

**LEBANESE AMERICAN UNIVERSITY**

Landslide Hazard and Risk Level Assessment of  
Quarried Slopes in Lebanon using Drone Imagery

By

Rouba Riad Kaafarani

A thesis

Submitted in Partial Fulfillment of the requirements

for the degree of Master of Science in Civil and Environmental Engineering

School of Engineering

August 2020

© 2020

Rouba Riad Kaafarani

All Rights Reserved

**THESIS APPROVAL FORM**

Student Name: Rouba Kaafarani I.D. #: 201305146

Thesis Title : Landslide Hazard and Risk Assessment of Quarried Slopes in Lebanon Using Drone Imagery


Program: M.Sc. in Civil and Environmental Engineering

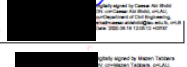
Department: Civil Engineering


School: Engineering

The undersigned certify that they have examined the final electronic copy of this thesis and approved it in Partial Fulfillment of the requirements for the degree of:

Masters \_\_\_\_\_ in the major of Civil Engineering

Thesis Advisor's Name <u>Grace Abou Jaoude</u>	Signature 	DATE: <u>18 / 08 / 2020</u> <small>Day Month Year</small>
------------------------------------------------	-----------------------------------------------------------------------------------------------	--------------------------------------------------------------

Committee Member's Name <u>Caesar Abi Shdid</u>	Signature 	DATE: <u>18 / 08 / 2020</u> <small>Day Month Year</small>
-------------------------------------------------	------------------------------------------------------------------------------------------------	--------------------------------------------------------------

Committee Member's Name <u>Mazen Tabbara</u>	Signature 	DATE: <u>18 / 08 / 2020</u> <small>Day Month Year</small>
----------------------------------------------	------------------------------------------------------------------------------------------------	--------------------------------------------------------------


## THESIS COPYRIGHT RELEASE FORM

### LEBANESE AMERICAN UNIVERSITY NON-EXCLUSIVE DISTRIBUTION LICENSE

By signing and submitting this license, you (the author(s) or copyright owner) grants the Lebanese American University (LAU) the non-exclusive right to reproduce, translate (as defined below), and/or distribute your submission (including the abstract) worldwide in print and electronic formats and in any medium, including but not limited to audio or video. You agree that LAU may, without changing the content, translate the submission to any medium or format for the purpose of preservation. You also agree that LAU may keep more than one copy of this submission for purposes of security, backup and preservation. You represent that the submission is your original work, and that you have the right to grant the rights contained in this license. You also represent that your submission does not, to the best of your knowledge, infringe upon anyone's copyright. If the submission contains material for which you do not hold copyright, you represent that you have obtained the unrestricted permission of the copyright owner to grant LAU the rights required by this license, and that such third-party owned material is clearly identified and acknowledged within the text or content of the submission. IF THE SUBMISSION IS BASED UPON WORK THAT HAS BEEN SPONSORED OR SUPPORTED BY AN AGENCY OR ORGANIZATION OTHER THAN LAU, YOU REPRESENT THAT YOU HAVE FULFILLED ANY RIGHT OF REVIEW OR OTHER OBLIGATIONS REQUIRED BY SUCH CONTRACT OR AGREEMENT. LAU will clearly identify your name(s) as the author(s) or owner(s) of the submission, and will not make any alteration, other than as allowed by this license, to your submission.

Name: Rouba Riad Kaafarani

Signature: \_\_\_\_\_

 Digitally signed by Rouba Kaafarani  
Date: 2020.08.17 23:52:55 +03'00'

Date: 17/8/2020

## PLAGIARISM POLICY COMPLIANCE STATEMENT

I certify that:

1. I have read and understood LAU's Plagiarism Policy.
2. I understand that failure to comply with this Policy can lead to academic and disciplinary actions against me.
3. This work is substantially my own, and to the extent that any part of this work is not my own I have indicated that by acknowledging its sources.

Name: Rouba Riad Kaafarani

Signature:  Digitally signed by Rouba Kaafarani  
Date: 2020.08.17 23:40:08 +03'00'

Date: 17/8/2020

*To Mohammad Ali, my supportive fiancée who had faith in me, encouraged me to take this step, and never failed in securing prospering environments at all times,*

*To my parents, brothers and friends*

*I dedicate my humble work.*

## **ACKNOWLEDGMENT**

I would like to extend my deep gratitude to my advisor, Dr. Grace Abou Jaoude for her continuous expert guidance, support, encouragement, advice, and patience through my two-year journey. I would like also to thank her for the efforts she did to secure the continuity and ease of the research, for her excitement about every progress we made, for being always besides me, not only as an advisor, but as a friend.

I would like to express my appreciation to my committee members, Dr. Caesar Abi Shdid and Dr. Mazen Tabbara whom I admired since my B.E.

Finally, I would like to acknowledge the continuous support of the lead engineering lab supervisor, Mr. George Shakour, the CIE computer lab supervisor, Mr. Hanna Boustany, and my colleague Mr. Hussein Rayshouni.

# Landslide Hazard and Risk Level Assessment of Quarried Slopes in Lebanon using Drone Imagery

Rouba Riad Kaafarani

## ABSTRACT

Human activities are continuously altering the geometry and steepness of natural slopes. When left exposed and unprotected, these slopes become susceptible to slide due to natural triggering factors like earthquakes and rainfall. Quarrying activities, in particular, contribute largely to slope failures worldwide, especially when unorganized and chaotic. In Lebanon, quarries are scattered randomly across the country and lack proper urban planning and management. Regional scale maps have been recently generated in a Geographic Information System (GIS) platform to identify hazard and risk areas for co-seismic and rainfall induced landslides; however, their applicability to altered “quarried” slopes has not been tested. In this research, we present a thorough methodology to assess, at a site-specific level, the hazard and risk levels of quarried slopes under three conditions: dry condition, heavy rainfall condition, and seismic condition. The aim is to ascertain the degree of accuracy of the regional scale maps in predicting landslides in quarried areas. A jointed limestone quarry in Bafliye, South of Lebanon, was mapped with a DJI Phantom 4 V2.0 drone, recreated as a 3D scene, assessed kinematically, and then analyzed using limit equilibrium and numerical modelling techniques. At failure, the maximum runout distance and the corresponding angle of reach were determined. The studied slope showed signs of failure under seismic events having a 10% chance of exceedance in 50 years, and under rainfall events having a 10-year return period with a relatively small runout distance of 7.76 m, yielding a low risk failure. The output of safety factors matched between the site specific and the regional scale analyses, while the failing mass volume and the corresponding risk levels did not. This indicated that the wedge failure analysis used in the regional scale analysis is adequate in predicting only hazard levels at quarried sites.

**Keywords:** Quarrying, Site specific, Regional scale, Drone, Landslide, Hazard, Seismic and rainfall events.



# Table of Contents

List of Tables .....	ix
List of Figures .....	x
<b>I. Introduction .....</b>	<b>1</b>
1.1 General.....	1
1.2 Site Description .....	7
<b>II. Literature Review .....</b>	<b>9</b>
2.1 Quarried Slopes Worldwide.....	9
2.2 Conditions of Quarried Slopes in Lebanon.....	10
2.3 Modes of Failures and Mapping Techniques .....	11
2.4 Stability Assessment Techniques .....	15
2.5 Shear Strength Model of Rock Joints and Rock Mass.....	16
2.6 Application to Quarried Slopes .....	17
<b>III. Methodology .....</b>	<b>22</b>
<b>IV. Results and Discussion .....</b>	<b>28</b>
4.1 Site Specific Analysis .....	28
4.1.1 Semi-automatic Joint Set Detection Output .....	28
4.1.2 Kinematic Analysis.....	28
4.1.3 Limit Equilibrium Analysis.....	30
4.1.4 Numerical Modelling Analysis.....	33
4.1.5 Comparison between LEM and FEM .....	33
4.1.5 Maximum Runout Distance and Angle of Reach .....	36
4.2 Comparison with Regional Scale Assessment .....	38
<b>V. Conclusion .....</b>	<b>43</b>
<b>VI. Limitations .....</b>	<b>45</b>
<b>References .....</b>	<b>46</b>
<b>Appendices .....</b>	<b>52</b>
Appendix A: Validation of 3D Model Measurements.....	52
Appendix B: Limit Equilibrium Results using RocScience SWEDGE.....	55
Appendix C: Numerical Modelling Using RocScience RS2 .....	64

# List of Tables

Table 1: Quarries density (per 1,000 hectares) as extracted from the World Bank report (2003)	2
Table 2: Intact rock properties used in RS2	27
Table 3: Input parameters used in RocFall	29
Table 4: Joint sets identified in DSE	28
Table 5: Factors of safety determined from SWEDGE under dry and wet conditions, as well as seismic loading	31
Table 6: Comparison between LEM and FEM results under all scenarios	36
Table 7: Wedges weights and their possible runout distance and angles of reach obtained from RocFall	37
Table 8: Width and Length of long and short bench and fountain as measured on field and in Pix4D Mapper	53

# List of Figures

Figure 1: Areas where quarries should be located vs actual quarries' location .....	3
Figure 2: Quarry in residential area in (a) Dahr El Baydar (b) Nahr El Mott.....	4
Figure 3: Proximity of quarries to urban settlements and roads (a) Biaqout (b) Abou Mizan (c) Harajel and Mayrouba .....	4
Figure 4: Quarry in Roumie, Maten area.....	5
Figure 5: Rainfall and earthquake hazards in (a) Aain Mouafaq and (b) Abou Mizan .....	6
Figure 6: Google Earth image of selected quarry site in Bafliye with quarries layer overlay .	8
Figure 7: Earthquake landslide hazard predicted by the regional scale map in Touaiti .....	11
Figure 8: (a) Planar sliding (b) wedge sliding (c) toppling failure (d) circular failure.....	12
Figure 9: Various discontinuity properties (Hudson and Harrison, 1997) .....	13
Figure 10: Offset between initial (blue dots) and computed (green dots) image positions along drone paths.....	22
Figure 11: 3D scene recreated in Pix4D Mapper .....	23
Figure 12: Number of overlapping images above the mapped area .....	23
Figure 13: Jointed rightmost slope face clipped in CloudCompare .....	24
Figure 14: Joints successfully detected using DSE and viewed in CloudCompare .....	25
Figure 15: Clusters representing joint set 1 (a) DSE output (b) Cluster representing quarry face discarded.....	25
Figure 16: Trace plane orientation determination.....	27
Figure 17: Angle of reach illustration .....	29
Figure 18: Google Earth image of the quarried slope detected in Halate, Jbeil.....	30
Figure 19: Elevation profile generated using 3D Analyst tool in GIS for Halate quarry .....	30
Figure 20: Methodology summary chart .....	27
Figure 21: (a) Rectangular block detected in joint set 10 (b) Area delineated for calculation in CloudCompare .....	29
Figure 22: Kinematic analysis (a) Planar sliding (b) Flexural toppling (c) Wedge sliding (d) Direct and oblique toppling .....	30
Figure 23: Factor of safety of the wedge formed by JS 5 and JS 3 (a) Dry conditions (b) Wet conditions (c) Seismic loading.....	32
Figure 24: Factor of safety of intersecting joint sets 10 and 5 under dry conditions .....	32
Figure 25: Slope elevation with joint sets 3 and 5 under dry conditions in RS2 .....	35
Figure 26: Slope elevation with joint sets 4 and 5 under wet conditions in RS2.....	35
Figure 27: Slope elevation with joint sets 10 and 4 under static seismic loading in RS2 .....	36
Figure 28: End location of wedge formed by joint sets 2 and 5 in case of failure as taken from RocFall .....	38

Figure 29: Slope profile as extracted from AcrMap for Befliye quarry .....	39
Figure 30: Google Earth image of Lebanon with geology and quarry layers overlay .....	40
Figure 31: Plassard rainfall map highlighting quarries locations.....	40
Figure 32: Pixelated rain hazards (pink) at the quarry site in Halat (grey polygon) .....	41
Figure 33: FS raster converted into point file for FS determination on site .....	41
Figure 34: Regional-scale runout analysis at Halat quarry in ArcMap .....	42
Figure 35: Variation between available polygon layer of quarries' area and actual quarry in Google Earth.....	42
Figure 36: Long bench, short bench and fountain at ELRC .....	52
Figure 37: soil contour at lower ELRC entrance .....	52
Figure 38: JS 5 and JS 6 (a) Dry conditions (b) 17% saturation (c) 0.25g ground acceleration .....	55
Figure 39: JS 2 and JS 3 (a) Dry conditions (b) 17% saturation (c) 0.25g ground acceleration .....	55
Figure 40: JS 2 and JS 4 (a) Dry conditions (b) 17% saturation (c) 0.25g ground acceleration .....	56
Figure 41: JS 8 and JS 4 (a) Dry conditions (b) 17% saturation (c) 0.25g ground acceleration .....	56
Figure 42: JS 3 and JS 4 (a) Dry conditions (b) 17% saturation (c) 0.25g ground acceleration .....	57
Figure 43: JS 9 and JS 4 (a) Dry conditions (b) 17% saturation (c) 0.25g ground acceleration .....	57
Figure 44: JS 9 and JS 3 (a) Dry conditions (b) 17% saturation (c) 0.25g ground acceleration .....	58
Figure 45: JS 2 and JS 8 (a) Dry conditions (b) 17% saturation (c) 0.25g ground acceleration .....	58
Figure 46: JS 3 and JS 8 (a) Dry conditions (b) 17% saturation (c) 0.25g ground acceleration .....	59
Figure 47: JS 2 and JS 9 (a) Dry conditions (b) 17% saturation (c) 0.25g ground acceleration .....	59
Figure 48: JS 8 and JS 5 (a) Dry conditions (b) 17% saturation (c) 0.25g ground acceleration .....	60
Figure 49: JS 9 and JS 5 (a) Dry conditions (b) 17% saturation (c) 0.25g ground acceleration .....	60
Figure 50: JS 2 and JS 5 (a) Dry conditions (b) 17% saturation (c) 0.25g ground acceleration .....	61

Figure 51: JS 6 and JS 4 (a) Dry conditions (b) 17% saturation (c) 0.25g ground acceleration	61
Figure 52: JS 5 and JS 4 (a) Dry conditions (b) 17% saturation (c) 0.25g ground acceleration	62
Figure 53: JS 10 and JS 4 (a) Dry conditions (b) 17% saturation (c) 0.25g ground acceleration	62
Figure 54: JS 10 and JS 5 (a) Dry conditions (b) 17% saturation (c) 0.25g ground acceleration	63
Figure 55: JS 5 and JS 6 (dry conditions)	64
Figure 56: JS 5 and JS 6 (rainfall intensity 0.103 mm/day)	64
Figure 57: JS 5 and JS 6 (0.25g ground acceleration)	65
Figure 58: JS 3 and JS 6 (dry conditions)	65
Figure 59: JS 3 and JS 6 (rainfall intensity 0.103 mm/day)	66
Figure 60: JS 3 and JS 6 (0.25g ground acceleration)	66
Figure 61: JS 2 and JS 3 (dry conditions)	67
Figure 62: JS 2 and JS 3 (rainfall intensity 0.103 mm/day)	67
Figure 63: JS 2 and JS 3 (0.25g ground acceleration)	68
Figure 64: JS 5 and JS 3 (rainfall intensity 0.103 mm/day)	68
Figure 65: JS 5 and JS 3 (0.25g ground acceleration)	69
Figure 66: JS 2 and JS 4 (dry conditions)	69
Figure 67: JS 2 and JS 4 (rainfall intensity 0.103 mm/day)	70
Figure 68: JS 2 and JS 4 (0.25g ground acceleration)	70
Figure 69: JS 8 and JS 4 (dry conditions)	71
Figure 70: JS 8 and JS 4 (rainfall intensity 0.103 mm/day)	71
Figure 71: JS 8 and JS 4 (0.25g ground acceleration)	72
Figure 72: JS 3 and JS 4 (dry conditions)	72
Figure 73: JS 3 and JS 4 (rainfall intensity 0.103 mm/day)	73
Figure 74: JS 3 and JS 4 (0.25g ground acceleration)	73
Figure 75: JS 9 and JS 4 (dry conditions)	74
Figure 76: JS 9 and JS 4 (rainfall intensity 0.103 mm/day)	74
Figure 77: JS 9 and JS 4 (0.25g ground acceleration)	75
Figure 78: JS 9 and JS 3 (dry conditions)	75
Figure 79: JS 9 and JS 3 (rainfall intensity 0.103 mm/day)	76
Figure 80: JS 9 and JS 3 (0.25g ground acceleration)	76
Figure 81: JS 2 and JS 8 (dry conditions)	77
Figure 82: JS 2 and JS 8 (rainfall intensity 0.103 mm/day)	77
Figure 83: JS 2 and JS 8 (0.25g ground acceleration)	78

Figure 84: JS 3 and JS 8 (dry conditions).....	78
Figure 85: JS 3 and JS 8 (rainfall intensity 0.103 mm/day) .....	79
Figure 86: JS 3 and JS 8 (0.25g ground acceleration).....	79
Figure 87: JS 2 and JS 9 (dry conditions).....	80
Figure 88: JS 2 and JS 9 (rainfall intensity 0.103 mm/day) .....	80
Figure 89: JS 2 and JS 9 (0.25g ground acceleration).....	81
Figure 90: JS 8 and JS 5 (dry conditions).....	81
Figure 91: JS 8 and JS 5 (rainfall intensity 0.103 mm/day).....	82
Figure 92: JS 8 and JS 5 (0.25g ground acceleration).....	82
Figure 93: JS 9 and JS 5 (dry conditions).....	83
Figure 94: JS 9 and JS 5 (rainfall intensity 0.103 mm/day) .....	83
Figure 95: JS 9 and JS 5 (0.25g ground acceleration).....	84
Figure 96: JS 2 and JS 5 (dry conditions).....	84
Figure 97: JS 2 and JS 5 (rainfall intensity 0.103 mm/day) .....	85
Figure 98: JS 2 and JS 5 (0.25g ground acceleration).....	85
Figure 99: JS 7 and JS 5 (dry conditions).....	86
Figure 100: JS 7 and JS 5 (rainfall intensity 0.103 mm/day).....	86
Figure 101: JS 7 and JS 5 (0.25g ground acceleration) .....	87
Figure 102: JS 6 and JS 4 (dry conditions).....	87
Figure 103: JS 6 and JS 4 (rainfall intensity 0.103 mm/day).....	88
Figure 104: JS 6 and JS 4 (0.25g ground acceleration) .....	88
Figure 105: JS 5 and JS 4 (rainfall intensity 0.103 mm/day).....	89
Figure 106: JS 5 and JS 4 (0.25g ground acceleration) .....	89
Figure 107: JS 10 and JS 4 (dry conditions).....	90
Figure 108: JS 10 and JS 4 (rainfall intensity 0.103 mm/day).....	90
Figure 109: JS 10 and JS 5 (dry conditions).....	91
Figure 110: JS 10 and JS 5 (rainfall intensity 0.103 mm/day).....	91
Figure 111: JS 10 and JS 5 (0.25g ground acceleration) .....	92

# Chapter One

## Introduction

### 1.1 General

Landslides are defined as the movement of a mass of rock or earth, as a whole or as debris, as a result of loss of shear strength. Considered a significant secondary effect of a dominant natural hazard (Xu et al., 2012), large slope failures are mostly triggered by natural hazards such as earthquakes and intense rainfall. Nevertheless, failures induced by human construction activities have been significantly increasing recently (Froude et al., 2018).

Human activities that increase the hazard of slope failures include cut slopes along a highway construction, unplanned construction on or near unstable slopes, illegal and legal mining, quarries, etc. These detrimental human interventions in naturally stable slopes increase the susceptibility of landslide occurrence (Froude et al. 2018). The extraction of soil or rock material from a slope by quarrying is one of the major triggers for landslide occurrences. According to Froude et al. (2018), 38.6% of non-seismic and non-rainfall triggered landslides are caused by both legal and illegal mining. Economic development, progress of human civilization and the ever-increasing demand on building materials such as limestone, granite and iron, are the main causes for the exploitation of slope material, and thus for potential geologic hazards like rock fall, unstable slopes and debris flows (Wang et al., 2018).

In Lebanon, quarries have been an important pillar for the economy since the end of the civil war in 1990 because of the reconstruction needs and the urban growth. Civil engineering works heavily increased the demand on construction materials, and led to the wide spread of the quarries all across the country, especially in mountainous terrains (Vedeil et al., 2007). Khawlie et al. (1999) presented a survey on the status of these quarries and indicated that in a period of 10 years, between 1987 and 1997, the number of quarries increased by 8%. Due to the lack of governmental supervision, the quarry sector became chaotic and very poorly organized (MOE/UNDP/ECODIT, 2011) with 1,278 quarries covering 5,267 hectares scattered all over the country. More than two thirds of these quarries (70.28%) extract limestone, 12.63% excavate

sandstone or sand and only 7.02% quarry marl as determined from overlaying the map highlighting quarries locations (Fig.1) over the geology map (Dubertret, 1945) readily available for Lebanon in GIS ArcMap. To better understand the distribution of quarrying practices in the country, the average density (number of quarries per 1,000 hectares) of quarries in each Lebanese province was presented in a report prepared by the World Bank in 2003 (Table 1).

*Table 1: Quarries density (per 1,000 hectares) as extracted from the World Bank report (2003)*

Provinces	Districts	Total area (hectares)	Number of Quarries	Density of quarries (per 1,000 hectares)
<b>Bekaa</b>	Baalbek	235,287	36	0.15
	Rashaya	53,710	15	0.28
	Western Bekaa	41,424	29	0.70
	Hermel	56,716	0	0.00
	Zahle	41,960	58	1.38
	<b>Total</b>	<b>429,097</b>	<b>138</b>	<b>Average: 0.32</b>
<b>Mount Lebanon</b>	Aaley	26,730	81	3.03
	Baabda	19,843	20	1.01
	Chouf	47,615	38	0.80
	Jbail	41,185	87	2.11
	Kesrouan	34,447	82	2.38
	Maten	26,829	59	2.20
	<b>Total</b>	<b>196,649</b>	<b>367</b>	<b>Average: 1.87</b>
<b>North Lebanon</b>	Akkar	79,787	28	0.35
	Batroun	27,580	59	2.14
	Beshamri	16,068	19	1.18
	Koura	18,103	14	0.77
	Tripoli	2,676	21	7.85
	Zgorta	17,457	13	0.74
	<b>Total</b>	<b>161,671</b>	<b>154</b>	<b>Average: 0.95</b>
<b>South Lebanon</b>	Jizzine	24,521	11	0.45
	Saida	26,856	3	0.11
	Sour	39,797	18	0.45
	<b>Total</b>	<b>91,174</b>	<b>32</b>	<b>Average: 0.35</b>
<b>Nabatieh</b>	Bint Jbeil	27,164	6	0.22
	Hasbaya	21,615	2	0.09
	Marjayoun	25,738	1	0.04
	Nabatieh	30,296	10	0.33
	<b>Total</b>	<b>104,813</b>	<b>19</b>	<b>Average: 0.18</b>

In a trial to regulate and organize quarrying activities in the country, a national plan designating sites suitable for quarrying activities was produced in 2009. The map proposed unpopulated areas where the damages on the surrounding environment are minimal as suitable mining locations. Nevertheless, open-pit mining continued outside the specified areas (Fig. 1), and in the last two decades, unsupervised quarrying activities have even extended to urban areas, provoking localized landslides, destabilizing buildings and threatening a total of 20,000 apartments by unstable slopes beneath (Fig. 2a and Fig. 2b) (Darwish et al., 2010). The proximity of quarries to urban



settlements and infrastructure (mainly roads) was checked in GIS ArcMap 10.3, by overlaying the roads map, urban settlement map and the quarries' locations map on top of each other (Fig. 3). Three locations were selected to show case the proximity in Biaqout (Fig. 3a), Abou Mizan (Fig. 3b) and Hrajel and Mayrouba (Fig. 3c) (from South to North). The quarry in Biaqout is heavily surrounded by urban settlements and is exposed to nearby road (Fig. 3a), and hence its failure would result in significant risks on settlements and infrastructure.

In fact, the removal and weakening of supporting rocks underneath residential buildings due to quarrying activities in Biaqout, Mount Lebanon, triggered a slope instability in February 16<sup>th</sup> 2000 which resulted in the complete destruction of two buildings and the partial destruction of another one (Abdallah, 2011).

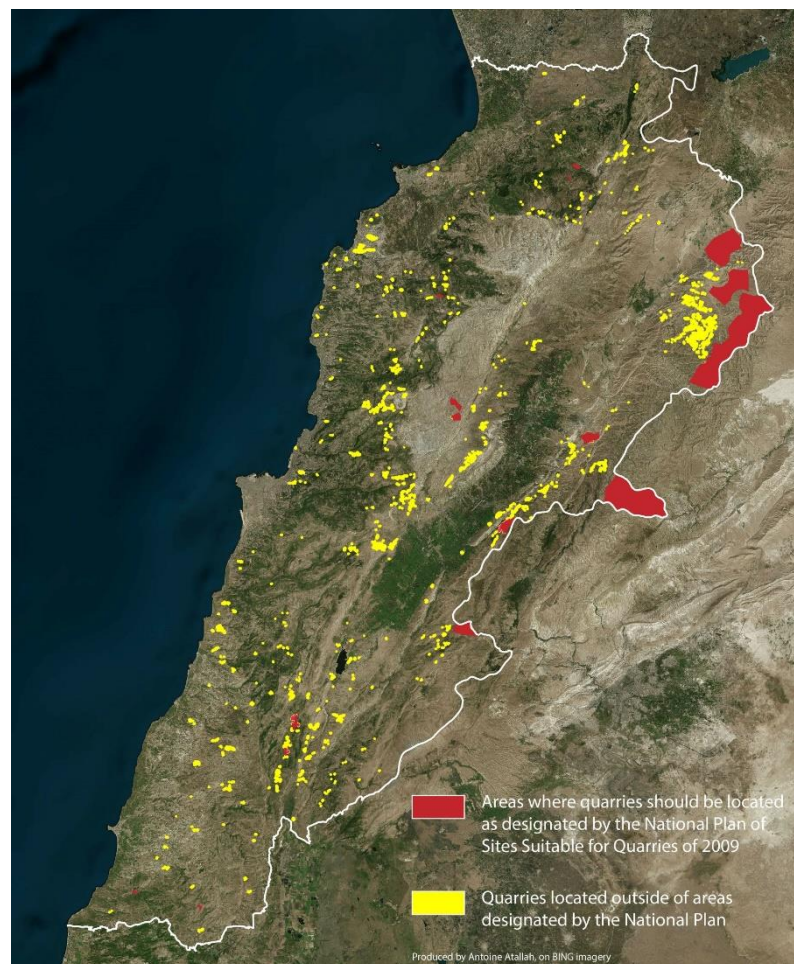


*Figure 1: Areas where quarries should be located vs actual quarries' location*



Figure 2: Quarry in residential area in (a) Dahr El Baydar (b) Nahr El Mott

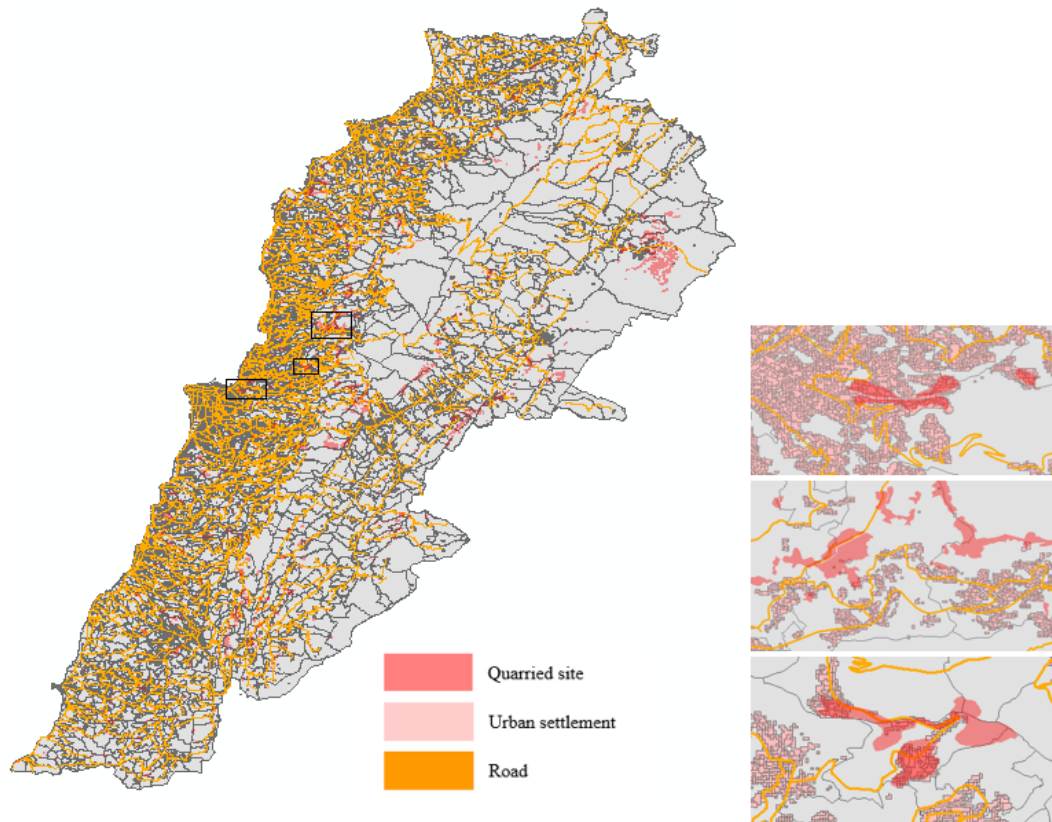


Figure 3: Proximity of quarries to urban settlements and roads (a) Biaqout (b) Abou Mizan (c) Harajel and Mayrouba

The operations at four neighbor quarries in the region of Roumie, Maten, along with heavy rainfall triggered rock fall, and the failing rock mass reached a nearby local road according to El-Nashra news (Fig. 3).



*Figure 4: Quarry in Roumie, Maten area*

Recently, Grant et al. (2016) and Kaafarani et al. (2019) assessed the rugged terrain under earthquake and rainfall events at a macro level (regional scale) using a multi-modal approach, where slopes were analyzed based on their geology and degree of inclination. Pollock et al. (2019), then, evaluated the risks associated with the predicted landslide hazards. This regional-scale work was performed in a GIS framework, based on the geologic map of Lebanon, a 15-m digital elevation map (DEM), earthquake peak ground acceleration (PGA) maps and rainfall data.

The regional scale model predicted that 183 quarries will fail under rainfall events (10 years return period storm) and 20 quarries will fail under earthquake triggering (10% probability of exceedance in 50 years). Fig. 5 shows rainfall and earthquake hazards predicted by the regional scale multi-modal model in Aain Mouafaq (Fig. 5a) and Abou Mizan (Fig. 5b). Under rainfall, six quarries will have high to low risks on nearby local, primary and international roads, and 19 quarries will have high to low risks on surrounding urban settlements. For instance, the quarry in Mazraet El Kreine is prone to rock slope failure and it will have a high risk on a nearby local road and surrounding urban settlements. The quarry in Abou Mizan area will result in a medium risk over two primary roads and urban settlements, and the quarry in Ehmej will have a low risk impact on a local road and nearby settlements. Several quarries will only impact the infrastructure (the quarry in Falougha will result in a low risk failure that will mainly affect the international road passing nearby), and other quarries will only impact urban



settlements (the quarry in Aain Mouaffaq will have a high risk on urban settlements in case of failure).

Under seismic events, five failing quarries will have high (quarries in Haret Hamze and Aain Mouaffaq) and medium (quarries in Bkaakouta, Baskinta, and Abou Mizan) risks on urban settlements, while only one quarry in Qarne will heavily affect a local road with failing rocks.

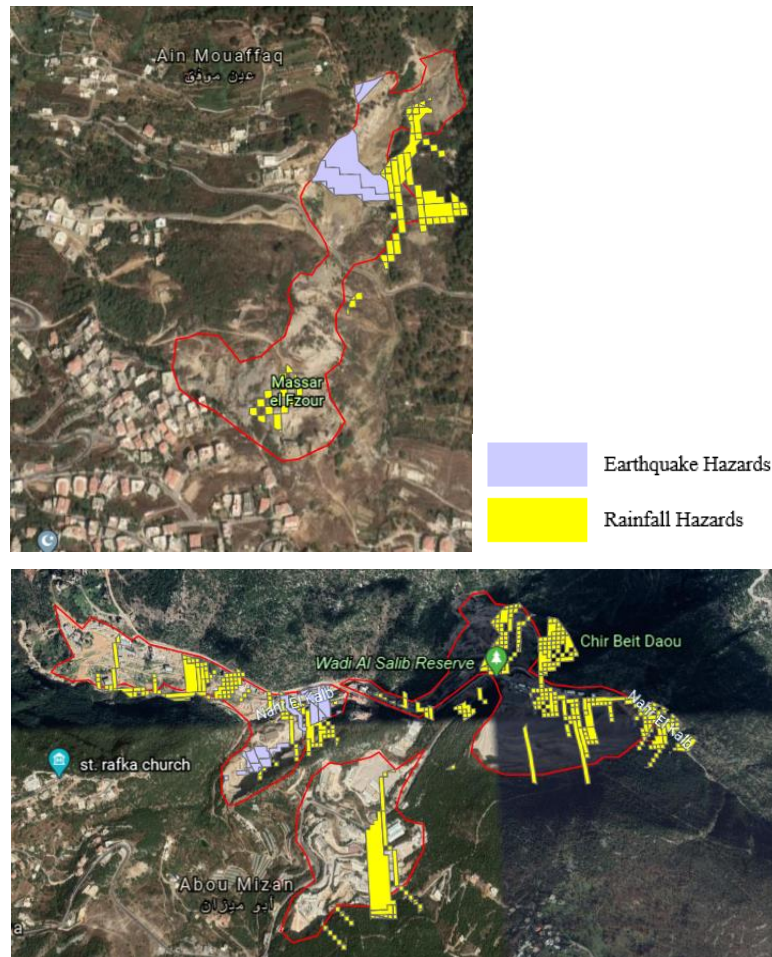


Figure 5: Rainfall and earthquake hazards in (a) Aain Mouaffaq and (b) Abou Mizan

Quarries have been heavily criticized in the news for their negative impact on the environment as well, namely the quarries located in Mayrouba, Harajel, Abou Mizan, Aain Dara, Kfarmatta, Baisour, Rihan, Jezzine, Wata el Jaouz, Kfarhouna, and Tarshish.

Despite the significance and persistence of quarrying problems in the country, the stability of these slopes has not been studied, especially under extreme conditions like earthquakes and heavy rainfall. Researchers rather focused on co-seismic stability

assessments of individual natural slopes given the rugged topography of Lebanon and its location in an active seismic zone (Ismail et al., 2014, Fawaz et al., 2014). The produced maps of Grant et al. (2016) and Kaafarani et al. (2019) can be easily used for a quick stability check everywhere in the country and specifically in quarry locations (Fig. 5). However, hazard and risk predictions can be further refined and updated based on site specific analysis with a more accurate and refined digital elevation map.

Thus, the purpose of this work is to define a coherent methodology to assess the hazard and risk levels of quarried slopes based on site-specific analysis, and to assess the ability of the regional scale model developed by Grant et al. (2016) to predict landslide hazards and risks at quarried sites in Lebanon. The developed methodology will allow full analysis of limestone slopes in general and quarried slopes in particular, and will be applied to the regional-scale maps to update hazard and risk levels at quarry sites. The proposed methodology will be adopted to produce an independent regional-scale hazard and risk map for quarries in Lebanon. This map can be further used to employ suitable prevention strategies and recommend alternative appropriate quarrying locations in case of high hazard and risk levels. The map will also contribute in the development and update of urban planning policies in the country to ensure safe future urban development and growth.

## **1.2 Site Description**

The proposed methodology is tested on a limestone quarry located in Bafliye, South Lebanon, that extends from 33°15'59.75" N 35°23'03.64" E to 33°15'58.89" N 35°22'47.84" E (Fig. 6). The slope is 58.5 meters high, 250 meters wide, 70° steep and dipping at 350°(to the North). The magnetic declination was determined using both a compass on site and available online databases based on location as +5°, hence making the slope dipping at 355°. The geology of the site is mainly comprised of Sannine white fractured limestone (Dubertret, 1945) which has a unit weight of 23 kN/m<sup>3</sup>. Multiple discontinuities can be easily identified on the slope face with some extensively extending forming wedges of various sizes. No failures were observed as the quarry was visited during summer.

All relevant strength parameters were determined from the available soil and rock material database in RocScience RocData, as needed in the analyses that were conducted. Based on the PSHA maps of Huijjer et al. (2011), the site is subject to a

peak ground acceleration (PGA) of 0.25g resulting from an earthquake having a 10% probability of exceedance in 50 years. The rainfall intensity in the region is 103 mm/day causing a 17% saturation for a storm having a 10 year return period (Plassard, 1971; Kaafarani et al., 2019).



Figure 6: Google Earth image of selected quarry site in Bafliyeh with quarries layer overlay

# Chapter Two

## Literature Review

### 2.1 Quarried Slopes Worldwide

Quarrying or open-pit mining is the process through which rock, sand, gravel or other materials and minerals are extracted from the ground to be used for construction purposes or other uses. Quarrying activities are usually carried out using different techniques, namely drilling, blasting, sawing and splitting or a combination of different methods. The choice of a suitable, cost and time-effective quarrying technique depends mainly on the hardness, type and intended use of the material to be extracted. In general, open-pit mining is designed in a way that produces minimal impact or damage on the integrity and soundness of the extracted material, and the surrounding rock mass (Cardu et al., 2005, Bhandari et al., 2002). A slope design is routinely carried out in a way that reduces costs and improves the stability and safety of the quarry. However, several failures have been recorded in quarry sites due to various factors such as unpredicted environmental events and uncontrolled blasting or mining practices. In 1618, quarrying in the mountain slopes of the southern Swiss town of Pleurs triggered a massive rock fall that killed 2430 people. Another large non-supported quarry cut into a mountain in Elm, eastern Switzerland, triggered a rock avalanche in 1876 and killed 116 people. In 1903, seventy people were killed by the limestone rock slide that developed in the joint planes of a coal mine in Alberta (Kellerer-Piklbauer, 2002). A steep limestone quarry near the city of Trabzon in northeast Turkey experienced three planar failures under heavy rainfall, and resulted in the demolition of a school, house, and a mosque. The failures also affected the nearby road and farms adversely (Karaman et al., 2013). Other quarrying activities coupled with complex geological settings and caused persistent displacements in a lignite quarry in Mavropigi, Greece. A large crack was generated due to quarrying practices 600 meters behind the slope face, and continued to increase in both length and width. This crack caused continuous horizontal displacements reaching a deformation rate as high as 40-50 mm/day when precipitation occurs, and yet mining activities continued under surveillance on top of the moving mass (Chrysanthos et al., 2017). Quarries, therefore, even when properly designed and monitored, are still failing and causing substantial damages worldwide.

## 2.2 Conditions of Quarried Slopes in Lebanon

In Lebanon, where quarries are mostly illegal and largely spread across the entire country, very few are properly designed, supervised, and monitored (MOE/UNDP/ECODIT, 2011). The only recorded failure is that of the quarry slope underneath a residential project in Biaqout, which triggered a rock slide in February 2000 due to heavy rainfall. The sliding mass resulted in the complete destruction of two buildings and to the partial destruction of another one (Abdallah, 2011). In spite of the damage it caused, no study was done to back analyze this failure nor was the stability of any other quarry questioned. Rather, all available studies in the literature focused on assessing the environmental impact of quarries on the surrounding ecosystems. For example, Darwish et al. (2010) assessed the environmental impact of quarried sites on natural ecosystems in Lebanon using satellite imagery and an integrated GIS approach to explore the potential of future quarrying activities in terms of land suitability and impact alleviation. The impact assessment of current quarrying activities on natural ecosystems showed that 272 quarries have high impact, 657 have medium impact and 349 have low impact. The study applied a land suitability model for quarrying activities based on geomorphological and ecological factors to show that a large area (6222.3 km<sup>2</sup>) is unsuitable for quarries, distributed mainly in the Central Mountain and western Lebanese areas.

From a slope stability perspective, studies have been mainly focused on co-seismic slope stability assessments because of the rugged topography and location of the country in an active seismic zone. Ismail et al. (2014) studied the stability of a 20 meters high slope in silty sand deposits under seismic loading using finite difference models in FLAC 3D and showed how soil cohesion, friction angle, and earthquake frequency affect the stability. Fawaz et al. (2014) and Fawaz et al. (2017) used finite element models and limit equilibrium analysis to show that high intensity rainfall events as well as a highway cut-slope excavation tremendously decreases the general stability of the natural slope. They highlighted the effects of the triggering factors, namely earthquake loading and highway excavation, on the instability of the natural ground during dry and rainy seasons. They proposed the use of piles and nails as the most effective solutions in reducing the effect of highway excavation on the continuous slope deformation and stability.



Saade et al. (2016) and Grant et al. (2016), on the other hand, assessed the regional-scale hazard of landslides triggered by earthquake and rainfall events in Lebanon based on the geologic map of Lebanon, a 15-m digital elevation map (DEM), earthquake peak ground acceleration (PGA) maps, rainfall data, and a preliminary landslide inventory database. Their work was performed in a GIS framework and regional-scale landslide hazard maps were produced for co-seismic landslide hazards and rainfall-induced landslide hazards. This state-of-the-art work is the only available database from which the approximate stability of quarried slopes could be inferred. In fact, the available regional maps predict failures at several quarried sites under rainfall and seismic events (Fig. 5 and Fig. 7). This further enhances the need for assessing particular high risk zones through focused studies that could be later fed into the GIS framework to further refine and confirm these predictions. Accordingly, the interest in the present work is to identify a time and cost efficient methodology to assess stability issues in quarried sites across the country.

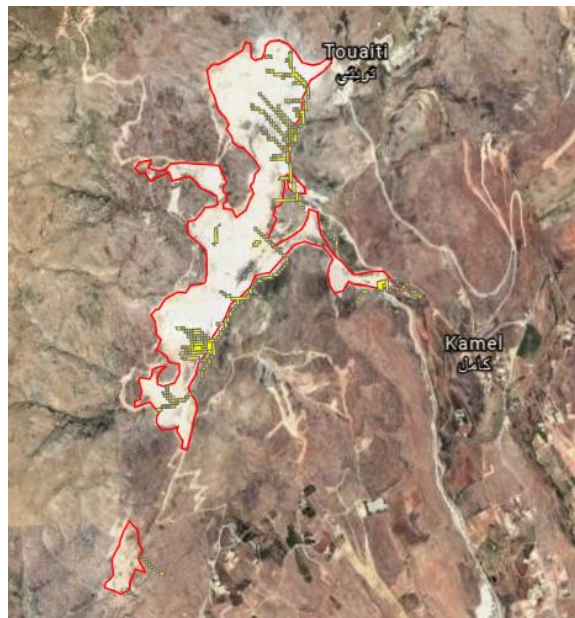


*Figure 7: Earthquake landslide hazard predicted by the regional scale map in Touaiti*

### **2.3 Modes of Failures and Mapping Techniques**

Failures occurring on rock slopes worldwide, whether quarried or not are usually dictated by the presence of discontinuities since it is seldom that rock exists as a complete non-fractured unit. In fact, rock masses typically comprise multiple intact rock blocks delineated by oriented structural discontinuities such as joints, bedding surfaces, foliations, etc. These discontinuities are referred to as structural fabric of the

rock mass, and may induce slope instability depending on their orientations (Hoek and Bray, 1981).

These discontinuities make the slope susceptible to four modes of failure: planar sliding, wedge sliding, toppling failures and circular failures. Planar sliding is usually governed by one discontinuity surface that is daylighting the slope face, and along which sliding occurs (Fig. 8a). Wedge sliding however, is defined by two intersecting joints having their line of intersection daylighting the slope, usually due to excavation activities and hence is considered a particular case from planar sliding. In this mode of failure, sliding occurs either on the line of intersection, or along the steeper of the two discontinuity planes in the direction of maximum dip (Fig. 8b). In toppling failure, rock slabs or columns (depending on their dimensions) dipping into the slope face usually rotate about a fixed point at their bases with slippage occurring simultaneously between the rock layers (Fig. 8c). For circular failures to occur, the intact rock material has to be very weak or the rock mass as a whole has to be extremely fractured. This type of failure is not controlled by structural discontinuities, and progresses following a circular arc at the base (Fig. 8d) (Norrish and Wyllie, 1996).

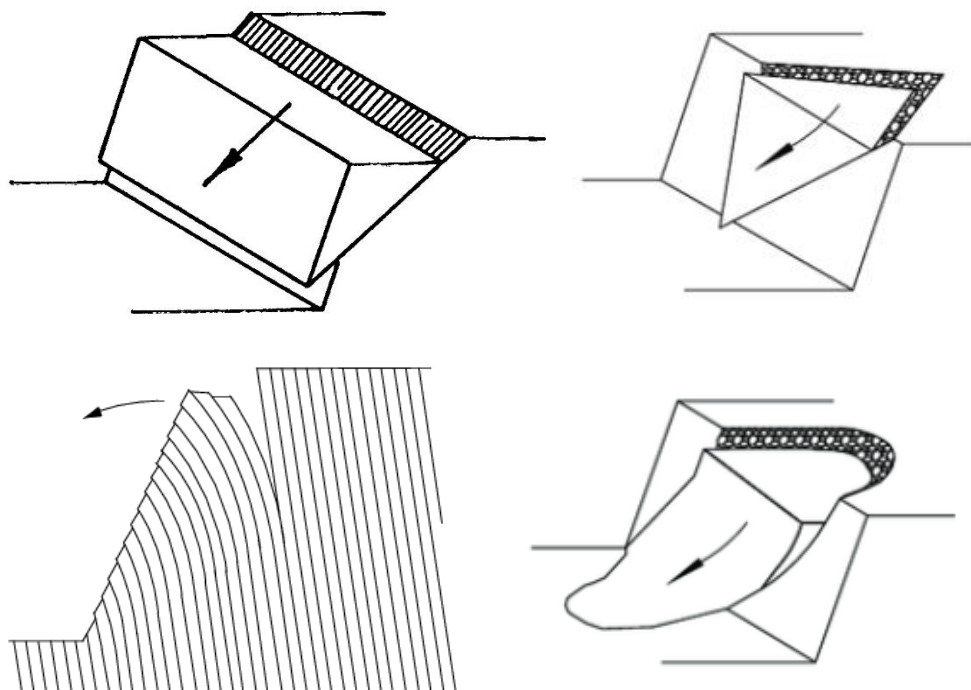


Figure 8: (a) Planar sliding (b) wedge sliding (c) toppling failure (d) circular failure

To conduct a proper rock slope analysis, the discontinuities causing failures in rock masses need to be mapped and their properties need to be determined using appropriate field data acquisition. Discontinuity mapping procedure is dictated by the international

society of rock mechanics (ISRM). ISRM specifies the properties to be measured, along with the methods and equipment to be used. The properties of interest in discontinuities are mainly the orientation, usually determined by either dip and dip direction or strike and dip, the spacing between successive discontinuities, persistence, roughness, wall strength, aperture, filling, water seepage, number of discontinuity sets (usually a set includes parallel discontinuities), and block size (Hudson and Harrison, 1997) (Fig. 9). As it is practically non-feasible to map each discontinuity and determine the corresponding properties, horizontal and vertical scanlines, rectangular and circular mapping windows are adopted. Scanline mapping involves tracing either a horizontal or vertical line (or both) using a tape on the slope face, and detect all discontinuities intersecting this line. The previously mentioned characteristics are determined for these discontinuities, and then the parallel ones are grouped together in one separate discontinuity set. Rectangular and circular window sampling is similar to scanlines, except that in this procedure, discontinuities are divided into three classes: (1) discontinuities intersecting the window with both their ends contained inside it, (2) discontinuities dissecting the window with one end only visible inside it, and (3) Discontinuities transecting the window with no end visible inside it (ISRM, 1978; Priest, 1993).

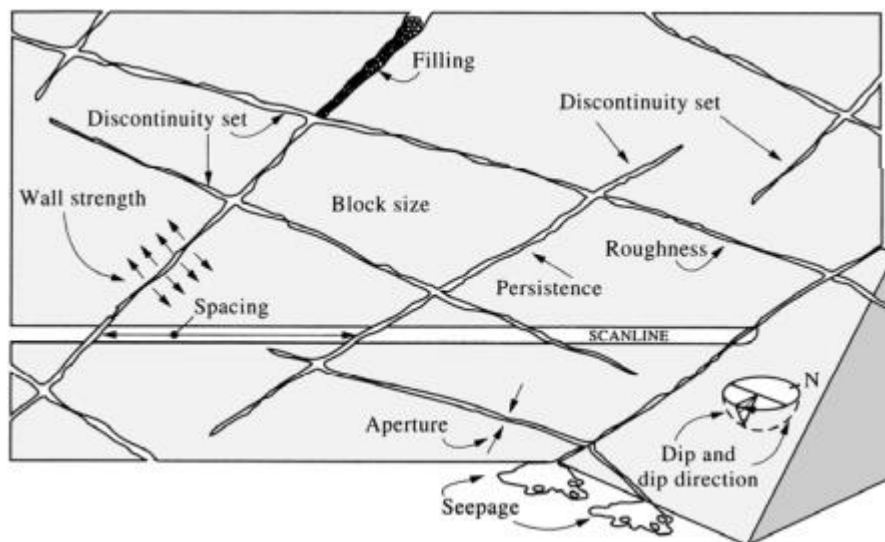


Figure 9: Various discontinuity properties (Hudson and Harrison, 1997)

The mentioned standard methods require manual geological data acquisition in the field, which can be challenging in case the site is inaccessible or the rock slope face is susceptible to fail. The time and costs involved in field data collection, along with other problems affect both the quality and quantity of information acquired, and investing

greater efforts and extra field work usually yield relatively small improvements (Crosta, 1997; Mah et al., 2011). Considering these limitations, several authors (Crosta, 1997; Kemeney et al., 2006; Mah et al., 2011; Sturzenegger et al., 2011) proposed and implemented other methods, mainly remote sensing ones, for geological discontinuity mapping and characterization, which are based on 3D images. The images are suggested to be obtained using both 3D terrestrial laser scanning (LIDAR) and digital photogrammetry, which allow a large amount of data to be efficiently gathered from a safe distance (Mah et al., 2011). Advancement in remote sensing was achieved in recent decades, with the development of small unnamed aerial vehicles (UAV) systems (i.e. drones), rendering the spatially continuous data acquisition more precise (high resolution to a centimeter precision) and less costly. Given the relatively low altitude of UAVs, the influence of weather on the remotely sensed images is relatively low, and the need for a special airport to take off is absent unlike other aircraft mounted remote sensing techniques. UAVs also allow a more flexible control for orientation changing, camera angle setting, initiation and termination of photography missions (Rossini et al. 2018; Tomastik et al. 2017; Xi and Li 2017). The new technique proved to be even faster with lower costs than airborne or ground-based LiDAR sensors (Rossi et al., 2018). Due to all these advantages, UAVs have been widely used in landslides monitoring, mining activities surveying, and general civil engineering practices (Rossini et al. 2018; Tomastik et al. 2017; Xi and Li 2017).

The captured images can be used to reconstruct the topography as a 3D model in readily available digital photogrammetry software, which are based on algorithms able to provide spatial information from features detected in two or more images. These software, also known as structure-from-motion (SfM) software, allow high-definition point clouds, digital surface models (DSM), and ortho-photos to be produced (Westoby et al. 2012; Colomina and Molina 2014). Uysal et al. (2015) used photogrammetry data collected with a UAV to produce high accuracy digital elevation models (DEM), while Yu et al. (2017) and Marinos et al. (2017) utilized the acquired data to achieve a great progress in slope modelling and identification using UAV photogrammetry. Salvini et al. (2018) employed UAV photogrammetry data along with discrete fracture networks to conduct slope stability assessment in a series of trials.

With the aid of the 3D point cloud and 3D models that can be generated and the use available images, the detection of discontinuities, their sets and properties can be easily

completed, either manually or semi-automatically using available, open-source algorithms. The latter method is widely used in the literature (García-Sellés et al., 2011; Gigli and Casagli, 2011; Khoshelham et al., 2011; Lato et al., 2010; Lato and Vöge, 2012; Olariu et al., 2008; Sturzenegger and Stead, 2009; Sturzenegger et al., 2011). It reduces the overall analysis time usually required in tedious field investigations using scanlines and other standard methods, while allowing user control and supervision of the results (Riquelme et al., 2014). Riquelme et al. (2014) proposed and tested a method for a semi-automatic algorithm (discontinuity set extractor or DSE) that can be used as an add-in in MATLAB. Their algorithm, unlike other available ones in the literature, which use triangulated irregular network (TIN) to simplify the surface (Gigli and Casagli, 2011; Lato et al., 2009; Slob 107 et al., 2007), uses real 3D (instead of 2.5D mesh surface) information stored in every point of the point cloud to be able to trace discontinuities and arrange them into sets. The algorithm was tested on regular geometric shapes like a cube, and then was tested on an actual slope with visible planes to verify its ability to detect these planes. The DSE algorithm was used in a full study to assess the stability of a slope in the National route N-332 in El Campello, Alicante, Spain, and it perfectly detected the slope planes which were visually validated (Riquelme et al., 2016).

## **2.4 Stability Assessment Techniques**

Once the discontinuities are mapped, detected and their properties are determined, the stability of the slope can be assessed using kinematic analysis, limit equilibrium methods, numerical modelling, and slope stability probability classification (Costa et al., 1999; Karaman et al., 2013; Sajinkumar et al., 2014; Alejano et al., 2017; Abdullah et al., 2018; Wang et al., 2019).

Kinematic analysis is usually the first step when evaluating the stability of a rock mass. In this analysis, a stereographic projection is performed to assess the stability of the structural fabric (i.e. discontinuities) through their dip and dip direction (Hoek and Bray, 1981). Kinematic analysis predicts the probability of occurrence for each mode of failure. If a failure mode is determined to be kinematically admissible, then the slope stability against this specific failure mode is analyzed using limit equilibrium methods (LEM).

Limit equilibrium methods are heavily adopted by researchers and engineers to calculate the ratio of the resisting forces to the driving forces, also known as the safety factor (Norris and Wyllie, 1996). The methods of slices (Fellenius, Janbu, Bishop, Spencer, and Morgenstern-Price) are the most commonly used limit equilibrium methods for slope stability problems. These techniques are statically indeterminate, and several assumptions are made to eliminate this indeterminacy, and hence only the global equilibrium is satisfied (Yu et al., 1998; Liu et al., 2015). Limit equilibrium methods also do not consider strains or displacements, and thus the inter-slice and slip surface stresses are not necessarily representative of the actual field stresses (Krahn, 2003).

Given the limitations of limit equilibrium methods, finite element methods such as the shear strength reduction technique (SSR) was found to be more advantageous to assess slopes' stability, and it has been adopted by researchers (Dawson et al., 1999). In SSR, the shear strength parameters (friction angle and cohesion), are reduced progressively until failure occurs. The reduction factor causing the failure is reported and it is equal to the factor of safety of the slope under study (Matsui and San, 1992).

Slope stability probability classification (SSPC), is widely used in the literature as well to determine the probability of occurrence of different failure modes in rock slopes, rather than determining a single-point rating value like other rock classification systems (Karaman et al., 2013; Li and Xu, 2015; Hack et al., 2003). The SSPC method is based on a three-step classification system to describe the exposure rock mass (ERM), reference rock mass (RRM), and slope rock mass (SRM). Using this approach, the rock slope stability is determined by two analyses: orientation-dependent stability analysis and orientation-independent stability analysis (Hack et al., 2003; Li and Xu, 2015).

## **2.5 Shear Strength Model of Rock Joints and Rock Mass**

In both limit equilibrium and finite element methods, the Barton-Bandis (B-B) criterion is usually adopted to model the shear strength of discontinuities. The B-B model predicts the shear failure behavior of rough rock joints. It is extensively verified against a wide range of experimental results, and its parameters can be easily determined using simple tests and they have real physical meaning (Prasetyo et al., 2017). The shear strength of discontinuities is determined using the criterion:

$$\tau = \sigma_n \tan \left[ JRC \log_{10} \left( \frac{JCS}{\sigma_n} \right) + \varphi_r \right]$$

where  $\tau$  is the shear strength,  $\sigma_n$  is the normal stress, JRC is the joint roughness coefficient, JCS is the joint compressive strength (MPa), and  $\varphi_r$  is the joint residual friction angle.

To model intact rock, the generalized Hoek-Brown criterion is usually employed. The criterion is non-linear and relates the major and minor effective principal stresses based on the following equation:

$$\sigma'_1 = \sigma'_3 + \sigma_{ci} \left( m_b \frac{\sigma'_3}{\sigma_{ci}} + s \right)^a$$

where  $\sigma'_1$  and  $\sigma'_3$  are the axial and confining effective principal stresses,  $\sigma_{ci}$  is the uniaxial compressive strength (UCS) of the intact rock material,  $m_b$  is a reduced value of the material constant  $m_i$ , and  $s$  and  $a$  are constants which depend upon the characteristics of the rock mass. For intact rock,  $m_b$  and  $m_i$  are the same.

## 2.6 Application to Quarried Slopes

The previously mentioned analysis methods (kinematic, LEM , FEM, etc.), data acquisition and interpretation techniques are employed widely in the literature along with other methodologies such as geophysical and environmental ones, to analyze rock slopes in general, and quarried slopes in particular. Quarried slopes stability interpretation are frequent in the literature as case studies mainly, where the focus is either on quarries that have failed already, or on open-pit mines having properties very similar to a failing quarry. These case studies conclude usually whether a quarry is safe given its current state, or under different natural events or excavation methods, with some of them suggesting mitigation measures and proposing adequate recommendations.

For instance, Costa et al. (1999) assessed the slope stability of a slate quarry in Delabole, UK using distinct element modeling on UDEC, by performing a sensitivity analysis on block and discontinuity properties. Instead of undergoing a detailed slope stability analysis, the authors identified, using a parametric analysis, that the quarry has a potential of failing following a translational planar sliding mechanism which controls slope deformation and induces instability. To ensure the development of realistic models in UDEC, site investigations were carried out to detect instabilities,

monitor both deformation and groundwater, survey scan lines, and determine rock strength and material behavior. Stereographic analysis was performed as well to confirm the kinematic possibility of planar failure on cleavage, and limit equilibrium analysis was done using PLANSTAT to evaluate the planar instability.

Karaman et al. (2013) evaluated the stability of three rock slopes in a limestone quarry in the area of Trabzon northeast Turkey, which are being excavated by two techniques: mechanical excavation and blasting. The most prone failure mechanism of the slopes was checked using kinematic analysis, and then their stability was evaluated using both orientation dependent, and orientation independent analyses from the slope stability probability classification (SSPC) system. Finally the results were compared to the ones obtained from slope mass rating (SMR) system. The geotechnical properties of the rock mass used in the analysis (discontinuity properties, UCS, point load strength index, unit weight, friction angle, weathering degree and groundwater conditions) were determined from field and laboratory testing. To determine the most suitable rock extraction technique from all three slopes, the authors studied the excavatability of the rock slopes, determined it as easy ripping and thus recommended pneumatic hammer as the mean of excavation that will achieve a stability probability  $\geq 80\%$ . A maximum height of 8 m for the three slopes was proposed, and safe dip angles of  $70^\circ$  for slope 1 (RMR=53),  $66^\circ$  for slope 2 (RMR=48) and  $75^\circ$  for slope 3 (RMR=59) were suggested to ensure slope stability.

Sajinkumar et al. (2014) studied quarried slopes stability during the monsoon in Barasuramala, India from three perspectives: geotechnical, geophysical, and environmental (i.e. EIA). Field measurements were done to map the landslide affected areas using a total station (Pentax R322NX), determine the soil shear strength parameters, and detect the possible failure mechanism(s). Translational slide failure was detected from vertical electrical sounding (VES) and from observations of soil cracks developed during the monsoon season. The authors assessed eight slopes across the area of study under dry, wet and saturation conditions using one dimensional infinite slope model. They found that all slopes are unstable under wet and saturation conditions. They determined also from EIA results that the possibility of rock fall is very high and showed that quarrying activities induce vibrations that may trigger landslides, strip soil and increase soil erosion. Recommendations like using controlled



blasting, banning quarrying activities during the monsoon season and constructing surface drains were made to minimize the risk of failure.

Alejano et al. (2017) analyzed the stability of an over tilted or inverse slope (i.e. dip angle is greater than  $90^\circ$ ) under seismic events having a ground acceleration of 0.04g and rainfall events with a return period of 100 years and an average annual rainfall rate of 165 l/m<sup>2</sup>. The rock mass was characterized using ISRM proposed methodologies (scanlines), where the dip, dip direction, joint roughness coefficient, joint compressive strength, weathering and water content were evaluated. The spacing of the rock joints were measured from obtained photographs on site, and the intact rock properties (UCS, UTS, density and friction angle) were determined using laboratory tests. Three cross sections were made along the quarry using available traditional surveying and topographic maps, and the steepest section of quarry was carried out for further analysis. Using kinematic analysis, planar failure and block toppling were the failure modes with the highest probabilities of occurrence. Therefore, RocScience Roc-Plane was utilized to determine the factor of safety, which was determined as 1.37 and thus the slope was determined to be a stable one. To validate the results, Monte-Carlo analysis was performed to estimate the probability of planar failure, and it was determined as 1.64% using the most conservative parameters, and thus the slope again has proven to be stable, with the planar failure unlikely to occur. The factor of safety against toppling failure was estimated from equations (ratio of stabilizing moments to overturning moments), and was found to be greater than 3.0 and thus the toppling will not take place on the slope under study.

Similarly, Abdullah et al. (2018) assessed the stability of a vertical quarry with interbedded calcareous sandstone and siltstone in Karang, Sambung district in central Java, Indonesia. The rock mass was classified on site using vertical and horizontal scanline mapping to determine strike and dip orientations. The rock mass was characterized as “fair” using the rock mass rating system (RMR). Kinematic analysis was then performed using RocScience DIPS, and it was determined that failure is controlled by intersecting joint sets, and thus yielding wedge failure with a probability of occurrence of 29% for region 1 and 49% for region 2. Hence, RocScience SWEDGE was selected for further detailed analysis, and both quarry regions proved to be unstable with factors of safety of 0.79 for region 1 and 0.58 for region 2. The stability of the slope was also assessed using numerical modelling (RocScience RS2), but in

this analysis both slope regions were stable ( $FS = 1.78$  for region 1 and  $FS = 1.31$  for region 2). Finally, the safe buffer zone, where no risk of rock fall is present, was determined using RocScience RocFall as 3.1 meters away from the face of region 1 and 3.6 meters away from the face of region 2).

Wang et al. (2019) utilized UAV acquired photogrammetry data in a structure from motion (SfM) software, Agisoft PhotoScan, to reconstruct the 3D scene and build the digital elevation model of the rock mass under study. The authors then used a random sample consensus (RANSAC) shape detection algorithm to determine all structural planes in the point cloud generated for the entire slope. The authors developed a computer program for rock block identification, based on geotechnical structure and model analysis-3D system (GeoSMA-3D), to analyze the kinematic slope stability. Then, the developed methodology was tested in a case study where the stability of a three-step open-pit limestone mine in Xiping County, Yunnan Province, China was assessed at different slope angles ( $45^\circ$ ,  $60^\circ$ , and  $80^\circ$ ). The slope was mapped using a DJI Phantom 4 Pro drone, and 117 images were collected on site. Eleven ground control points were marked on site and their coordinates were determined using a total station, to increase the geo-location accuracy of the point cloud of the 3D model. RANSAC detected a total of 491 structural plane on the entire slope which were grouped into three discontinuity sets. Removable blocks, or blocks susceptible to fail were determined on the three steps of the slope, along with their volume and corresponding factors of safety. As the slope becomes steeper, the volume of the failing block becomes larger with the factor of safety being less than 1.0 in most of the scenarios, and thus yielding instability of the slope under study. The slope stability was studied using the developed program only under dry conditions, and no seismic or rainfall loading was taken into consideration.

As presented, quarried slopes stability has been extensively tackled in the literature worldwide, with distinct methods employed to map the slopes and model them. Also, various analysis techniques were adopted to assess their stability under dry conditions or existing state, and in some studies under rainfall and seismic events. All presented literature herein mainly assessed the stability of the quarried slopes as case studies, to make suitable excavation and safety recommendations. Few researchers tested and validated newly developed mapping or analysis techniques (mainly algorithms). No research has set a coherent, time and cost efficient methodology to study the

susceptibility of mined slopes to fail under dry, seismic and rainfall events. In Lebanon, no particular work has been done to assess the stability of quarries that have been mined since the early 90s in a chaotic and widely spread manner. The regional-scale maps developed by Grant et al. (2016), Kaafarani et al. (2019), and Pollock et al. (2019) showed several quarry sites facing high hazard and risk levels. Since the DEM used in the regional scale study was rather coarse (15 m DEM), and in some instance the quarry face might have not been fully captured, the current study takes their work one step further. It aims to develop a site specific methodology for stability of quarried sites. The results will be compared to the predictions of the regional scale maps.

# Chapter Three

## Methodology

The selected quarry was mapped using a DJI Phantom 4 V.2.0 drone. The drone flight was automated in Pix4D Capture employing the double grid mission (i.e. drone follows a grid of horizontal and vertical paths along which it captures the images) (Fig. 10). The sideways and front image overlap was set to 90% and the camera angle was set at 60° from horizontal.

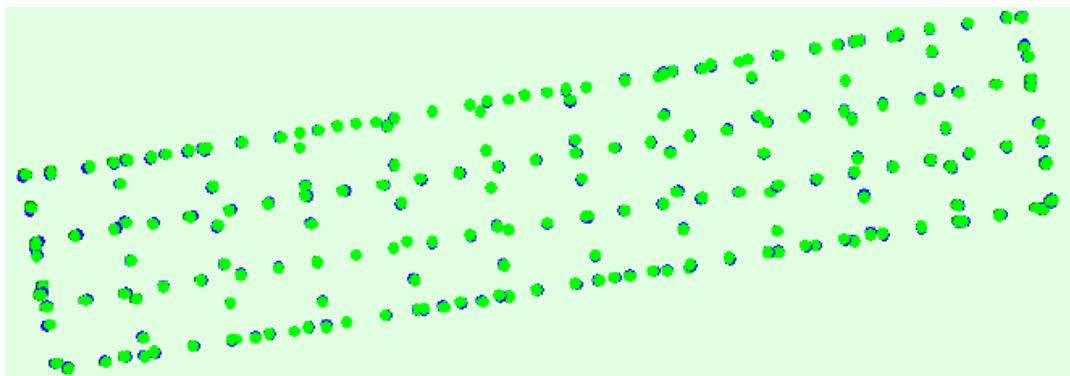


*Figure 10: Offset between initial (blue dots) and computed (green dots) image positions along drone paths*

Several flights with different camera angles from horizontal were required to generate several 3D models of the quarried slope, mainly to increase the probability of capturing the smallest features and details on the quarry face. The high overlap was maintained in each flight to accurately reconstruct and geo-reference the 3D scene. The covered area was 0.1 km<sup>2</sup> approximately, and a total of 210 geo-located images were collected and then processed in Pix4D Mapper version 4.4.12 to recreate the 3D scene (Fig. 11). The high resolution 3D model option in the software was utilized to generate the point cloud, digital surface model (DSM), orthomosaic and 3D texturized mesh. The average ground sampling distance was 2.36 cm and the minimum number of matches was set to 3, meaning that a feature should exist at least in 3 images to be reconstructed in the 3D model. This procedure reduced the noise in the model, especially at its extremities where the drone might have not captured enough images due to the flight path set in Pix4D Capture, resulting in low overlap between the images (Fig. 12). The validation of measurements' accuracy made on 3D models generated in Pix4D Mapper is summarized in Appendix A.



Figure 11: 3D scene recreated in Pix4D Mapper

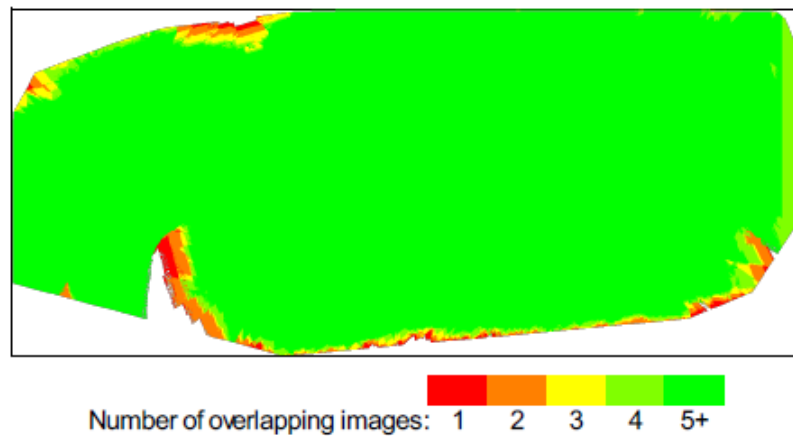


Figure 12: Number of overlapping images above the mapped area

The additional features (i.e. other than the quarry face characteristics) captured in the model were eliminated from the point cloud file using an open source application “CloudCompare”. By visual inspection, the rightmost face of the quarry was found to be highly jointed and has the highest number of persistent discontinuities. To reduce the processing time of the used software programs, this part was extracted as a separate point cloud file in CloudCompare to be further analyzed in detail.

The point cloud, shown in Fig. 13, was later used as input to the Discontinuity Set Extractor (DSE), an open source plugin used in MATLAB to detect discontinuities in rocks and their sets semi-automatically. DSE follows a statistical procedure, based on positioning information stored in the point cloud file to determine joint sets and their orientations. Hence, statistical input parameters were required to establish principal planes: nearest neighbor coefficient, number of bins, minimum angle between principal planes and the maximum number of principal planes. The input values were adopted from Riquelme et al. (2014). The nearest neighbor coefficient  $k_{nn}$  was set to 30, meaning that for a point to be part of a plane, it should be neighboring another 30

points to form a plane altogether. All discontinuity planes were set up using the coplanarity test option in which the algorithm confirmed first that the points are coplanar (i.e. they belong to the same plane) before setting their discontinuity planes. The other parameters were assigned as follows: 64 bins were used for density analysis, 30 degrees were assigned as minimum angle between principal planes, and 10 was used as the maximum number of principal planes.



*Figure 13: Jointed rightmost slope face clipped in CloudCompare*

Then, the cluster analysis was performed to determine the equations of the planes having the below mathematical equation form:

$$Ax + By + Cz + D = 0$$

The discontinuity set orientation was fixed for the sake of cluster analysis, and thus all joints in one discontinuity set would have the same normal vector (same values of A, B and C). Only clusters with a minimum of 100 points were extracted, and the very close ones were merged into one bigger cluster. All other clusters representing jointing with less than 100 points were discarded, as the resulting joints were relatively small and would not contribute in critical failures (Riquelme al., 2014). All detected joint sets in DSE were overlaid on the quarry face in CloudCompare to be validated (Fig. 14), and only the points tracing actual discontinuities were kept while the points tracing parts of the slope surface and curvature were discarded (Fig. 15).





Figure 14: Joints successfully detected using DSE and viewed in CloudCompare

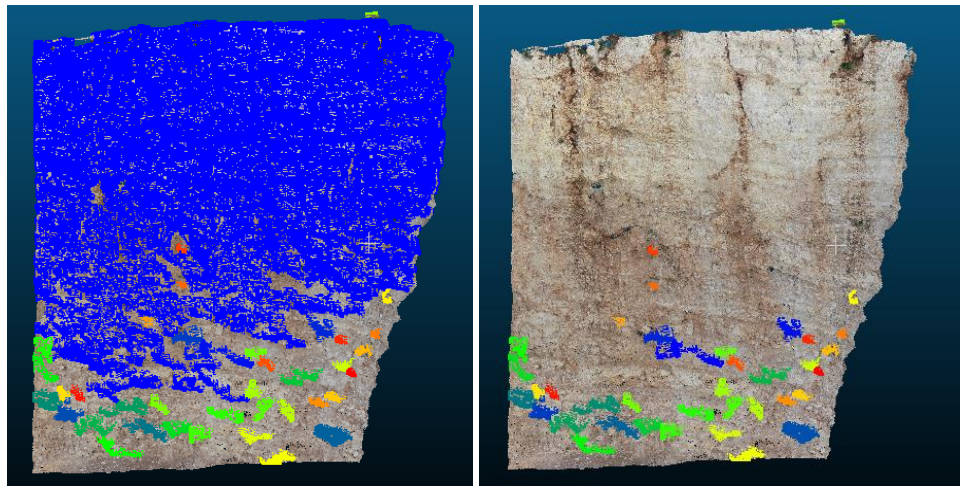


Figure 15: Clusters representing joint set 1 (a) DSE output (b) Cluster representing quarry face discarded

RocScience DIPS 7.0 was utilized to assess the kinematic stability of the jointed rock face at hand using equal angle, pole mode, and lower hemisphere stereographic projection representation. Friction angle and slope dip direction were the input required by the software, in addition to a lateral limit parameter required for two failure modes. The slope dip direction was corrected for magnetic declination, which was determined to be  $+5^{\circ}$  based on the site location. The susceptibility to flexural toppling, planar sliding, wedge sliding, oblique and direct toppling was assessed and the probability for each mode of failure was obtained. A lateral limit of  $20^{\circ}$  was used in planar sliding analysis and  $30^{\circ}$  was used in flexural toppling analysis (Goodman 1980, Hudson and Harrison 1997).

Mode-specific software were then adopted to analyze the failure modes with the highest probability of occurring, and determine the corresponding factor of safety

under dry conditions, as well as rainfall and seismic events. In case of planar failure, RocScience RocPlane is usually adopted, while in case of toppling failure, RocScience RocTopple is employed, and in case of wedge sliding RocScience SWEDGE is used. In this research, only RocScience SWEDGE 6.0 was used given that wedge sliding had the highest probability of occurring. The potential critical intersecting joints were determined from DIPS and were analyzed in SWEDGE using limit equilibrium methods, and corresponding factors of safety were determined. The Barton-Bandis criterion for jointed rock mass was used in the analysis of joints since its parameters are directly related to the discontinuities themselves, rather than the intact rock. A residual friction angle of  $35^\circ$ , joint roughness coefficient (JRC) of 10 and joint compressive strength (JCS) of 51.74 MPa were assigned for the limestone material based on RocData, a RocScience database for soil properties and models, based on the rock description and observations made on site. Slope dimensions were assigned in SWEDGE, such as the slope height, dip and dip direction (corrected for magnitude declination), and its length which was assigned a value of 51 meters in this case corresponding to the length of the section under study. Also the upper bench dip ( $10^\circ$ ), dip direction (dipping in the same direction as the slope), and the width (assumed to be 50 meters to prevent illogically massive wedges from forming) were used as input values in SWEDGE.

The results of limit equilibrium methods were checked against those obtained from finite element methods. In this case, RocScience RS2 was chosen to conduct the numerical analysis on the slope face. The intact rock mass was modelled using the Generalized Hoek-Brown criterion, and the input parameters for the intact rock were determined from RocData based on the rock description (Table 2). The “joint network” option in RS2 was used to model the intersecting joint sets. The parallel deterministic joint model was used as the dip and dip direction are known. However, since the orientation of the joint sets is in the 3D space, and a 2D model is constructed, a trace plane needed to be defined to convert the orientation to 2D. A trace plane is assumed to be a vertical cross section of the slope and thus its dip direction is needed to be used as input. This dip direction is the azimuth of the normal vector of the trace plane, pointing into the screen and measured clockwise from the north. The determination of the trace plane is shown in Fig. 16: The dip direction of the slope is  $355^\circ$  measured clockwise (which is  $5^\circ$  measured counter clockwise). The trace plane is perpendicular



to the slope face at all times, and thus the normal vector of the trace plane is perpendicular to the normal vector of the slope plane at all times. Hence, the clockwise angle between the north and the normal vector to the trace plane is  $85^\circ$ .

The length and spacing of the discontinuities were determined from CloudCompare as average values, and all joints are assumed to be fully persistent and thus will yield conservative results as non-persistent discontinuity usually has a higher shear strength than a persistent discontinuity. Absence of actual data about joints persistence, one of the most significant discontinuity parameters, is a key factor of this assumption as well, as it is practically impossible to measure the discontinuity area even in field investigations (Park et al., 2005). Similar to LEM, the Barton-Bandis criterion was used for joint modelling along with the previously determined parameters. In this analysis however, the actual infiltration rate (103 mm/day) determined from available rainfall data maps in GIS (Plassard, 1971) was used as a boundary condition on the slope face and top bench to calculate the safety factor rather than using a saturation value like in LEM.

Table 2: Intact rock properties used in RS2

Parameter	$\nu$	E (MPa)	UCS (MPa)	mb	s	a	mi
Value	0.25	8371.70	75.00	1.17	0.001	0.51	10.00

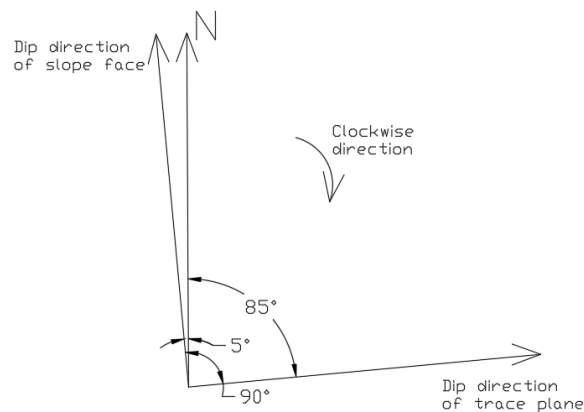


Figure 16: Trace plane orientation determination

The meshing option for all calculations was set to a uniform mesh type with 6-noded triangle elements and an approximate number of mesh elements of 1000 elements. As for the boundary conditions, the right most and bottom boundaries were restrained from moving in both X and Y directions. A window was specified for the SSR (shear

strength reduction: used to calculate the factor of safety) analysis in some cases. This window covers only the face of the slope where failure possibility was investigated. This is because in some cases, the critical deformation pattern, or failure was observed along the upper slope (bench) where the joints are intersecting, and it is not certain that joints are persistent up to the upper bench face.

The expected runout distance and angle of reach were calculated using the rigid body option available in RocScience RocFall. The seeder (i.e. point of rock mass release) was assumed to be at the highest point of the slope, in order to generate the highest potential energy and thus the highest runout distance. It should be noted that RocFall employs probabilities to determine the runout distance, therefore, ten rocks were thrown from the seeder point in order to cover all possible runout distances, and the distance with the highest probability was reported. The initial velocity of the sliding rock wedges was assumed to be zero since the rock detaches under the applied load and slides in free fall. The weights of the possible wedges were obtained from RocScience SWEDGE for a persistence of 50 m, which is equal to the bench extension in RS2, in order to avoid illogically massive wedge formation. Both tangential and normal restitution coefficient values were assigned as in Azzoni et al. (1995), and dynamic and rolling friction coefficient mean values were assigned as in Robotham et al. (1995). The slope roughness spacing and amplitude were simply measured from the 3D model in Pix4D Mapper. All input parameters used in RocFall are summarized in Table 3. The roughness parameters were neglected for the ground, since it is very smooth as observed on site, and only the restitution and friction values given in Table 3 were assigned to the slope face.

The relevant output of the analysis was the maximum distance from the slope face that could be reached if a failure occurs, and based on it the angle of reach, represented by  $\alpha$  in Fig. 17 (i.e. the angle formed between the horizontal line extending from the seeder and a line joining the seeder and the stop point of the rock mass) could be calculated.

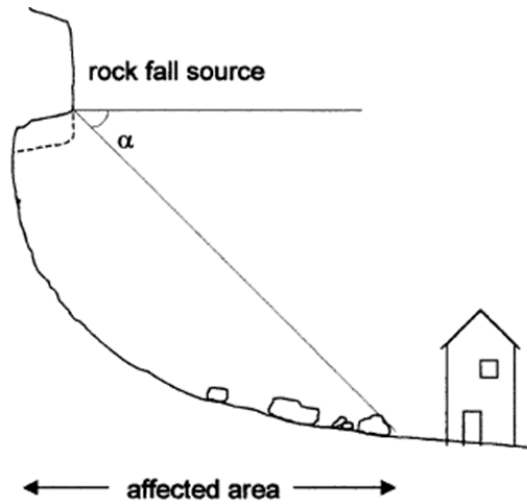


Figure 17: Angle of reach illustration

Table 3: Input parameters used in RocFall

<b>Restitution Coefficient</b>	
Normal	Tangential
0.32	0.71
<b>Friction Coefficient</b>	
Dynamic	Rolling
0.42	0.40
<b>Slope Roughness</b>	
Spacing (m)	Amplitude (m)
0.5	0.01

The site in Bafliyeh was selected because it was relatively easy to fly a drone over the area and take the necessary images. However, the multi-modal analysis of Grant et al. (2016) and Kaafarani et al. (2019) did not fully capture this quarry in Bafliyeh due to the coarseness of the digital elevation model (DEM). Thus, there was no failure predicted in this quarry under rainfall and earthquake events. In order to complete this work and compare the results to the regional scale hazard maps, another slope with similar geometry and geology was identified. This was done by overlaying the quarries location and geology maps on top of the regional scale hazard map in GIS ArcMap, and by calculating the elevation profile at several quarried sites with similar geology. The 3D analyst tool was employed and the interpolate line option was used to obtain the elevation profile of the terrain (Fig. 19). Fig. 19 shows the elevation in meters versus the horizontal distance in meters at the chosen site, and both were used to infer the slope of the terrain. A slope in the region of Halate, Jbeil was found to have similar geometry and geology, and indicated a potential for wedge sliding under rainfall and

seismic events, similar to the Bafliyeh slope. A Google Earth image of the selected site is presented in Fig. 18. The factors of safety obtained in the site specific analysis were compared with the regional scale assessment of the Halate slope, as well as the reach angles and sliding block weights.



Figure 18: Google Earth image of the quarried slope detected in Halate, Jbeil

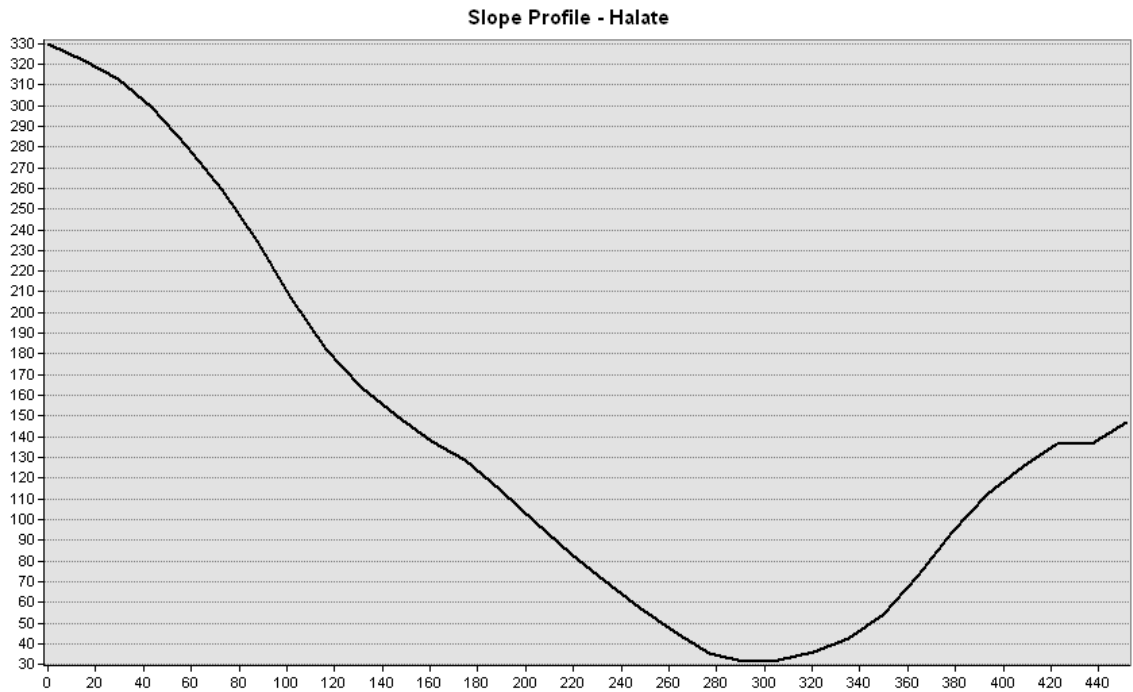


Figure 19: Elevation profile generated using 3D Analyst tool in GIS for Halate quarry

The entire methodology is summarized in Fig. 20.

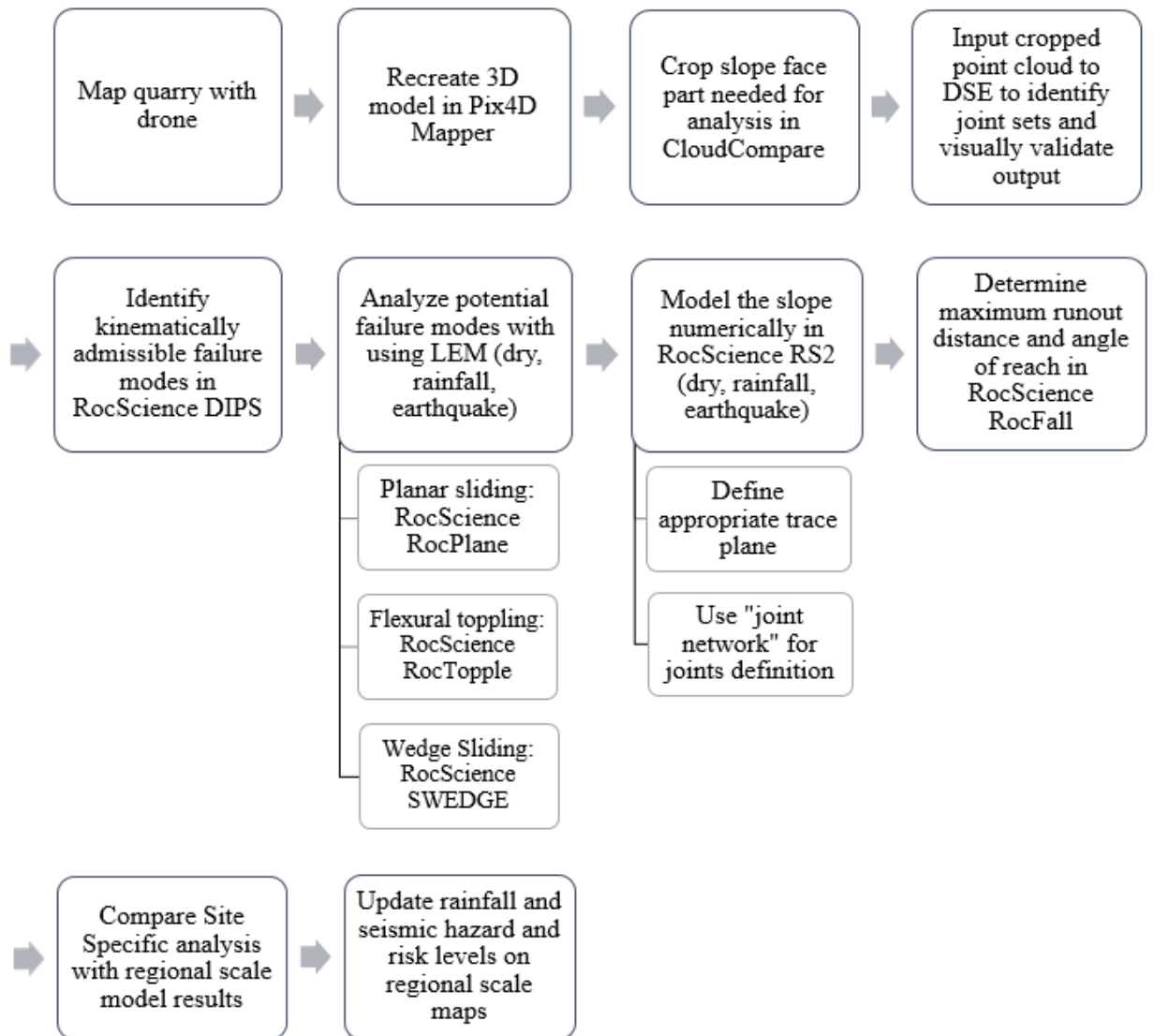


Figure 20: Methodology summary chart

# Chapter Four

## Results and Discussion

### 4.1 Site Specific Analysis

#### 4.1.1 Semi-automatic Joint Set Detection Output

A total of ten joint sets are detected in DSE and their dip and dip direction are summarized in Table 4. Colored clusters in Fig. 11b represent the first joint set indicated in Table 4 (Dip =  $3.86^\circ$  and Dip direction =  $315^\circ$ ), and it is comprised of 36 short discontinuities. By visual inspection, the detected joints are almost parallel, and hence they do belong to the same joint set. The remaining joint sets were inspected and confirmed similarly. Most of the calculated joint planes were found to be perfectly tracing joints that are visibly detectable in the point cloud in Cloud Compare, and on the 3D model in Pix4D Mapper, and thus they were validated. This visual validation was necessary as the detection of joint sets using DSE is not fully automatic, since the software might detect parts of the slope face or vegetation as discontinuities.

Table 4: Joint sets identified in DSE

Joint Set	1	2	3	4	5	6	7	8	9	10
Dip (°)	3.86	56.72	56.72	44.14	58.53	76.34	91.36	91.36	90.61	89.71
Dip Direction (°)	315	41.42	318.58	356.63	347.74	1.74	1.33	91.33	105.02	158.96

#### 4.1.2 Kinematic Analysis

The kinematic analysis of the discontinuities in DIPS showed that planar sliding will occur on 22.33% of the discontinuities, flexural toppling will take place on 22.06% of the joints, wedge sliding will happen on 46.10% of joint intersections, while direct toppling has no chance of occurring and oblique toppling will be expected on 4.89% of discontinuities intersections.

##### 4.1.2.1 Planar Sliding

Joint sets 4 and 5 fall in the region outside the friction cone and within the daylight envelope or in the critical area for planar sliding failure (Fig. 22a). Sets 4 and 5 are intersecting joint sets, as inspected in CloudCompare and DIPS, and are prone to sliding as wedges since the chance of them sliding as a wedge is much higher than individual joints sliding as planes.

#### 4.1.2.2 Flexural Toppling

Joint sets 7 and 10 fall in the critical region of flexural toppling (closed zone formed by the slip limit and lateral limits). Both joint sets are nearly vertical (dip of  $90^{\circ}$ ) (Fig. 22b), which explains their susceptibility to fail by flexural toppling. By inspecting the 3D model (Fig. 11), joint set 7 is composed of vertical short discontinuities that are a result of excavation activities and are focused on the lower part of the slope. These discontinuities are not persistent into the slope face and thus there are no back to back formed rock columns that would cause flexural toppling failure by rotating around the base. Joint set 10 (Fig. 21a) has a massive block that can topple at the top of the slope, but the left joints of the block are not developed enough to cause the block to detach from the slope face and fail by toppling. In addition, the area of the block face was calculated in CloudCompare (Fig. 21b) and was determined to be 207.38 m<sup>2</sup>, which results in a weight of approximately 4769.74 kN using the unit weight of limestone (23 kN/m<sup>3</sup>), and by assuming a 1 meter depth into the slope face. The block weight is a large force acting downwards, and thus it will act against external applied loads, enforcing again the very low probability of this scenario occurring. On the other hand, the right and base discontinuities of the block that are extending to the upper surface have a higher tendency to fail in a wedge sliding mode given that they are more developed and fractured. Therefore, this mode will not be analyzed further, as it is unlikely to occur on the slope face.

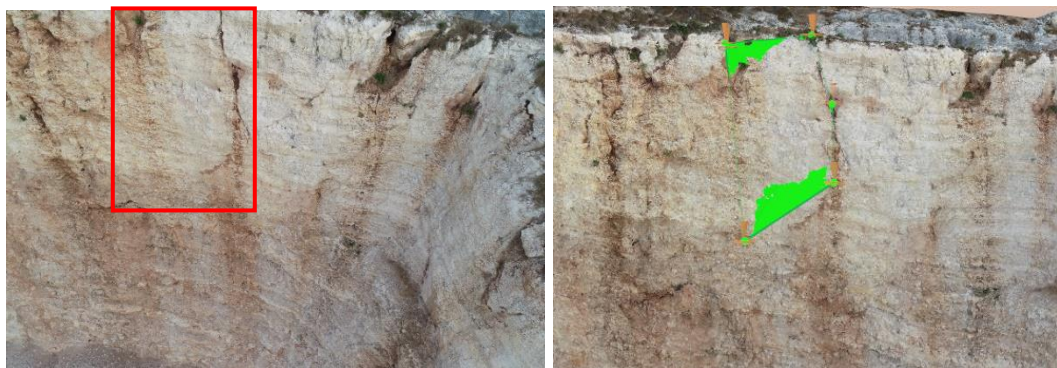


*Figure 21: (a) Rectangular block detected in joint set 10 (b) Area delineated for calculation in CloudCompare*

#### 4.1.2.3 Wedge Sliding

Wedge sliding has the highest probability of occurring with 46.10% of joints intersections prone to sliding. Fig. 22c shows the stereographic representation of all



discontinuity planes intersections and those vulnerable to wedge sliding as well, highlighted in the crescent shaped critical area.

#### 4.1.2.4 Direct and Oblique Toppling

The analysis of direct and oblique toppling resulted in no chance of direct toppling for intersecting joints and a 4.89% probability of oblique toppling which is considered very low and thus this mode of failure is not analyzed further (Fig. 22d).

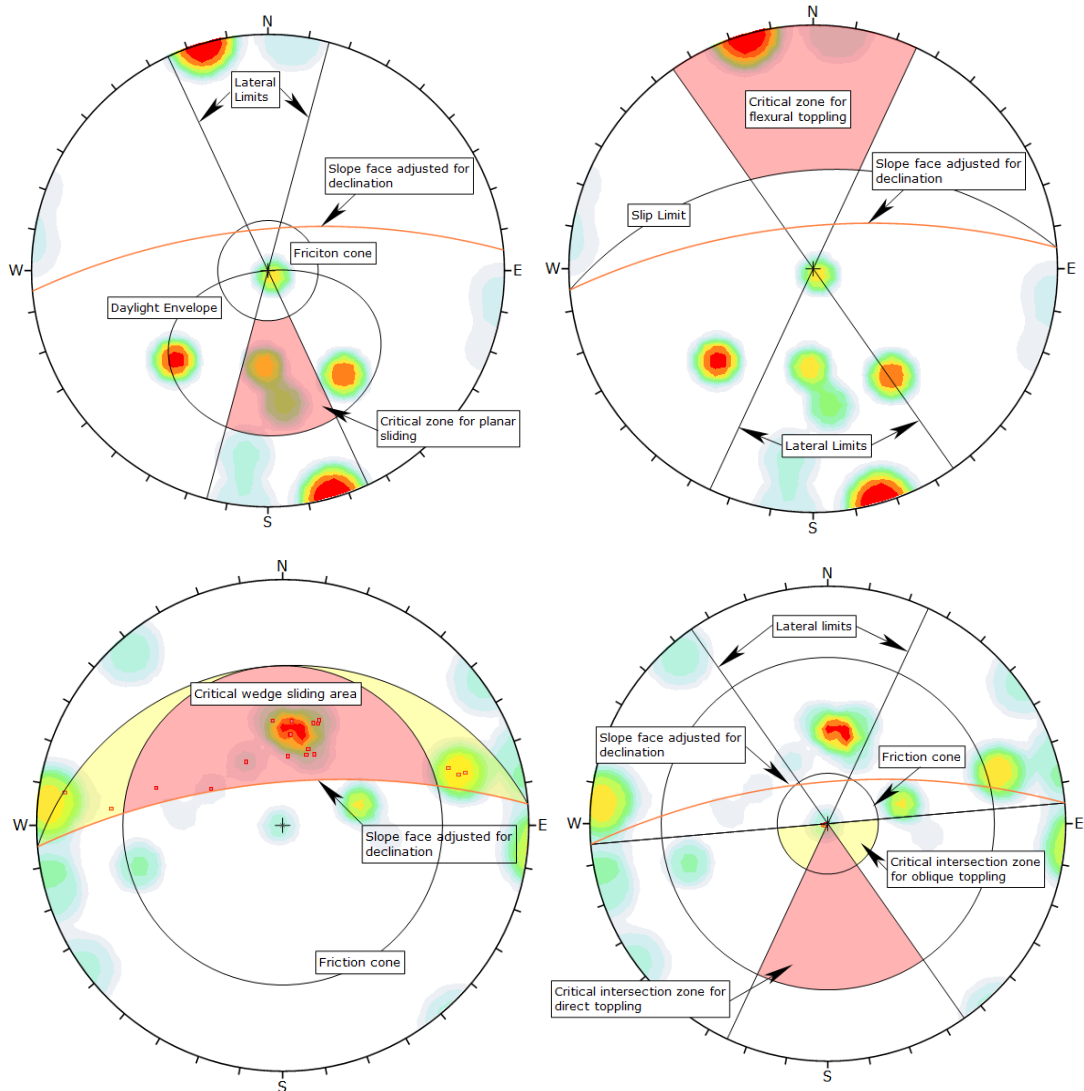


Figure 22: Kinematic analysis (a) Planar sliding (b) Flexural toppling (c) Wedge sliding (d) Direct and oblique toppling

#### 4.1.3 Limit Equilibrium Analysis

Eighteen pairs of intersecting joints were kinematically subject to wedge sliding and were carried for further analysis in SWEDGE using limit equilibrium methods. The analysis was performed using the deterministic analysis where the intersecting joints' dip and dip directions, joints strength parameters and slope characteristics were



directly used as input, instead of depending on the software in determining the possible intersections. The analysis of all intersections is presented in Appendix B and their factors of safety are summarized in Table 5 under dry and wet conditions, as well as under possible seismic events.

*Table 5: Factors of safety determined from SWEDGE under dry and wet conditions, as well as seismic loading*

<b>Joint Set Intersections</b>	<b>F.S (Dry Conditions)</b>	<b>F.S (Wet Conditions)</b>	<b>F.S (Seismic Loading)</b>
<b>JS 5 and JS 6</b>	1.53	1.48	1.22
<b>JS 2 and JS 3</b>	1.94	1.93	1.21
<b>JS 5 and JS 3</b>	1.42	1.41	0.86
<b>JS 2 and JS 4</b>	2.15	2.15	1.36
<b>JS 8 and JS 4</b>	1.81	1.81	1.16
<b>JS 3 and JS 4</b>	1.81	1.80	1.15
<b>JS 9 and JS 4</b>	1.82	1.81	1.17
<b>JS 9 and JS 3</b>	4.68	4.67	2.97
<b>JS 2 and JS 8</b>	2.98	2.97	1.86
<b>JS 3 and JS 8</b>	3.05	3.04	1.90
<b>JS 2 and JS 9</b>	2.25	2.23	1.36
<b>JS 8 and JS 5</b>	1.58	1.57	0.91
<b>JS 9 and JS 5</b>	2.00	2.00	1.19
<b>JS 2 and JS 5</b>	1.48	1.47	0.89
<b>JS 6 and JS 4</b>	37.67	37.63	11.43
<b>JS 5 and JS 4</b>	1.79	1.78	1.45
<b>JS 10 and JS 4</b>	1.83	1.82	1.52
<b>JS 10 and JS 5</b>	20.50	20.47	9.67

Under dry conditions, intersecting joint sets 3 and 5 yield the lowest factor of safety of 1.42, as shown in Fig. 23a. A slope is considered stable when the factor of safety is greater than 1.3 (Hoek et al., 1981). The results of the analysis under dry conditions are confirmed by the observations made on site, where no failure was detected.

Under wet conditions, the factor of safety of Joint sets 3 and 5 slightly decreases to 1.41 (Fig. 23b). This slight decrease in the factor of safety is expected, given that the water is occupying 17% of the joint height, which decreases the friction between joint asperities, and thus makes the susceptibility to wedge sliding higher.

The same wedge has the lowest factor of safety of 0.86 under horizontal seismic loading (Fig. 23c), indicating definite failure under possible earthquake events. Under seismic events, other wedges are also found unstable, like the wedges formed by the intersections of joint sets 5 and 6, 2 and 3, 8 and 4, 3 and 4, 9 and 4, 8 and 5, 9 and 5, and 2 and 5. These joint intersections have a factor of safety less than 1.3, and thus impose high risks under seismic events given their definite failure. This result is

expected from visual inspection of slope face on site, where it can be clearly seen that the apertures of the joints are wide, the fractures are well developed, and the wedges are abundant, especially in the area under analysis. Therefore, under cyclic excitation and ground acceleration, these wedges are expected to detach from the rock face and cause damages in their extent of influence.

From SWEDGE analysis for intersection of joints 3 and 5, the sliding of the block is expected to occur in all three scenarios on joint 5, as it is the more exposed joint with the easiest and steepest path for the wedge to follow in case of failure.

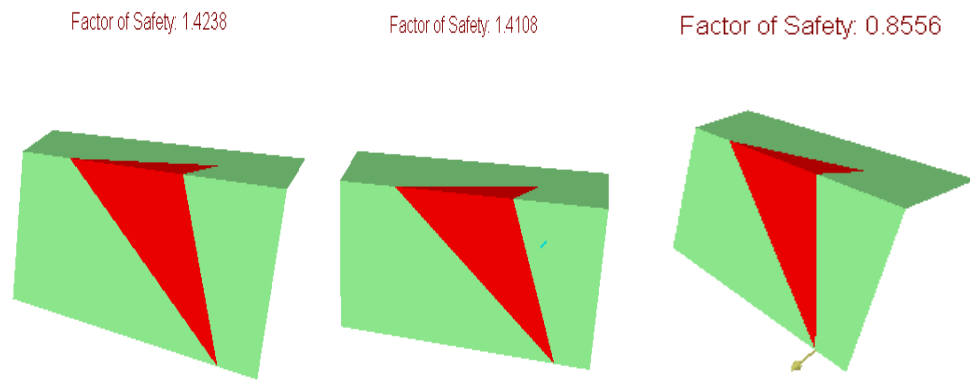


Figure 23: Factor of safety of the wedge formed by JS 5 and JS 3 (a) Dry conditions (b) Wet conditions (c) Seismic loading

The very high factors of safety obtained from intersecting joints 10 and 5 for example, are due to the high persistence of the joints in the rock material into the bench (283.61 m and 384.89 m). As a result, not only the wedge is larger and heavier, but its susceptibility to fail is smaller as it needs to overcome the friction existing between joints asperities over the extensive length. These two factors play a role in increasing the resisting forces significantly compared to the applied external loads, and hence increasing the factor of safety (Fig. 24).

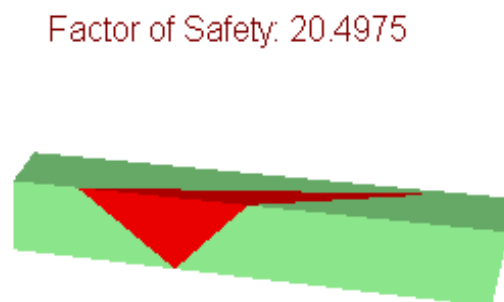


Figure 24: Factor of safety of intersecting joint sets 10 and 5 under dry conditions

#### **4.1.4 Numerical Modelling Analysis**

The factors of safety were determined from the numerical modelling of the slope in RS2 using finite element methods for the same joint sets previously presented.

Using FEM, the lowest factor of safety of 1.41 occurs on the same intersecting joint sets 3 and 5 (Fig. 25) under dry conditions, which is similar to the one obtained in LEM with a 0.98% difference. The wedge-like failure shape is occurring where total displacement contour is maximum with a red color, and is developing along the steepest joint set (joint set 5), which constitutes the easiest path for failure progression. However, under wet conditions (i.e. an infiltration rate of 103 mm/day), intersecting joint sets 4 and 5 prove to be more critical with a safety factor of 1.19, making the slope unstable ( $F.S < 1.3$ ), whereas it was considered safe in LEM with a factor of safety of 1.41 (Fig. 26). For this scenario, a larger wedge is developing along the slope profile with the maximum displacement being concentrated in the lower section of the slope on the intersection formed by both joint sets, with the sliding mostly occurring on joint set 4. This variation is expected, given that the actual rainfall intensity is used in the analysis based on the slope location and the saturation level is calculated automatically in RS2 based on the joints orientations, rather than using a universal scaled saturation value for all scenarios. Under seismic events with a predicted PGA of 0.25g, failure is anticipated in intersecting joint sets 10 and 4 with an obtained safety factor of 0.97 (Fig. 27), which is greater, and not consistent with the one obtained from LEM in SWEDGE. The failure is expected to occur on the highest section of the slope, and to develop along the nearly-vertical joint set 10. The analysis of the remaining intersecting joints is presented in Appendix C.

#### **4.1.5 Comparison between LEM and FEM**

Factors of safety obtained from both LEM and FEM for all joint intersection possibilities are summarized in Table 6 for dry conditions, rainfall and seismic events. All potential wedges prove to be safe under dry conditions using both analysis types, which can be confirmed by the observations made on site, where no failure signs were detected. Under rainfall events however, LEM predicts that the slope will remain stable, whereas FEM predicts that 7 wedges out of 18 will fail, with one being just at the verge of failure with a factor of safety of 1.29. For seismic conditions, LEM predicts that failure will occur on half of the joint intersections, while FEM confirms that 12 wedges are prone to fail. However, the predicted failures are not always on the

same intersecting joints. For example, the wedge formed by intersecting joints 2 and 3 fails in LEM under seismic events with a factor of safety of 1.21, while it stays safe in FEM with a factor of safety of 1.39 (which is not very far from failure). On the other hand, the wedge created by intersecting joints 2 and 8 is unstable in FEM (F.S = 1.19), and stable in LEM (F.S = 1.86).

The factors of safety obtained from FEM are mostly lower than those obtained from LEM for all scenarios, since the analysis done using RS2 is more detailed and requires all information relating to intact rock, joints, and loading applied. It can be noticed also that using FEM analysis, the highest factor of safety obtained is 1.75 compared to 37.67 in LEM (both under dry conditions), which occurred in a different joint set intersection, further enforcing the reliability of RS2 analysis in predicting failure susceptibility, as the factors of safety obtained are more realistic.

This discrepancy is expected because of the limitations of LEM previously described in Chapter 2. In addition, in FEM in RS2, the user has more control over joints properties such that persistence, length and spacing, that can be used as input. This is not an available option in SWEDGE, where the user can only use the dip and dip direction as input, and the software assumes the persistence and length, which might not be representative of the actual measurements made on the slope face. In RS2, the intact rock mass is modelled using a different shear strength model than the joints (Generalized Hoek-Brown for intact rock and Barton-Bandis for joints), while in SWEDGE, a shear strength model is only used for joints, and thus RS2 better simulates the case at hand and better represents the real-life scenario. Nevertheless, these factors of safety present simply an indication of stability rather than confirmation. No model is totally accurate without field observation and validation.

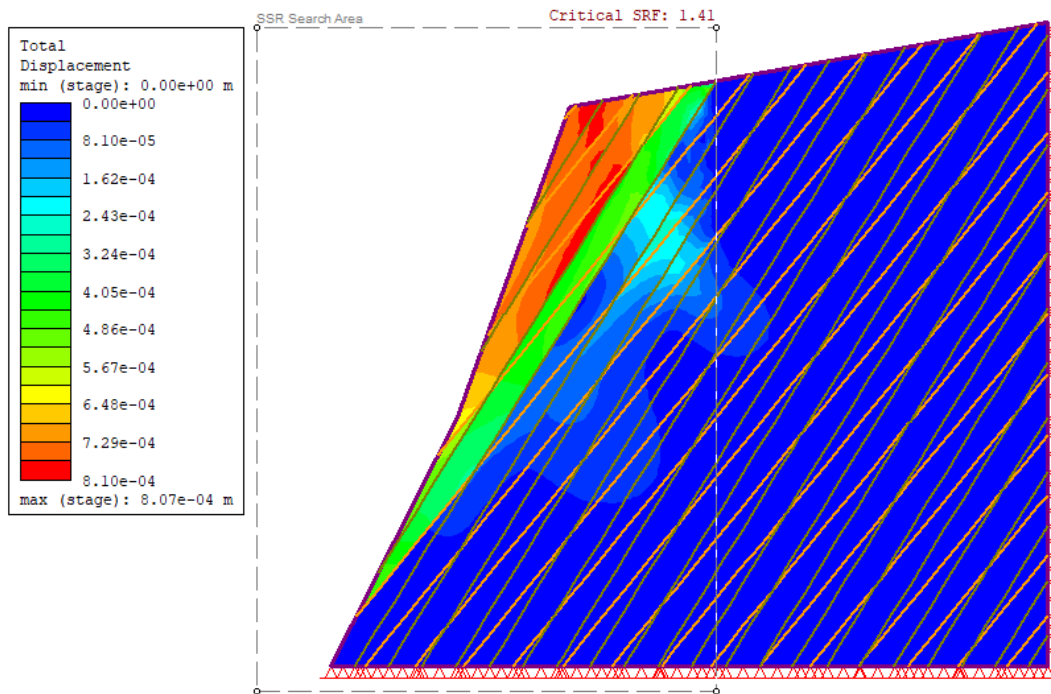


Figure 25: Slope elevation with joint sets 3 and 5 under dry conditions in RS2

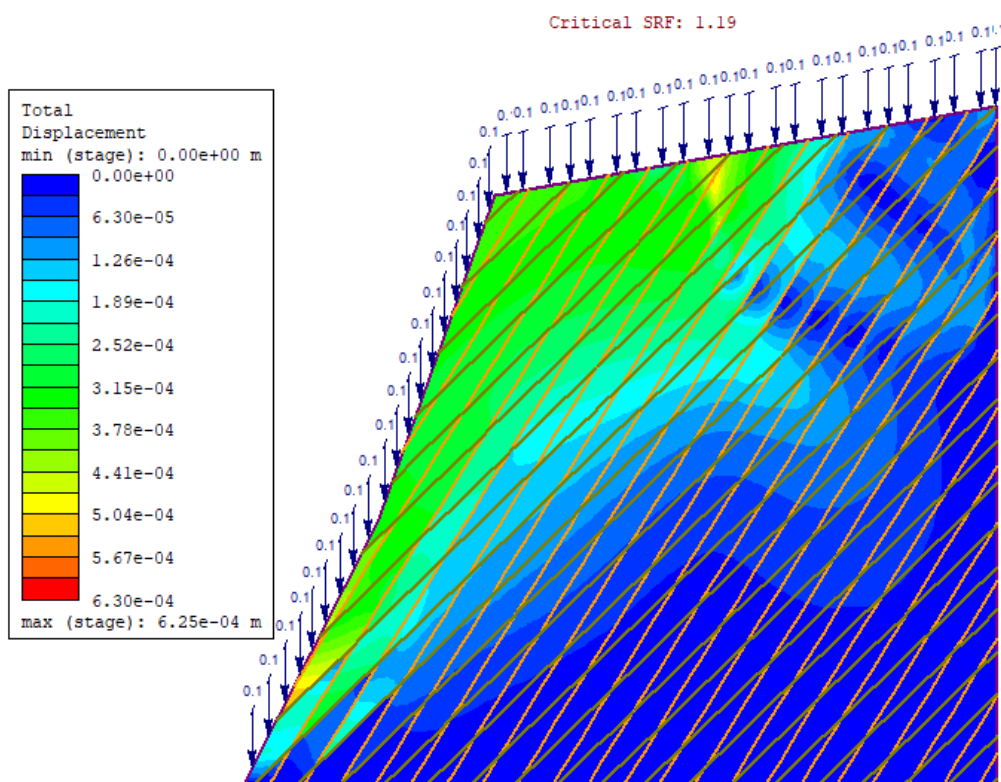


Figure 26: Slope elevation with joint sets 4 and 5 under wet conditions in RS2

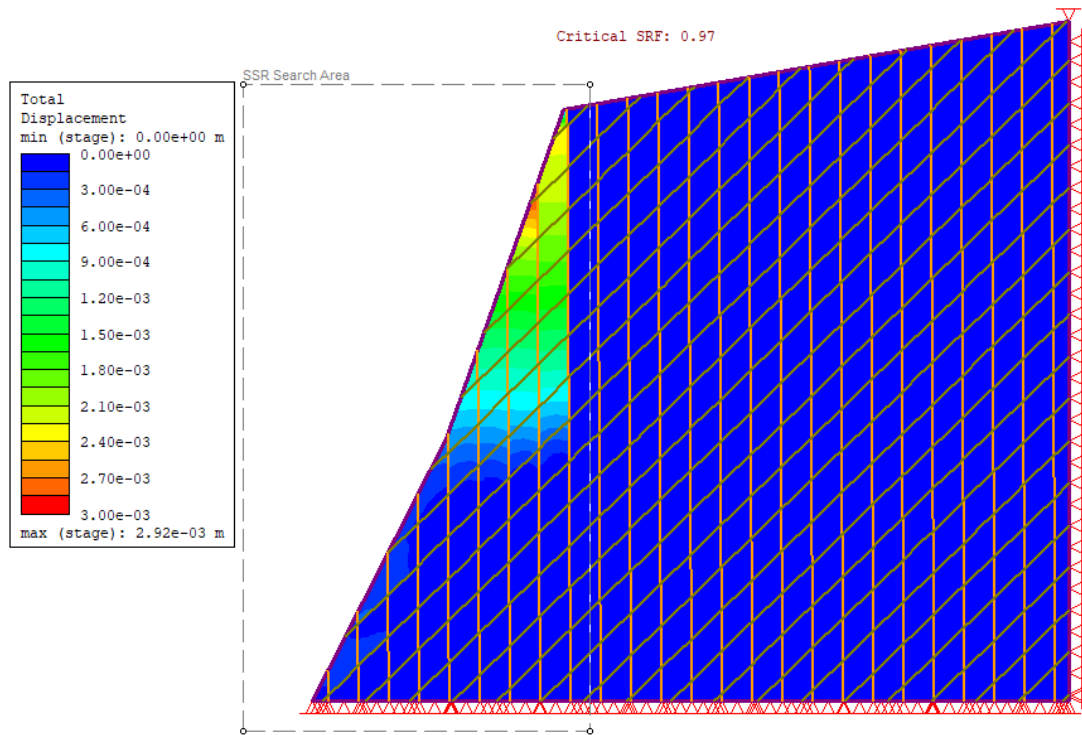


Figure 27: Slope elevation with joint sets 10 and 4 under static seismic loading in RS2

Table 6: Comparison between LEM and FEM results under all scenarios

JS Intersections	Dry Conditions		Rainfall Event		Seismic Event	
	F.S (LEM)	F.S (FEM)	F.S (LEM)	F.S (FEM)	F.S (LEM)	F.S (FEM)
JS 5 and JS 6	1.53	1.50	1.48	1.23	1.22	1.19
JS 2 and JS 3	1.94	1.57	1.93	1.40	1.21	1.39
JS 5 and JS 3	1.42	1.41	1.41	1.32	0.86	1.29
JS 2 and JS 4	2.15	1.65	2.15	1.45	1.36	1.43
JS 8 and JS 4	1.81	1.76	1.81	1.45	1.15	1.30
JS 3 and JS 4	1.81	1.58	1.80	1.35	1.15	1.41
JS 9 and JS 4	1.82	1.78	1.81	1.46	1.17	1.26
JS 9 and JS 3	4.68	1.55	4.67	1.34	2.97	1.37
JS 2 and JS 8	2.98	1.68	2.97	1.39	1.86	1.19
JS 3 and JS 8	3.05	1.57	3.04	1.36	1.90	1.10
JS 2 and JS 9	2.25	1.68	2.23	1.36	1.36	1.45
JS 8 and JS 5	1.58	1.49	1.57	1.28	0.91	1.02
JS 9 and JS 5	2.00	1.49	2.00	1.28	1.19	1.40
JS 2 and JS 5	1.48	1.60	1.47	1.51	0.89	1.11
JS 6 and JS 4	37.67	1.60	37.63	1.25	11.43	1.27
JS 5 and JS 4	1.79	1.44	1.78	1.19	1.45	1.29
JS 10 and JS 4	1.83	1.75	1.82	1.21	1.52	0.97
JS 10 and JS 5	20.50	1.45	20.47	1.29	9.67	1.02

#### 4.1.5 Maximum Runout Distance and Angle of Reach

The maximum runout distance, or the maximum distance from the slope face to the stop point reached when the wedge detaches from the slope face is determined from

RocFall as 12.68 m for intersecting joints 2 and 3. This distance is associated also with intersecting joint sets 9 and 3, 8 and 3 and these are the wedges with the largest weights, and thus they have the highest potential energy and will travel farther distances. The angle of reach based on this maximum distance is 77.77°. However, for all previously determined failing intersecting joint sets in both SWEDGE and RS2, which have smaller wedge weights, this runout distance is 7.76 m from the slope’s face, and corresponds to a reach angle of 82.44°. Therefore, it is the one more likely to occur in case of failure. Table 7 summarizes all possible wedges weights determined from SWEDGE, their runout distances and angles of reach obtained in RocFall. An example of a RocFall output is presented for intersecting joint sets 5 and 2 in Fig. 28. Fig. 28 shows the slope geometry in white, and the histogram representing the probability of wedges failing from the slope’s crest to reach several locations away from the slope face, and then the farthest possible distance with the highest probability of reaching is taken as the maximum runout distance. In the case represented herein, all rocks triggered by the software from the top of the slope reached a distance of 10.22 m away from the face, and thus this value is reported for the wedge formed by discontinuities sets 2 and 5 in Table 7.

*Table 7: Wedges weights and their possible runout distance and angles of reach obtained from RocFall*

<b>Joint Set Intersections</b>	<b>Weight (MN)</b>	<b>Runout distance (m)</b>	<b>Angle of Reach (°)</b>
<b>JS 5 and JS 6</b>	2.78	5.30	84.82
<b>JS 2 and JS 3</b>	99.39	12.68	77.77
<b>JS 5 and JS 3</b>	12.66	7.76	82.44
<b>JS 2 and JS 4</b>	0.64	5.30	84.82
<b>JS 8 and JS 4</b>	0.66	5.30	84.82
<b>JS 3 and JS 4</b>	0.67	5.30	84.82
<b>JS 9 and JS 4</b>	0.65	5.30	84.82
<b>JS 9 and JS 3</b>	52.74	12.68	77.77
<b>JS 2 and JS 8</b>	46.10	10.22	80.09
<b>JS 3 and JS 8</b>	53.33	12.68	77.77
<b>JS 2 and JS 9</b>	32.02	10.22	80.09
<b>JS 8 and JS 5</b>	22.82	7.76	82.44
<b>JS 9 and JS 5</b>	26.24	10.22	80.09
<b>JS 2 and JS 5</b>	30.24	10.22	80.09
<b>JS 6 and JS 4</b>	0.33	7.76	82.44
<b>JS 5 and JS 4</b>	0.63	7.76	82.44
<b>JS 10 and JS 4</b>	0.53	7.76	82.44
<b>JS 10 and JS 5</b>	4.79	7.76	82.44

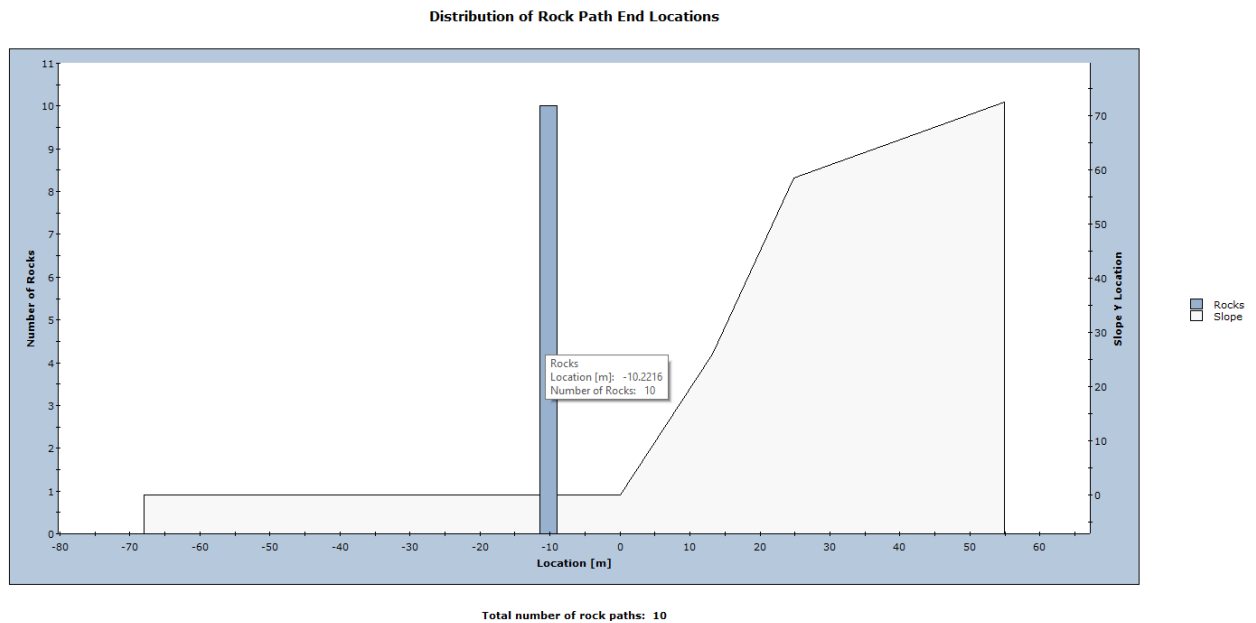


Figure 28: End location of wedge formed by joint sets 2 and 5 in case of failure as taken from RocFall

## 4.2 Comparison with Regional Scale Assessment

Using the available DEM with a resolution of  $15\text{ m} \times 15\text{ m}$ , the elevation profile of the Bafliye quarry is generated in ArcMAP and a slope steepness of  $23^\circ$  is obtained. The actual slope measured for the site is  $70^\circ$  (Fig. 29). In general, the regional scale assessment considered the Bafliye quarry as prone either to debris flow or coherent rotational slides given its gentle inclination and mild slope in DEM. No signs of failure were observed on the rainfall and seismic regional hazard maps of Grant et al. (2016) and Kaafarani et al. (2019).

Due to the coarseness of the available DEM used in the regional scale map, and hence its inability to detect the Bafliye slope under study, and given the need to confirm the proposed methodology, a quarry with similar slope, geology and climate conditions was chosen for comparison purposes. A quarried site in Halate, Jbeil having approximately the same slope inclination ( $63.5^\circ$ ) and detected by the regional scale as prone to wedge sliding was selected. By overlaying the quarries layer on top of the Dubertret geology map in Google Earth, both quarries are found to have the same geology (limestone) (Fig. 30). Both quarries exist in same climate conditions, and thus they have the same rainfall intensity (0.103 mm/day) that will produce the same saturation level of 17% (Fig. 31). Also, the peak ground acceleration at both sites is the same at 0.25g (Huijjer et al., 2011). Fig. 32 shows the rain hazards (pink pixels) near and on the quarried site (grey polygon). The raster representing the factor of



safety for a design storm having a 10 years return period average was converted to a point file, and only the points inside the quarry were selected as highlighted in blue in Fig. 33. The smallest value in the factor of safety raster for the selected site under rainfall events is 1.02 which is lower than the one obtained from site specific analysis (FEM result: 1.19), with a difference of 14.3%. Both analysis types yield an unsafe slope and predict its failure under rainfall events, with the regional scale being more conservative with a lower factor of safety. The obtained results validate the ability of the regional scale to roughly predict rainfall hazards at quarried sites.

Under seismic events, the regional scale assessment predicts critical displacements that yield the slope to failure, rather than calculating a factor of safety. The critical displacement determined from regional scale analysis for the Halate quarry is 0.29 cm compared to 0.3 cm in site specific analysis of the Bafliye quarry (Fig. 27). The difference obtained between these values is 3.33% which can be considered negligible, and thus confirms the ability of the regional scale model to predict failures under seismic events in quarried slopes using few input parameters.

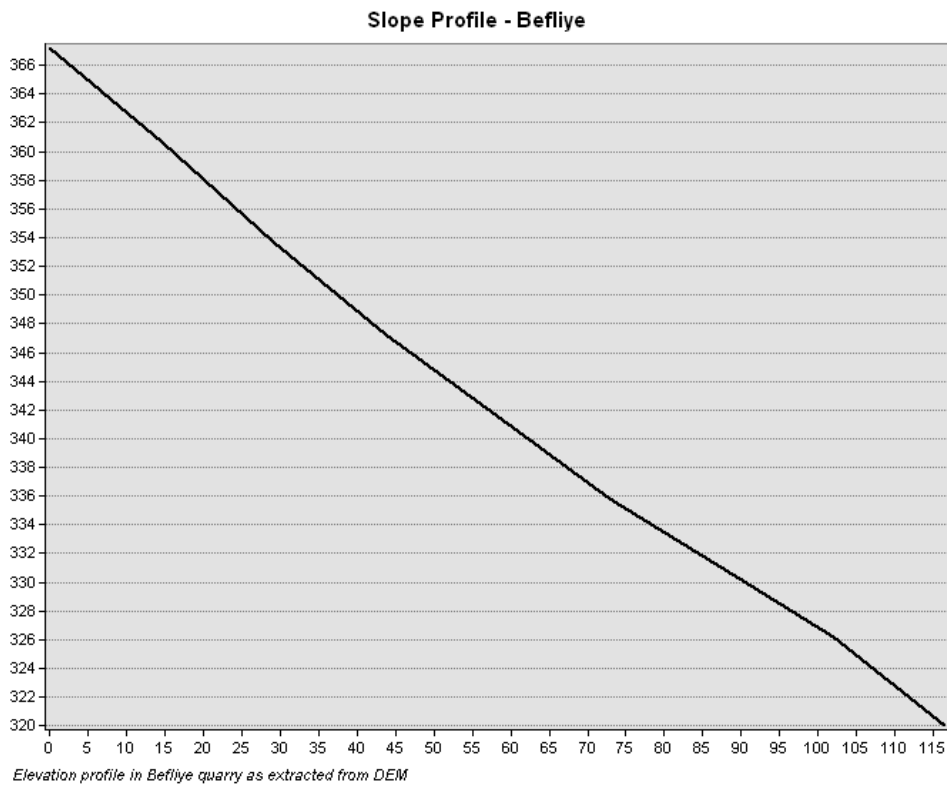


Figure 29: Slope profile as extracted from AcrMap for Befliye quarry

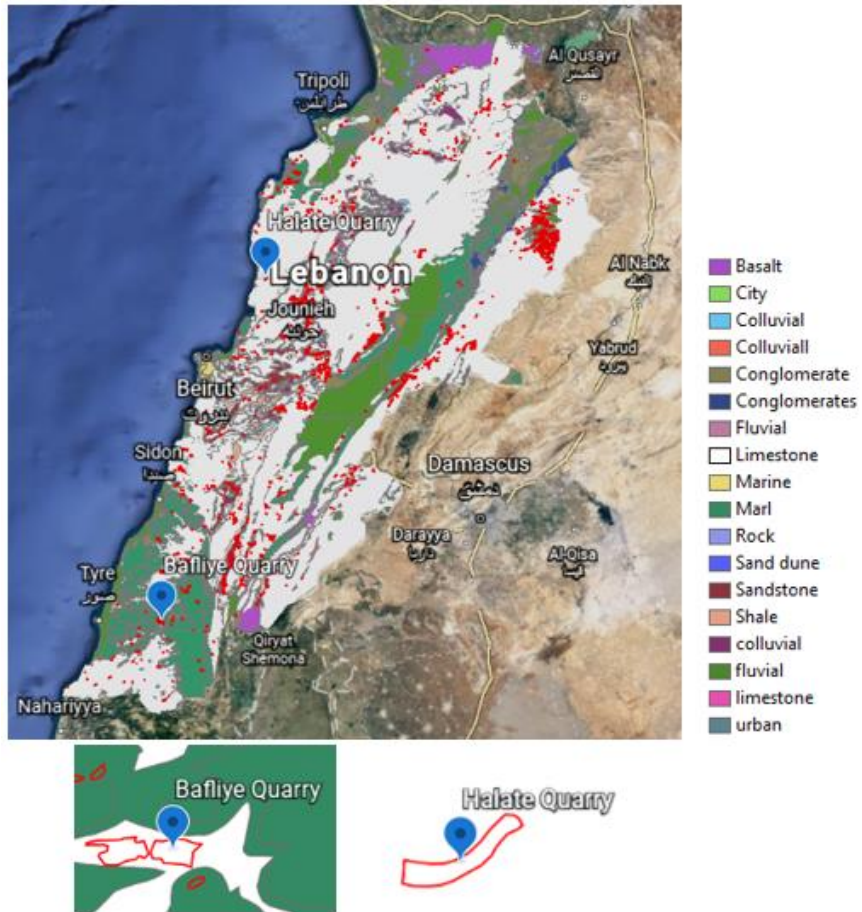


Figure 30: Google Earth image of Lebanon with geology and quarry layers overlay

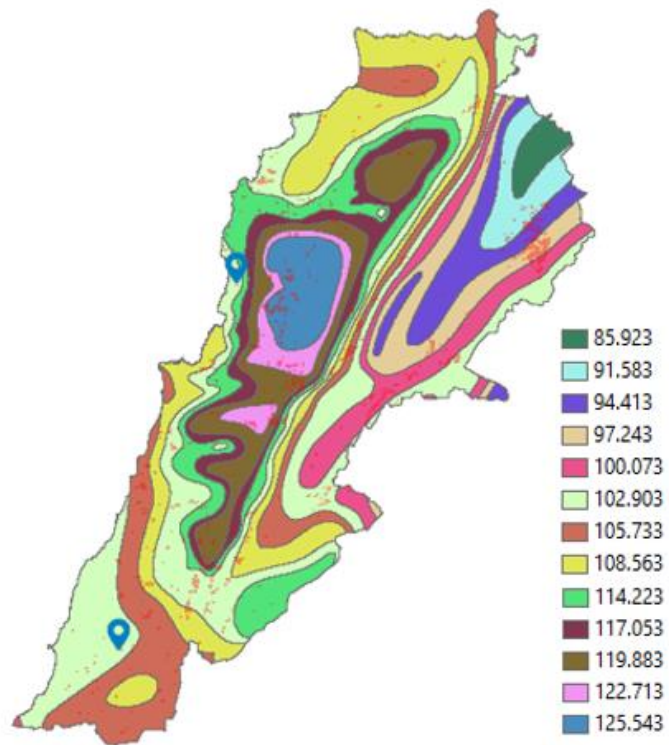


Figure 31: Plassard rainfall map highlighting quarries locations

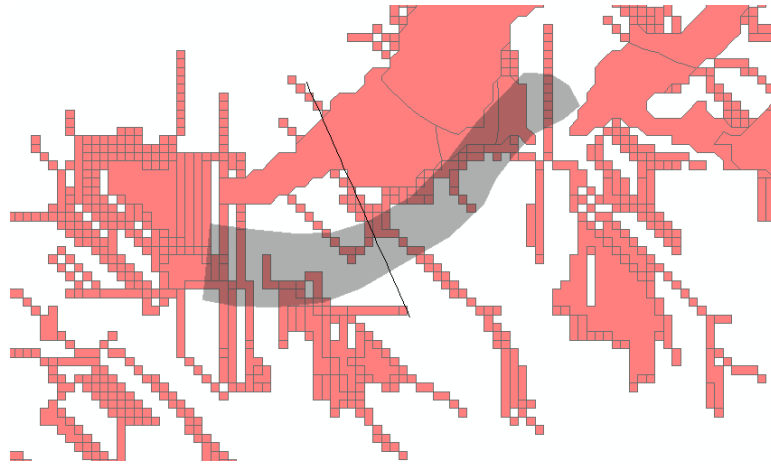


Figure 32: Pixelated rain hazards (pink) at the quarry site in Halat (grey polygon)

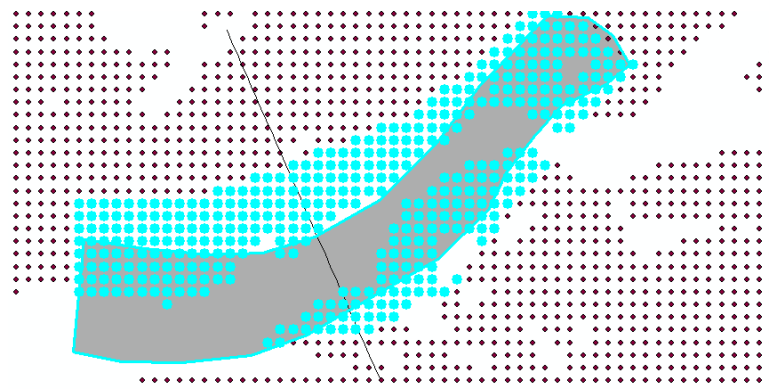


Figure 33: FS raster converted into point file for FS determination on site

The regional scale assessment successfully captures the top of the quarry as a hazard source from which the runout starts as shown in Fig. 34 (pink color is the runout source, and light green color is the runout area or extent). The quarry's actual area as observed in Google Earth is larger than the available polygon file of quarries' locations (Fig. 35) and hence the runout source predicted by the regional scale model is considered valid.

The runout area from the hazard source is determined to be  $71,550 \text{ m}^2 > 5000 \text{ m}^2$  implicating a high-risk runout with a reach angle of  $34^\circ$  as associated in Kaafarani et al. (2019). The corresponding volume is higher than  $1000 \text{ m}^3$ , yielding a weight higher than  $23 \text{ MN}$  for a unit weight of  $23 \text{ kN/m}^3$ . The rock weight obtained in site specific analysis for the most critical intersecting joints is  $12.66 \text{ MN}$  at most and yields a much smaller runout distance ( $7.76 \text{ m}$ ) and thus a higher reach angle ( $82.44^\circ$ ). The difference in reach angles in both analysis is  $58.76\%$ , with the site specific analysis predicting a low risk if failure occurs while the regional scale model predicts a high risk scenario. Site specific analysis takes into account the roughness factors of both the slope's face and lying ground, which will increase the friction between these surfaces and the

sliding wedge mass, causing energy losses and therefore stopping the sliding wedge at a closer distance, and hence increasing its angle of reach and reducing its risk level. Even though the slopes are similar in terms of geometry, geology and triggering factors, this does not imply that the runout analysis has to be the same, as the latter depend on specific site conditions (roughness of slope face, volume and weight of failing wedge, etc.).

The regional scale assessment does not take into consideration the presence, effects and interactions of discontinuities and is based on Mohr-Coulomb criteria solely, whereas the site specific assessment takes these factors fully into account, and more reliable models are used for the analysis of rock material. Nevertheless, the regional assessment when capturing the quarried slopes, provides a good approximation (in this case with a difference of 14.3% in rainfall events and 3.33% in seismic events) of the possible hazard levels.

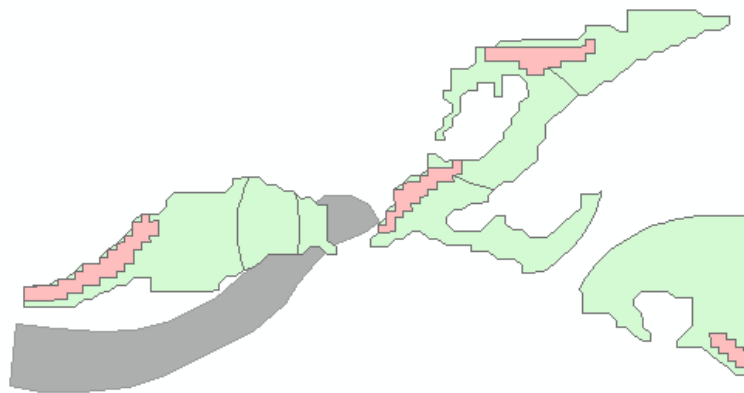


*Figure 34: Regional-scale runout analysis at Halat quarry in ArcMap*



*Figure 35: Variation between available polygon layer of quarries' area and actual quarry in Google Earth*

# Chapter Five

## Conclusion

Quarried slopes in Lebanon occupy large areas of the mountainous terrains and their spread is usually chaotic and unorganized. They alter the slope geometry, induce additional discontinuities and compromise the slope's safety, yet, quarried slopes have not been studied from a slope stability perspective in Lebanon. The recently generated regional scale maps for landslide hazards under rainfall and seismic events provided a direct assessment of slope stability across the country. However, their ability to predict hazards and risks at altered slopes was not yet validated.

A time and cost efficient methodology using drone imagery, especially under rainfall and seismic events is presented in this research to predict hazards and risks at quarried sites, and its results are compared with the regional scale assessment. In order to test the methodology at hand, a quarried slope in Bafliye, South Lebanon was selected, and the susceptibility of this slope to fail under possible rainfall and seismic events was assessed using limit equilibrium and finite element methods. The dominant failure mode in this quarry was found from the kinematic analysis to be wedge sliding. Both LEM and FEM analyses showed that the quarry is stable under dry conditions with a factor of safety of 1.41, and this was confirmed from observations made on site, with no failures detected visually. However, under rainfall events with intensity of 103 mm/day, the slope proved to be unstable in FEM with a factor of safety of 1.19 and stable in LEM with a factor of safety of 1.41. The critical slopes in the quarry also generated low factors of safety under seismic events with a peak ground acceleration of 0.25g. The corresponding factors of safety of 0.86 using LEM and 0.97 using FEM were obtained under seismic conditions. Numerical analysis predicted the lowest factor of safety under rainfall and seismic to occur on intersecting joints different than the one predicted in LEM, with the FEM method being more representative of the real-life scenario. As for runout assessment, it was found that the failing rock wedges can reach a distance of 10.22 meters away from the slope's face, and thus posing no significant risk on nearby areas.

The site-specific analysis was compared to the multi-modal regional scale landslide hazard assessment under rainfall and seismic events (Grant et al. (2016) and Kaafarani

et al. (2019)). The Bafliye quarry was not captured by the DEM due to the coarseness of the raster, and another quarry in Halate, Jbeil with similar slope, geology, PGA, and rain intensity was selected to compare the results of site specific analysis to the regional scale model results. The results came in good agreement for hazard assessment, with a 14.3% difference in case of rainfall events and 3.33% difference in case of seismic events. The safety factor under rainfall was found to be 1.02 from the regional maps which is lower and more conservative than 1.19 obtained from site specific assessment. The runout in regional scale was calculated based on the weights of sliding wedge (23 MN) and angles of reach were assigned accordingly ( $34^\circ$ ), yielding a high risk landslide. These values were different by 58.76% than the ones obtained from site specific analysis, where the maximum wedge weight was 12.66 MN and the angle of reach was calculated as  $82.44^\circ$ , and thus resulting in a low risk landslide. This difference is due to the multiple parameters involved in the runout distance calculation in the site specific analysis (friction, restitution, roughness, wedge weight, wedge velocity) compared to the regional runout determination which is based only on the failing wedge weight.

The proposed methodology results confirm the observations made on site in terms of possible modes of failure. The methodology proved to be time and cost effective since no geotechnical field investigation campaigns, surveying activities, nor extensive knowledge of rock mechanics are required. The regional scale model hazard predictions came in good agreement with site specific analysis when the slope is captured in the DEM, while risks associated with runout distances did not. Hazard and risk levels at the site under study can now be updated easily on the regional maps to better represent their actual degree, using more refined strength parameters. The results obtained from one quarried site however, are not definitive, and more quarried sites should be investigated to build a robust comparison and draw representative conclusions on the ability of the regional scale to predict failures in quarries. Finally, regional maps for hazard and risk level prediction at quarried sites under rainfall and seismic events can be developed for Lebanon. These maps can be further used to designate safe and suitable quarrying locations, update and develop public policies related to future urban planning and enforce measurements to reduce the risks of quarries on nearby urban settlements and infrastructure.

# **Chapter Six**

## **Limitations**

The aim was initially to map at least two quarries (one limestone and one sandstone) to be able to update the regional maps at all quarried sites and to generate a separate regional map for quarries hazard levels under rainfall and earthquake triggering events. However, due to the sensitivity of the topic, and the fact that many quarries are illegal and their owners have concerns about their site being photographed and exposed to the public, we faced restrictions and we were not allowed to access several sites. More than 30 municipalities and quarry owners were contacted to ask permission, but we were able to secure only one limestone quarry to which the proposed methodology was tailored, and was analyzed thoroughly herein.

# References

- Abdallah, C. (2011). Assessment of erosion, mass movements, and flood risks in Lebanon. In H. Kouyoumjian & M. Ham (Ed.). *Review and Perspectives of Environmental Studies in Lebanon* (pp 225-246). National Council for Scientific Research (CNRS), Beirut, Lebanon.
- Abdullah, R., Yusufianshah, D., Alel, M., Jusoh, S., Hezmi, M., & Yunus, M & Ali, A.N. & Ali., A. (2018). Slope stability analysis of quarry face at Karang Sambung district, central Java, Indonesia. *International Journal of Civil Engineering and Technology* 9, 857-864.
- Alejano, L., Castro-Filgueira, C., Pérez-Rey, I., & Arzúa, J. (2017). Stability Analysis of an Over-tilted Slope in a Granite Quarry: The Role of Joint Spacing. *Procedia Engineering* 191, 402-409. doi:10.1016/j.proeng.2017.05.197.
- Azzoni, A., & De Freitas, M. (1995). Experimentally Gained Parameters, Decisive for Rock Fall Analysis. *Rock Mechanics and Rock Engineering* 28 (2), 111-124.
- Bhandari, S. & Rathore, S. (2002). Comparative study of blasting techniques in dimensional stone quarrying. *International Society of Explosives Engineers*, pp 219 – 228.
- Cardu, M., Patrucco, M. & Lovera, Enrico & Michelotti, Enrica. (2005). Quarrying by explosive and diamond wire in hard dimension stones. *Proceedings of the 3<sup>rd</sup> world conference on explosives and blasting*, Brighton, 13 September 2005. European Federation of Explosives Engineers, Rochester, UK, pp 409 – 414.
- Chrysanthos, S., Zacharias, A., Evangelia, A., & Georgia, P. (2017). Mining in a Landslide—Is It Possible? *Geotechnical Investigation and Analysis*. doi:10.1061/9780784480458.026.
- Colomina, I. & Molina, P. (2014). Unmanned aerial systems for photogrammetry and remote sensing: a review. *ISPRS J Photogramm Remote Sens* 92:79–97.
- Costa, M., Coggan, J.S., & Eyre, J.M. (1999). Numerical modeling of slope behavior of Delabole slate quarry (Cornwall, UK). *International Journal of Surface Mining, Reclamation and Environment* 13, 11-18.
- Cotecchia, F., Lollino, P., Santaloia, F., Vitone, C. & Mitaritonna, G. (2010). Deterministic Landslide Hazard Assessment at Regional Scale. *Geotechnical Special Publication*. doi:10.1061/41095(365)319.
- Crosta, G. (1997). Evaluating rock mass geometry from photogrammetric images. *Rock Mech Rock Eng* 30(1):35–38. doi:10.1007/BF01020112.
- Darwish, T., Khater, C., Jomaa, I., Stehouwer, R., Shaban, A., & Hamze, M. (2010). Environmental impact of quarries on natural resources in Lebanon. *Land Degrad. Develop.* 22, 345–358.
- Dawson, E., Roth, W., & Drescher, A. (1999). Slope stability analysis by strength reduction. *Geotechnique* 49(6): 835 – 840.



- Dubertret L (1945) Cartes géologiques à l'échelle de 1/50 000 (Hamidieh, Halba, Batroun, Tripoli, Sir El Dannieh, Jbail, Qartaba, Baalbeck, Beirut, Zahle, Rayak, Saida, Jezzine, Rachaya). République Libanaise, Ministère des Travaux publics, Beyrouth, Liban.
- Fawaz, A., Abdullah, S., Farah, E., & Hagechehade, F. (2017). Analysis and Remedies for Landslides Including Vegetation: A Case Study in Lebanon. *American Journal of Civil Engineering* 5(6), 320-330. doi:10.11648/j.ajce.20170506.12.
- Fawaz, A., Farah, E., & Hagechehade, F. (2014). Slope Stability Analysis Using Numerical Modelling. *American Journal of Civil Engineering* 2 (3), 60-67. doi:10.11648/j.ajce.20140203.11.
- Froude, M., & Petley, D. (2018). Global fatal landslide occurrence from 2004 to 2016. *Nat. Hazards Earth Syst. Sci.* 18, 2161–2181. doi: 10.5194/nhess-18-2161-2018.
- García-Sellés, D., Falivene, O., Arbués, P., Gratacos, O., Tavani, S. & Muñoz, J.A. (2011). Supervised identification and reconstruction of near-planar geological surfaces from terrestrial laser scanning. *Computers & Geosciences* 37, 1584-1594.
- Gigli, G. & Casagli, N. (2011). Semi-automatic extraction of rock mass structural data from high resolution LIDAR point clouds. *International Journal of Rock Mechanics and Mining Sciences* 48, 187-198.
- Goodman, R.E. (1980). *Introduction to Rock Mechanics* (Chapter 8), Toronto: John Wiley, pp 254-287.
- Grant, A., Wartman, J., & Abou-Jaoude, G. (2016). Multimodal method for co-seismic landslide hazard assessment. *Eng. Geol.* 212, 146-160.
- Hack, R., Price, D. & Rengers, N. (2003). A new approach to rock slope stability: a probability classification SSPC. *Bulletin of engineering geology and the environment*, 62(2), 167-184. doi:10.1007/s10064-002-0155-4.
- Hoek, E. & Bray, J. (1981). *Rock Slope Engineering*. Revised 3rd Edition, The Institution of Mining and Metallurgy, London, pp 341-351.
- Hudson, J. & Harrison, J. (1997). *Engineering Rock Mechanics – An introduction to the Principles*, Pergamon. ISBN 978-0-08-043864-1.
- Huijjer, C. & Harajli, M. & Sadek, S. (2011). Upgrading the seismic hazard of Lebanon in light of the recent discovery of the offshore thrust fault system. *Lebanese Science Journal* 12, 67-77.
- Ismail, S., Hagechehade, F., & Al Wardany, R. (2014). Slope stability analysis under seismic loading. *Proceedings of the Second European Conference on earthquake engineering and seismology*, August 25-29 2014, Istanbul, Turkey.
- ISRM (1978). Suggested methods for the quantitative description of discontinuities in rock mass. *Int J Rock Mech Min Sci Geomech Abstr* 15:319–368.

- Kaafarani, R., Abou Jaoude, G., Wartman, J., Tawk, M. (2019). Landslide susceptibility mapping based on triggering factors using a multi-modal approach. Proceedings of International Conference of Engineering, 3-5 April, 2019. Beirut, Lebanon.
- Karaman, K., Ercikdi, B., & Kesimal, A. (2013). The assessment of slope stability and rock excavatability in a limestone quarry. *Earth Sciences Research Journal*, 17(2), 169-181.
- Kellerer-Pirklbauer, V. (2002). The influence of land use on the stability of slopes with examples from the European Alps. *Mitt. naturwiss. Ver. Steiermark* 132, 43–62.
- Kemeny, J., Turner, K. & Norton, B. (2006). LIDAR for rock mass characterization: hardware, software, accuracy and best-practices. In: Proceedings of the workshop on laser and photogrammetric methods for rock face characterization, Golden, CO, pp 49–61.
- Khawlie, M., 1999. Hot spots and sensitive areas: contribution of remote sensing to Geoenvironmental mapping in Lebanon. In: Borrousky P. (Ed.). *Geoenvironmental mapping*, Balkema publishing, 79-87.
- Khoshelham, K., Altundag, D., Ngan-Tillard, D. & Menenti, M. (2011). Influence of range measurement noise on roughness characterization of rock surfaces using terrestrial laser scanning. *International Journal of Rock Mechanics and Mining Sciences* 48, 1215-1223.
- Krahn, J. (2003). The 2001 R.M. Hardy Lecture: The limits of limit equilibrium analyses. *Canadian Geotechnical Journal*. 40. 643-660. doi:10.1139/t03-024.
- Lato, M. & Vöge, M. (2012). Automated mapping of rock discontinuities 756 in 3D LIDAR and photogrammetry models. *International Journal of Rock Mechanics and Mining Sciences* 54, 150-158.
- Lato, M., Diederichs, M. & Hutchinson, D. (2010). Bias correction for view-limited Lidar scanning of rock outcrops for structural characterization. *Rock mechanics and rock engineering* 43, 615-628.
- Lato, M., Diederichs, M., Hutchinson, D. & Harrap, R. (2009). Optimization of LiDAR scanning and processing for automated structural evaluation of discontinuities in rock masses. *International Journal of Rock Mechanics and Mining Sciences* 46, 194-199.
- Li, X.Z., Xu, Q. (2016). Application of the SSPC method in the stability assessment of highway rock slopes in the Yunnan province of China. *Bulletin of engineering geology and the environment* 75, 551–562. doi:10.1007/s10064-015-0792-z.
- Liu, S., Shao, L. & Li, H. (2015). Slope stability analysis using the limit equilibrium method and two finite element methods. *Computers and Geotechnics*. 63. doi:10.1016/j.compgeo.2014.10.008.
- Mah, J., Samson, C. & Mckinnon, S. (2011). 3D laser imaging for joint orientation analysis. *Int J Rock Mech Min Sci* 48:932–941. doi:10.1016/j.ijrmms.2011.04.010.

- Marinos, V., Proutzopoulos, G., Asteriou, P., Papathanassiou, G., Kaklis, T., Pantazis, G., Lambrou, E., Grendas, N. & Karantanellis E, Pavlides S (2017). Beyond the boundaries of feasible engineering geological solutions: stability considerations of the spectacular Red Beach cliffs on Santorini Island, Greece. *Environ Earth Sci.* doi.org/10.1007/S1266 5-017-6823-2.
- Matsui, T. & San, K. (1992). Finite Element Slope Stability Analysis by Shear Strength Reduction Technique. *Soils and Foundations* 32(1): 59-70.
- MOE, UNDP, & ECODIT (2011). State and Trends of the Lebanese Environment Report.
- Norrish, N. & Wyllie, D. (1996). Rock slope stability analysis. In: Landslides: investigation and mitigation, Special Report 247. Transportation Research Board, National Research Council, Washington, pp 391–425.
- Olariu, M., Ferguson, J., Aiken, C. & Xu, X. (2008). Outcrop fracture characterization using terrestrial laser scanners: Deep-water Jack fork sandstone at Big Rock Quarry, Arkansas. *Geosphere* 4, 247-259.
- Park, H. (2005). A new approach for persistence in probabilistic rock slope stability analysis. *Geosciences Journal.* 9, 287-293. doi:10.1007/BF02910589.
- Park, J., Lee, S., Lee, D., Kim, Y. & Lee, J. (2019). A regional-scale landslide early warning methodology applying statistical and physically based approaches in sequence. *Engineering Geology* 260. doi:105193. 10.1016/j.enggeo.2019.105193.
- Pellicani, R., Argentiero, I., & Spilotro, G. (2017). GIS-based predictive models for regional-scale landslide susceptibility assessment and risk mapping along road corridors. *Geomatics, Natural Hazards and Risk* 8. doi:10.1080/19475705.2017.1292411.
- Piras, M., Taddia, G., Forno, M., Gattiglio, M., Aicardi, I., Dabove, P., Lo Russo, S. & Lingua, A. (2017). Detailed geological mapping in mountain areas using an unmanned aerial vehicle: application to the Rodoretto Valley, NW Italian Alps. *Geomatics, Natural Hazards and Risk*, 8:1, 137-149. doi:10.1080/19475705.2016.1225228.
- Plassard, J. (1971). Rainfall map of Lebanon at scale 1/200,000. Ministry of Public Works. General Directorate of Civil Aviation.
- Pollock, W., Grant, A., Wartman, J., & Abou-Jaoude, G. (2019). Multimodal method for landslide risk analysis. *MethodsX*, 6, 827–836. doi:10.1016/j.mex.2019.04.012.
- Prasetyo, S., Gutierrez, M., & Barton, N. (2017). Nonlinear shear behavior of rock joints using a linearized implementation of the Barton-Bandis model. *Journal of Rock Mechanics and Geotechnical Engineering*, 9. doi:10.1016/j.jrmge.2017.01.006.
- Priest SD. (1993). *Discontinuity analysis for rock engineering*, Springer. eISBN 978-94-011-1498-1.

- Riquelme, A., Abellán, A., Tomás, R. & Jaboyedoff, M. (2014). A new approach for semi-automatic rock mass joints recognition from 3D point clouds. *Computers & Geosciences*. doi:10.1016/j.cageo.2014.03.014.
- Riquelme, A., Tomás, R., Cano, M., & Abellán, A. (2016). Using Open-Source Software for Extracting Geomechanical Parameters of a Rock Mass From 3D Point Clouds: Discontinuity Set Extractor and SMR Tool. In Ulusay et al. (Eds). *ISRM International Symposium – EUROCK 2016, Ürgüp, Turkey, 29-31 2016*. London: International Society for Rock Mechanics and Rock Engineering 176, 1091-1096.
- Robotham, M., Wang, H., & Walton, G. (1995). Assessment of risk from rock fall from active and abandoned quarry slopes. *Institution of mining and Metallurgy, Section A 104, A25-A33*.
- Rossi, G., Tanteri, L., Tofani, V., Vannocci, P., Moretti, S. & Casagli, N. (2018). Multitemporal UAV surveys for landslide mapping and characterization. *Landslides 15*, 1045–1052. doi:10.1007/s10346-018-0978-0.
- Rossini, M., Di Mauro, B., Garzonio, R., Baccolo, G., Cavallini, G., Mattavelli, M., De Amicis, M. & Colombo, R. (2018). Rapid melting dynamics of an alpine glacier with repeated UAV photogrammetry. *Geomorphology 304*:159–172. doi:/10.1016/j. geomorphology.2017.12.039.
- Saade, A., Abou-Jaoude, G., Wartman, J., & Grant, A. (2016). Earthquake-Induced Landslide Hazard Mapping: A Case Study in Lebanon. In *Geo-Chicago 2016* (pp. 177-186).
- Sajinkumar, K., Sankar, G., Rani, V., & Sundarajan, P. (2014). Effect of quarrying on the slope stability in Banasuramala: an offshoot valley of Western Ghats, Kerala, India. *Environ Earth Sci 72*, 2333-2344. doi : 10.1007/s12665-014-3143-7.
- Salvini, R., Mastroiocco, G., Esposito, G., Di Bartolo, S., Coggan J & Vanneschi C (2018). Use of a remotely piloted aircraft system for hazard assessment in a rocky mining area (Lucca, Italy). *Nat Hazards Earth Syst Sci 18*, 287–302. doi.org/10.5194/nhess-18-287-2018.
- Slob, S., Knapen, B., Hack, R., Turner, K. & Kemeny, J. (2005). Method for Automated Discontinuity Analysis of Rock Slopes with Three-Dimensional Laser Scanning. *Transportation Research Record: Journal of the Transportation Research Board 1913*, 187-194.
- Steiakakis, C., Zach, A., Apostolou, E., & Papavgeri, G. (2017). Mining in a Landslide—Is It Possible? *Geotechnical Investigation and Analysis. Geotechnical Frontiers 2017: Walls and Slopes, GSP 278*.
- Sturzenegger, M. & Stead, D. (2009). Quantifying discontinuity orientation and persistence on high mountain rock slopes and large landslides using terrestrial remote sensing techniques. *Nat. Hazards Earth Syst. Sci. 9*, 267-287.
- Sturzenegger, M., Stead, D. & Elmo, D. (2011). Terrestrial remote sensing based estimation of mean trace length, trace intensity and block size/shape. *Eng Geol 119*:96–111. doi:10.1016/j.enggeo.2011.02.005.

- Tomastik, J., Mokros, M., Salon, S., Chudy, F. & Tunak, D. (2017). Accuracy of photogrammetric UAV-based point clouds under conditions of partially-open forest canopy. *Forests*. doi:10.3390/ f8050 151.
- Uysal, M., Toprak, A. & Polatm, N. (2015). DEM generation with UAV Photogrammetry and accuracy analysis in Sahitler hill. *Measurement* 73:539-543. doi.org/10.1016/j.measurement.2015.06.010.
- Vedeil E, Faour G, & Velut S. (2007). Atlas du Liban territoires et societies. Coll. Etudes contemporaines. Ed. Institut Francais du Proche-Orient / CNRS Liban. Beyrouth, Liban ISBN 978-2-35159- 053-9. 210 pp.
- Wang, H., Zhang, B., Bai, X., & Shi, L. (2018). A novel environmental restoration method for an abandoned limestone quarry with a deep open pit and steep palisades: a case study. *R. Soc. open sci.* 5: 180365.doi:10.1098/rsos.180365.
- Wang, S., Zhang, Z., Wang, C., Zhu, C., Ren, Y. (2019). Multistep rocky slope stability analysis based on unmanned aerial vehicle photogrammetry. *Environ Earth Sci* 78, 260. doi:10.1007/s12665-019-8145-z.
- Westoby, J., Brasington, J., Glasser, F., Hambrey, J. & Reynolds, J. (2012). Structure-from-Motion photogrammetry: a low-cost, effective tool for geoscience applications. *Geomorphology* 179:300–314.
- World Bank, METAP. (2003). Republic of Lebanon Cost Assessment of Environmental Degradation.
- Xi, W. & Li, D., (2017). Steep slope DEM Model construction based on the unmanned aerial vehicle (UAV) images. *Sains Malays* 46:2119–2124. doi:10.17576 /jms-2017-4611-12.
- Xu, C., Xu, X., Dai, F., & Saraf, A.K. (2012). Comparison of different models for susceptibility mapping of earthquake triggered landslides related with the 2008 Wenchuan earthquake in China. *Computers & Geosciences* 46, 317-329.
- Yu, H., Salgado, R., Sloan, W., & Kim, J. (1998). Limit Analysis versus Limit Equilibrium for Slope Stability. *Journal of Geotechnical and Geoenvironmental Engineering - J GEOTECH GEOENVIRON ENG.* 124. doi:10.1061/ (ASCE) 1090-0241(1998)124:1(1).
- Ziade, R., Abdallah, C., & Baghdadi, N. (2014). The effect of forest fire on mass movement in Lebanese mountainous areas. *International Journal of Wildland Fire*. doi:10.1071/WF13077.

# Appendices

## Appendix A: Validation of 3D Model Measurements

Prior to the quarry's site visit, the Phantom 4 Pro V2.0 was used to map a building (Engineering Laboratories and Research Center, ELRC) at the Lebanese American University, Byblos campus where geometrical features can be easily measured, both in real life using a regular tape or total station, and in Pix4D Mapper. A medium resolution 3D model was generated for the building to accelerate image processing and the point cloud and the 3D texturized mesh generation. Four distinct features (Fig. 36 and Fig. 37) were selected from the 3D model to be measured using a regular tape on site, and then in the 3D model in Pix4D using the linear distance option.



Figure 36: Long bench, short bench and fountain at ELRC



Figure 37: soil contour at lower ELRC entrance

Three features are at the main entrance to the ELRC, which represent a long bench, a short bench and the fountain. The plane 2D dimensions of these features were measured and reported in Table 8. The maximum difference was obtained to be 1.2% which is considered very low, and hence proving that measurements taken from Pix4D Mapper, even when using medium resolution models, have high accuracy when compared with real life measurements.

*Table 8: Width and Length of long and short bench and fountain as measured on field and in Pix4D Mapper*

	<b>Width (m)</b>	<b>Length (m)</b>
Long Bench		
<b>Pix 4D Mapper</b>	0.60	8.34
<b>Field</b>	0.60	8.36
<b>Difference (%)</b>	0	0.24
Short Bench		
<b>Pix 4D Mapper</b>	0.81	2.36
<b>Field</b>	0.82	2.36
<b>Difference (%)</b>	1.2	0
Fountain		
<b>Pix 4D Mapper</b>	2.36	10.74
<b>Field</b>	2.38	10.78
<b>Difference (%)</b>	0.84	0.37

The fourth feature was checked for perimeter determination accuracy using Pix4D Mapper, for which has a specific tool, rather than just adding length and width. The perimeter measured in the field is 17.22 meters while the one measured in Pix4D Mapper is 17.20 meters and hence yielding a difference of 0.12% and once again proving the high accuracy of the measurements done in Pix4D Mapper.

Then, the slope measurement accuracy was determined using a total station and a signal receiver along the way to ELRC, which is an inclined path. The ground slope between the location where the total station is placed and the signal receiver was determined, using both the instrument and receiver heights, and the measured angle between the vertical axis passing through the total station upward (azimuth) and the inclination of the device. The height of the total station is 1.41 meters, the height of the receiver is 1.45 meters, and the recorded angle with the azimuth using the total station is  $97^{\circ}10'35''$ . The inclined distance between both instruments was measured as 22.814 meters, and hence using it along with the supplementary angle ( $82^{\circ}49'25''$ ), the horizontal distance between the total station and its receiver was calculated as

22.636 meters., and the vertical distance between the total station and the receiver was determined as 2.85 meters. As a result, the difference in elevation between the two locations at ground level can be calculated using the below equation:

$$\begin{aligned} elev_{receiver} - elev_{total\ station} &= HI - VD - HR = 1.41 - 2.85 - 1.45 \\ &= -2.89\ m \end{aligned}$$

And thus,  $elev_{total\ station} - elev_{receiver} = 2.89\ m$

The result came out negative since the total station was placed on the higher level.

The slope of the ground can be then calculated as the ratio of the vertical ground difference and the horizontal distance between the two ground points.

$$slope = \frac{2.89}{22.636} \times 100 = 12.767\%$$

The slope obtained in Pix4D Mapper is 12.867% and thus yielding a difference of 0.78%, which is relatively on the lower end.

Therefore, the measurements made on Pix4D Mapper can be considered of high accuracy given the negligible differences found between real-life and 3D model measurements.



## Appendix B: Limit Equilibrium Results using RocScience SWEDGE

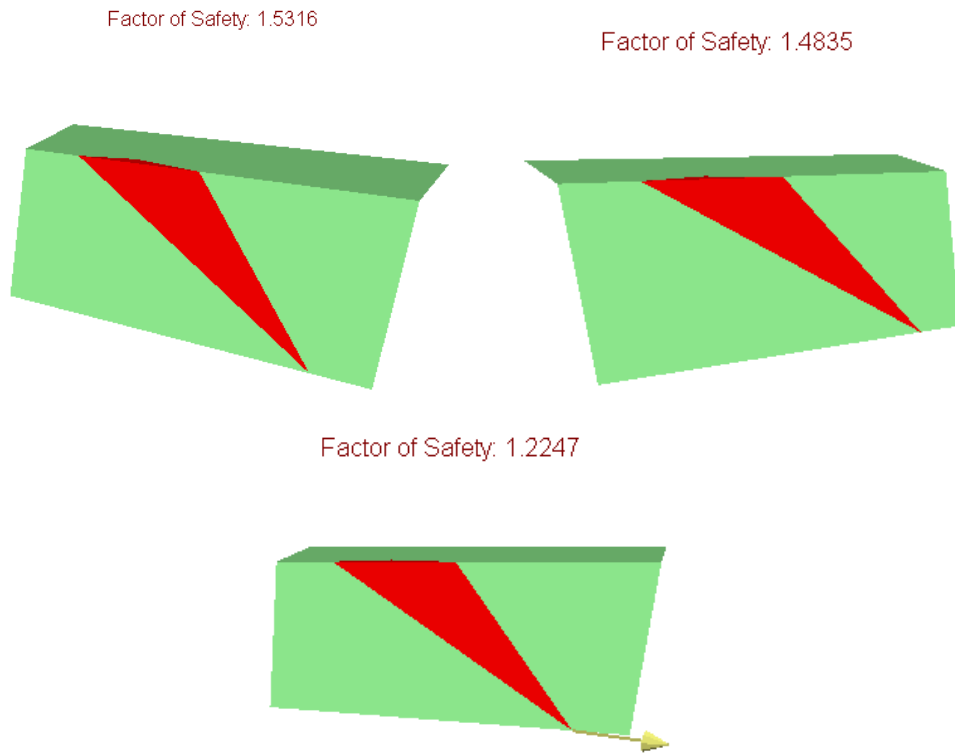


Figure 38: JS 5 and JS 6 (a) Dry conditions (b) 17% saturation (c) 0.25g ground acceleration

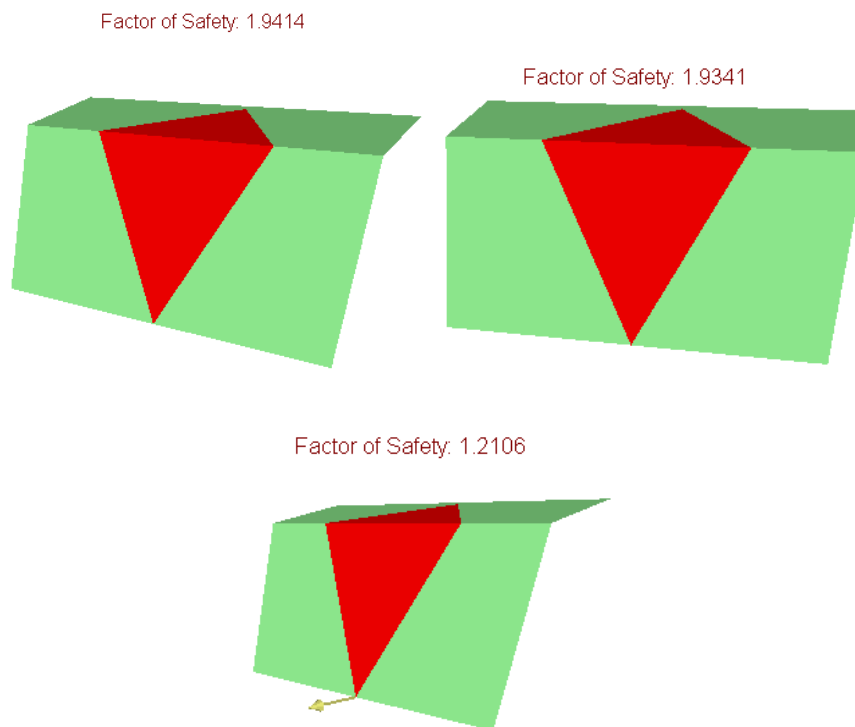


Figure 39: JS 2 and JS 3 (a) Dry conditions (b) 17% saturation (c) 0.25g ground acceleration

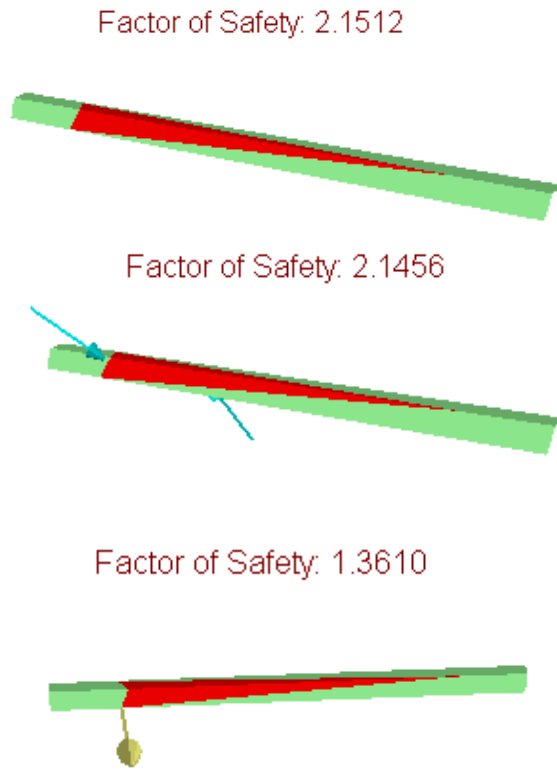


Figure 40: JS 2 and JS 4 (a) Dry conditions (b) 17% saturation (c) 0.25g ground acceleration

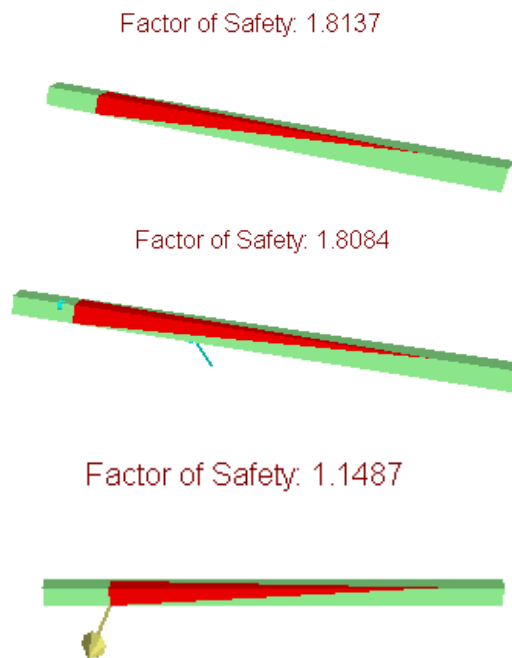
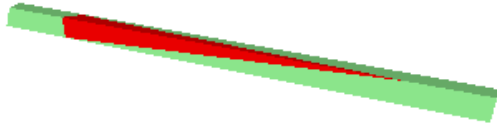
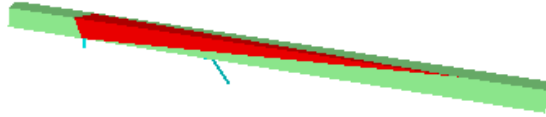


Figure 41: JS 8 and JS 4 (a) Dry conditions (b) 17% saturation (c) 0.25g ground acceleration

Factor of Safety: 1.8052



Factor of Safety: 1.7998

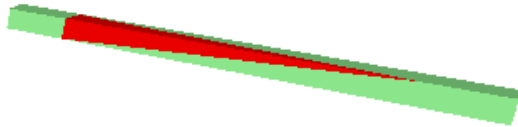


Factor of Safety: 1.1487

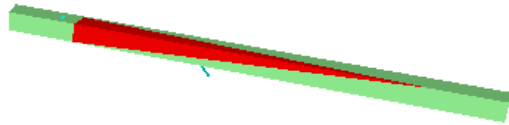


Figure 42: JS 3 and JS 4 (a) Dry conditions (b) 17% saturation (c) 0.25g ground acceleration

Factor of Safety: 1.8152



Factor of Safety: 1.8097



Factor of Safety: 1.1703

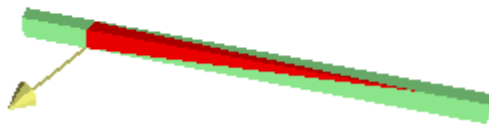


Figure 43: JS 9 and JS 4 (a) Dry conditions (b) 17% saturation (c) 0.25g ground acceleration

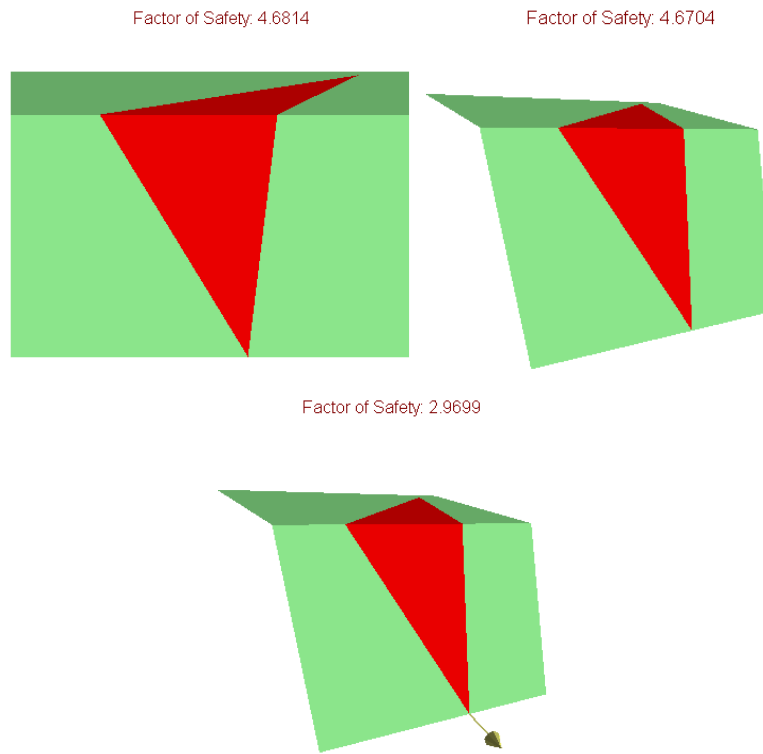


Figure 44: JS 9 and JS 3 (a) Dry conditions (b) 17% saturation (c) 0.25g ground acceleration

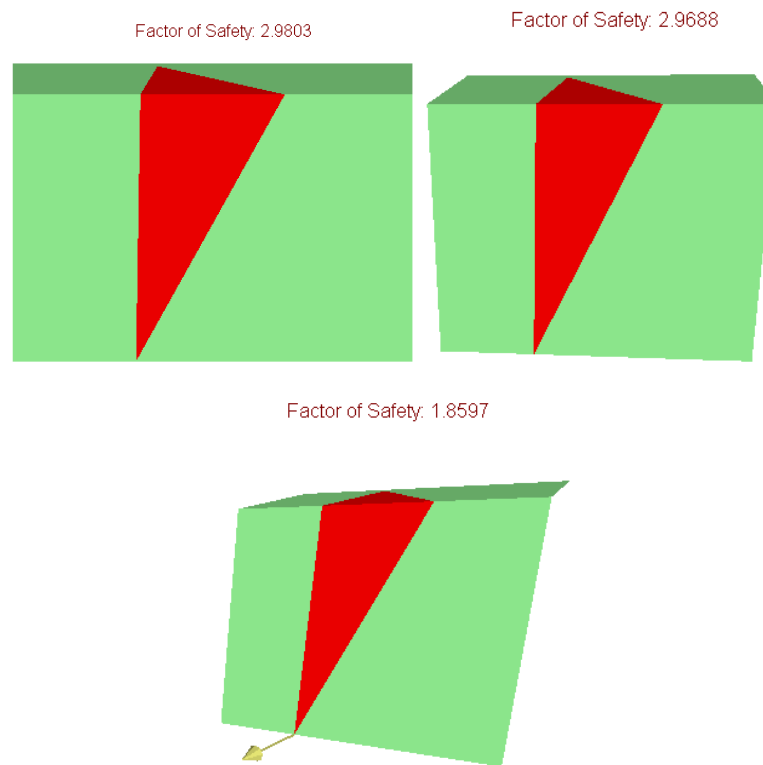


Figure 45: JS 2 and JS 8 (a) Dry conditions (b) 17% saturation (c) 0.25g ground acceleration

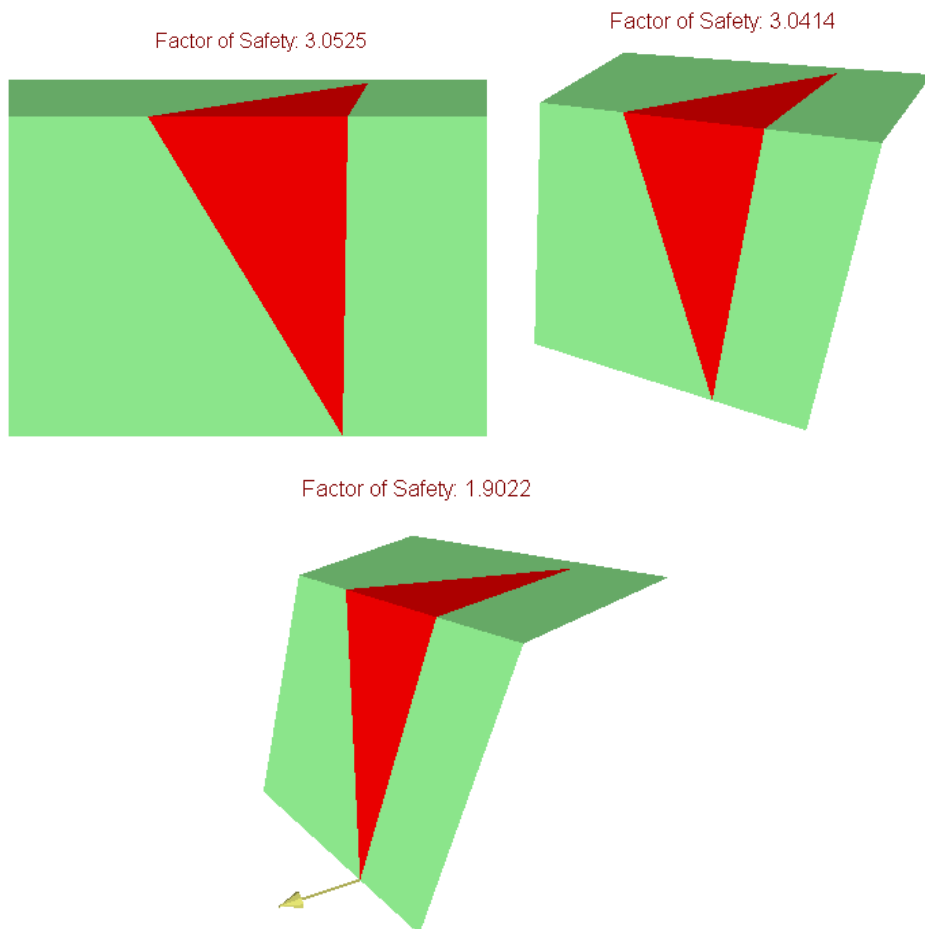


Figure 46: JS 3 and JS 8 (a) Dry conditions (b) 17% saturation (c) 0.25g ground acceleration

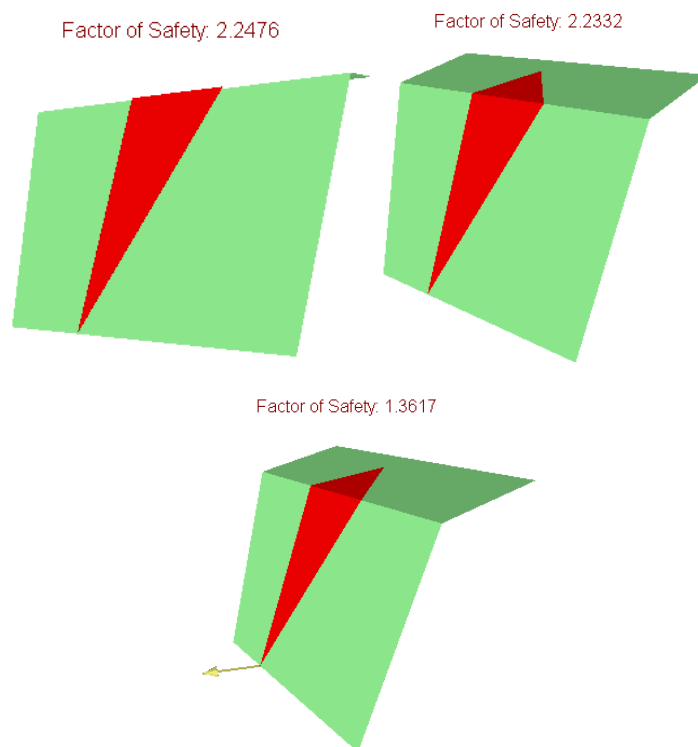


Figure 47: JS 2 and JS 9 (a) Dry conditions (b) 17% saturation (c) 0.25g ground acceleration

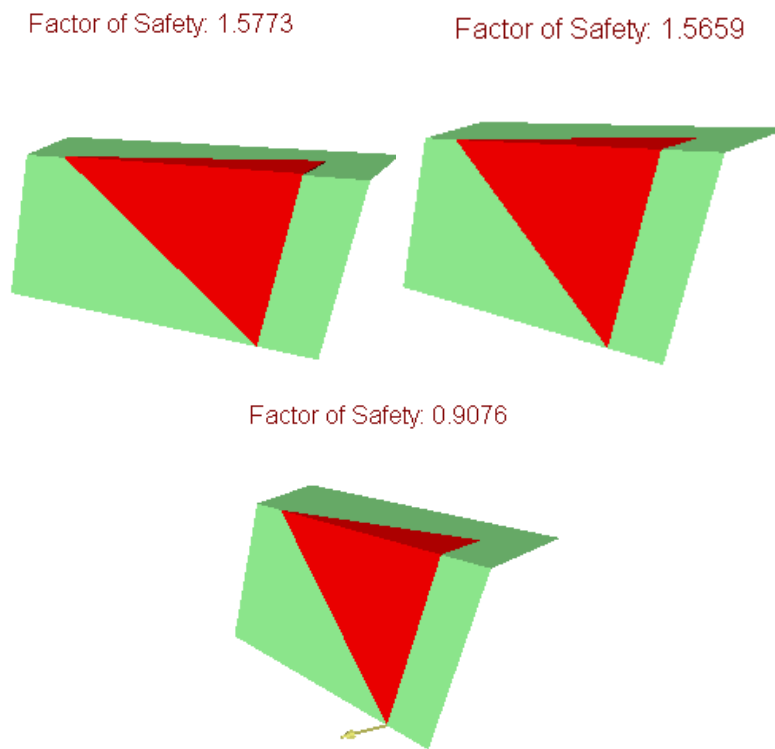


Figure 48: JS 8 and JS 5 (a) Dry conditions (b) 17% saturation (c) 0.25g ground acceleration

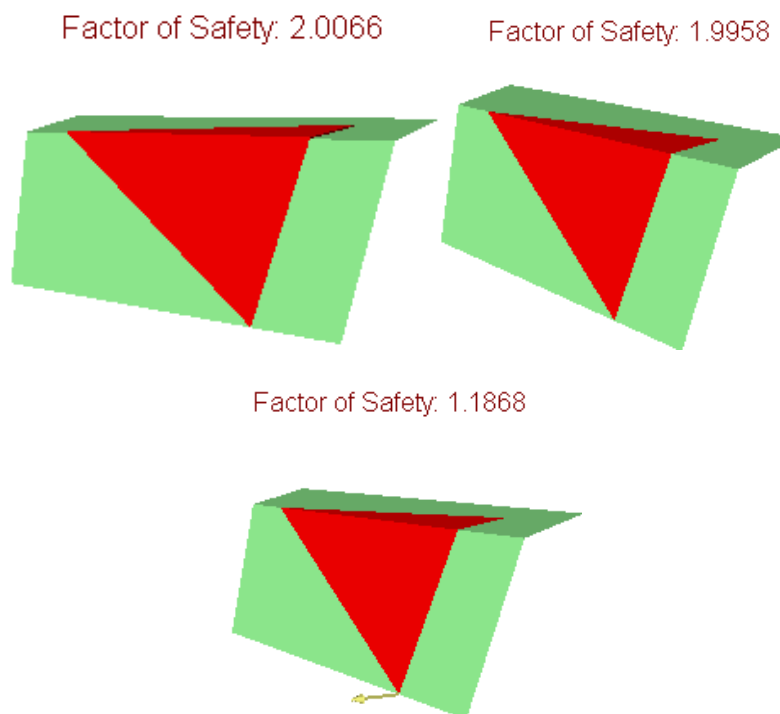


Figure 49: JS 9 and JS 5 (a) Dry conditions (b) 17% saturation (c) 0.25g ground acceleration

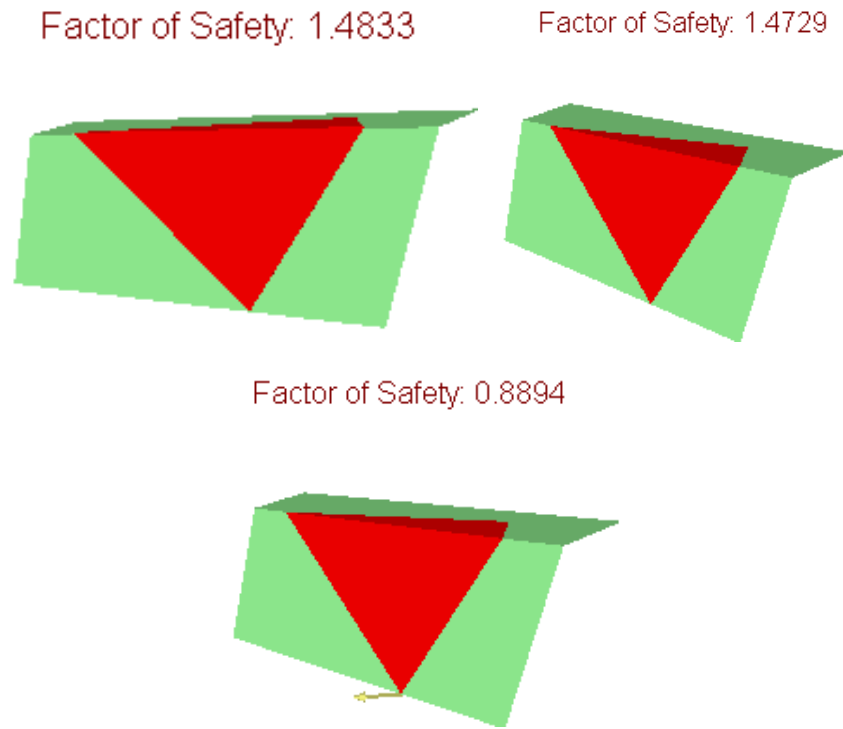


Figure 50: JS 2 and JS 5 (a) Dry conditions (b) 17% saturation (c) 0.25g ground acceleration

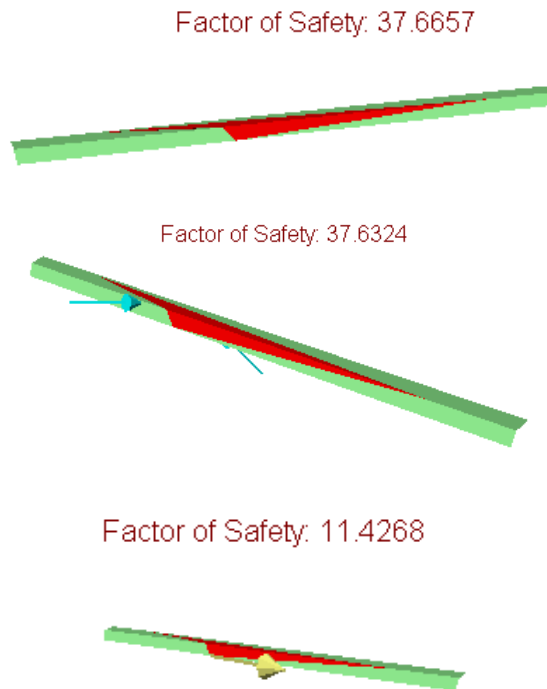
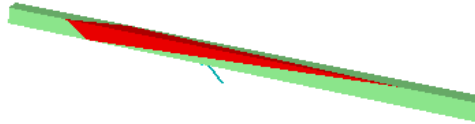


Figure 51: JS 6 and JS 4 (a) Dry conditions (b) 17% saturation (c) 0.25g ground acceleration

Factor of Safety: 1.7876



Factor of Safety: 1.7817



Factor of Safety: 1.4474

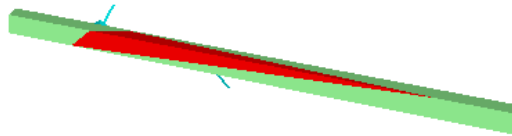


Figure 52: JS 5 and JS 4 (a) Dry conditions (b) 17% saturation (c) 0.25g ground acceleration

Factor of Safety: 1.8318



Factor of Safety: 1.8256



Factor of Safety: 1.5215



Figure 53: JS 10 and JS 4 (a) Dry conditions (b) 17% saturation (c) 0.25g ground acceleration



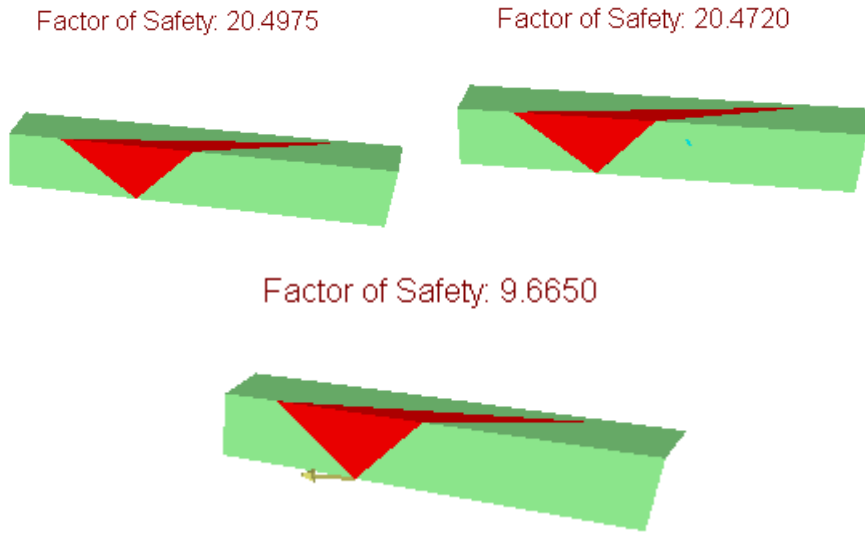


Figure 54: JS 10 and JS 5 (a) Dry conditions (b) 17% saturation (c) 0.25g ground acceleration



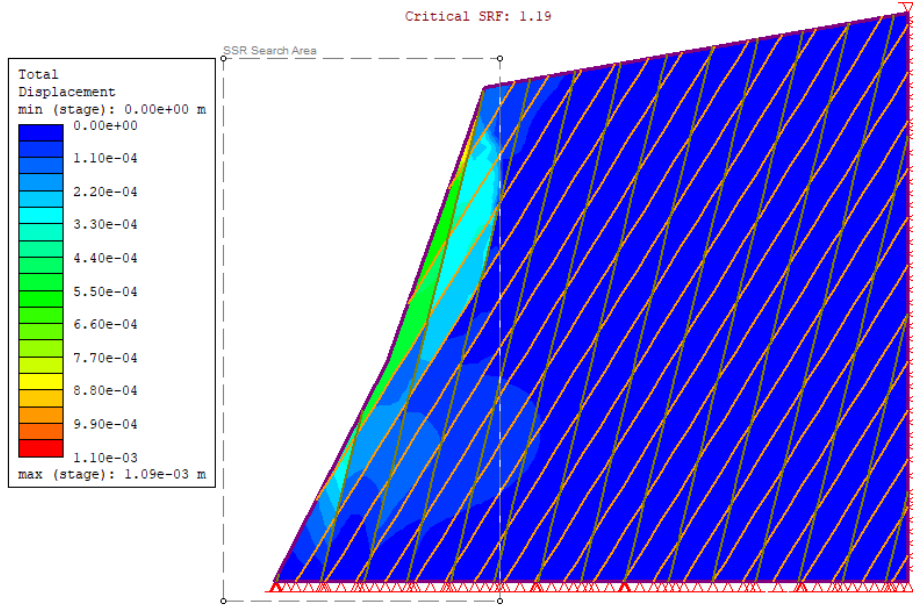


Figure 57: JS 5 and JS 6 (0.25g ground acceleration)

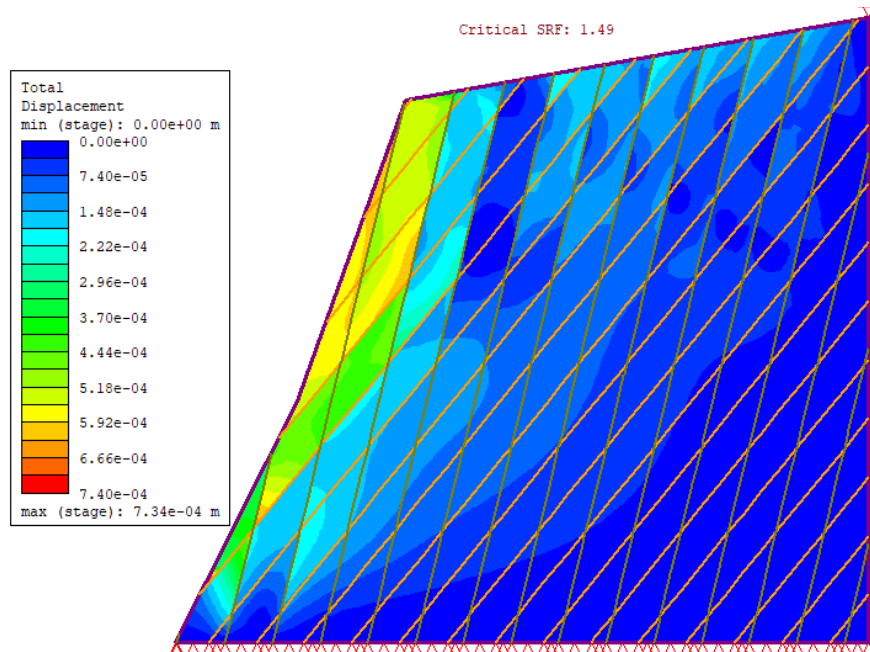


Figure 58: JS 3 and JS 6 (dry conditions)

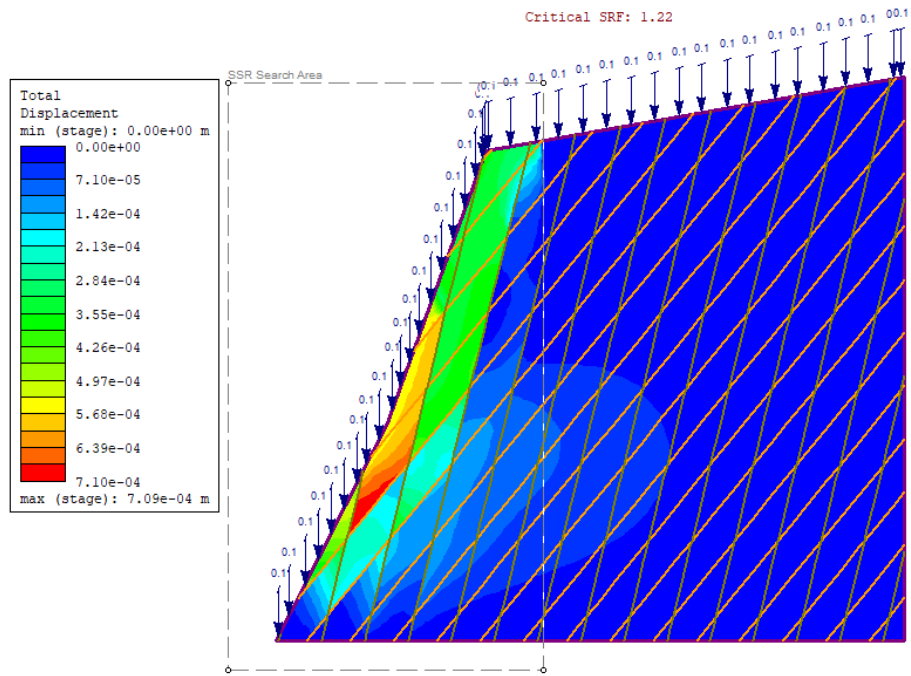


Figure 59: JS 3 and JS 6 (rainfall intensity 0.103 mm/day)

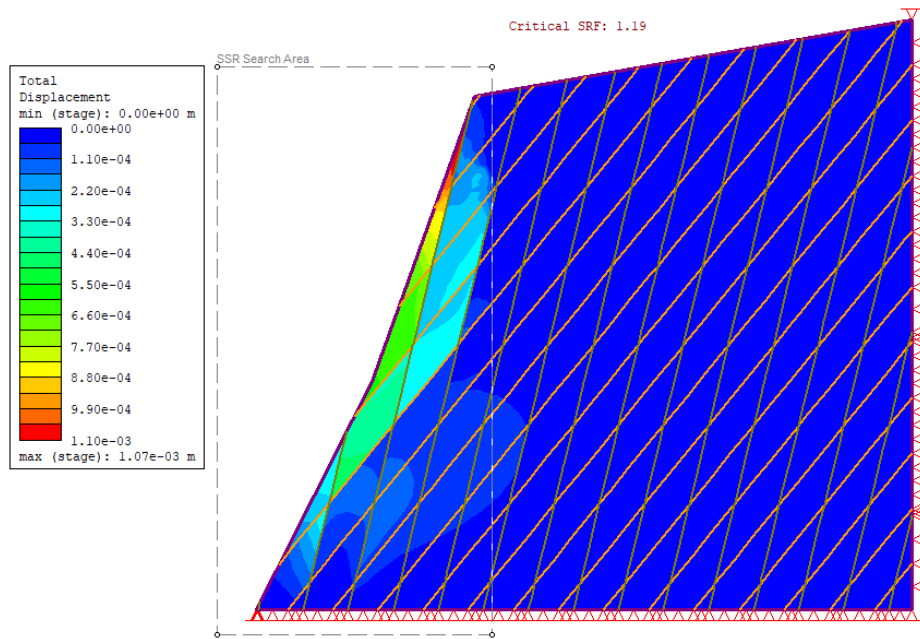


Figure 60: JS 3 and JS 6 (0.25g ground acceleration)

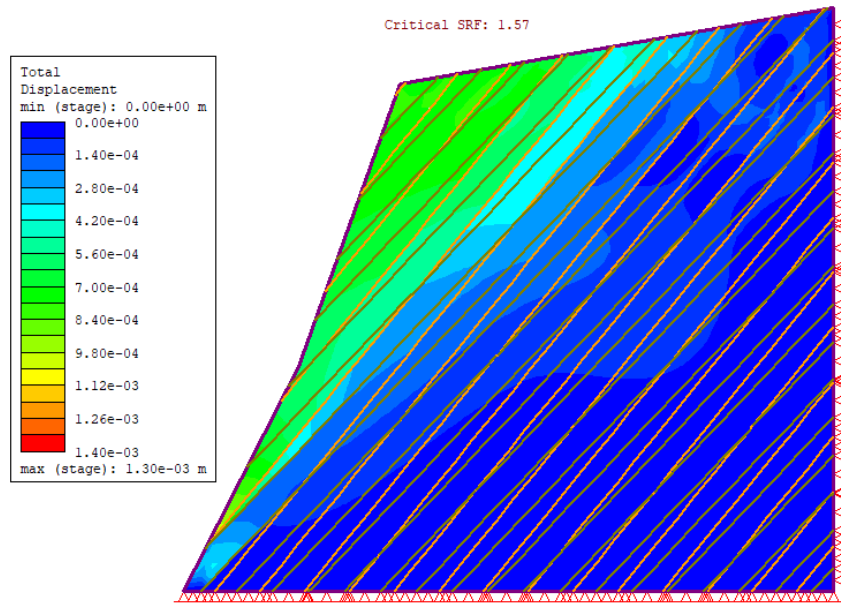


Figure 61: JS 2 and JS 3 (dry conditions)

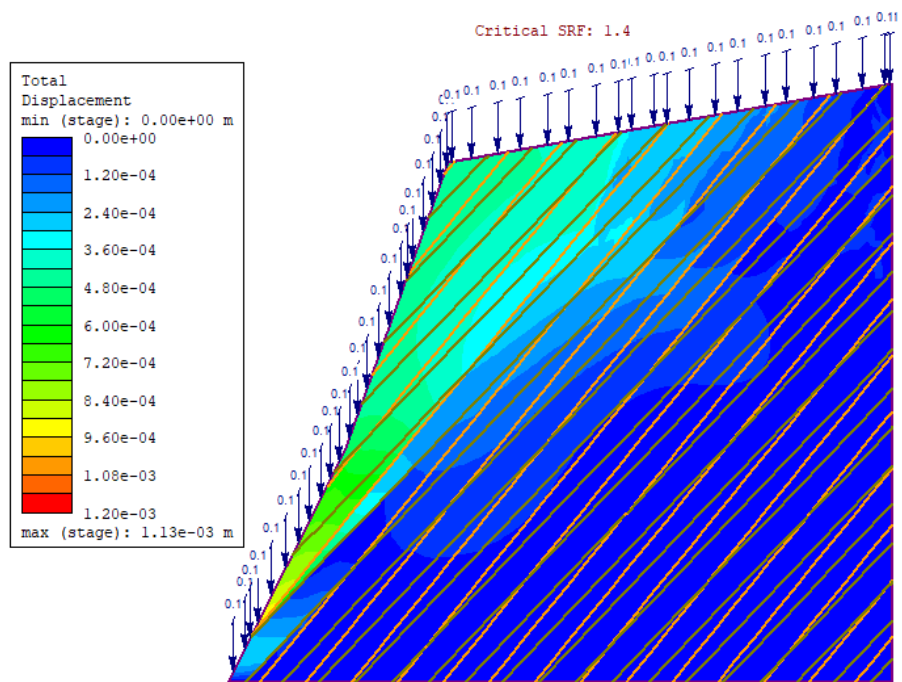


Figure 62: JS 2 and JS 3 (rainfall intensity 0.103 mm/day)

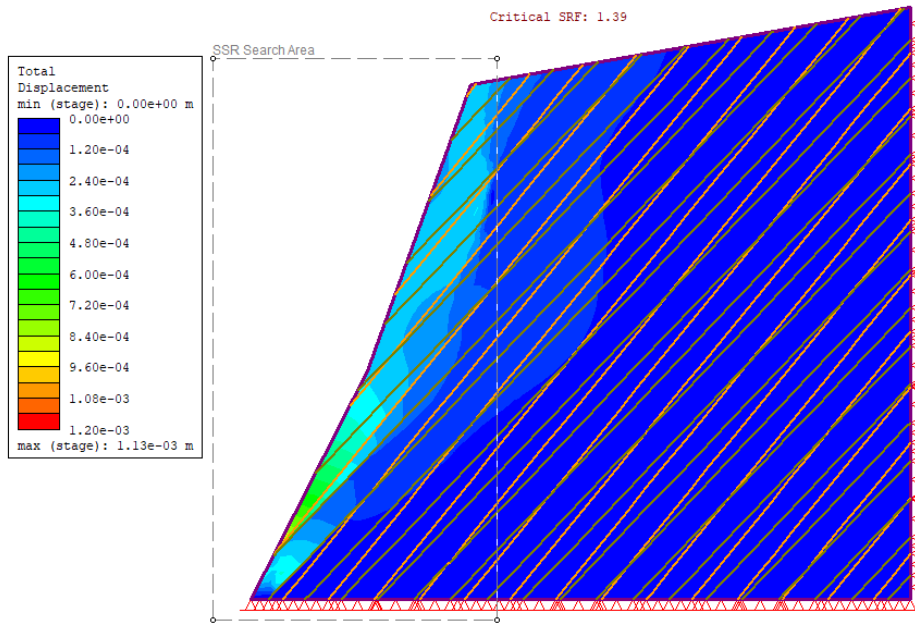


Figure 63: JS 2 and JS 3 (0.25g ground acceleration)

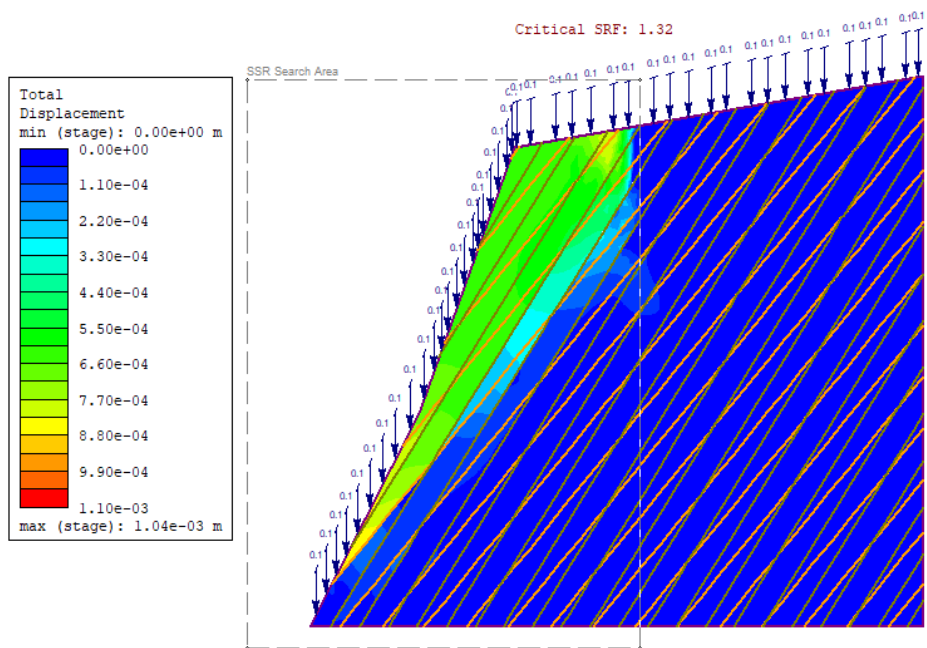


Figure 64: JS 5 and JS 3 (rainfall intensity 0.103 mm/day)

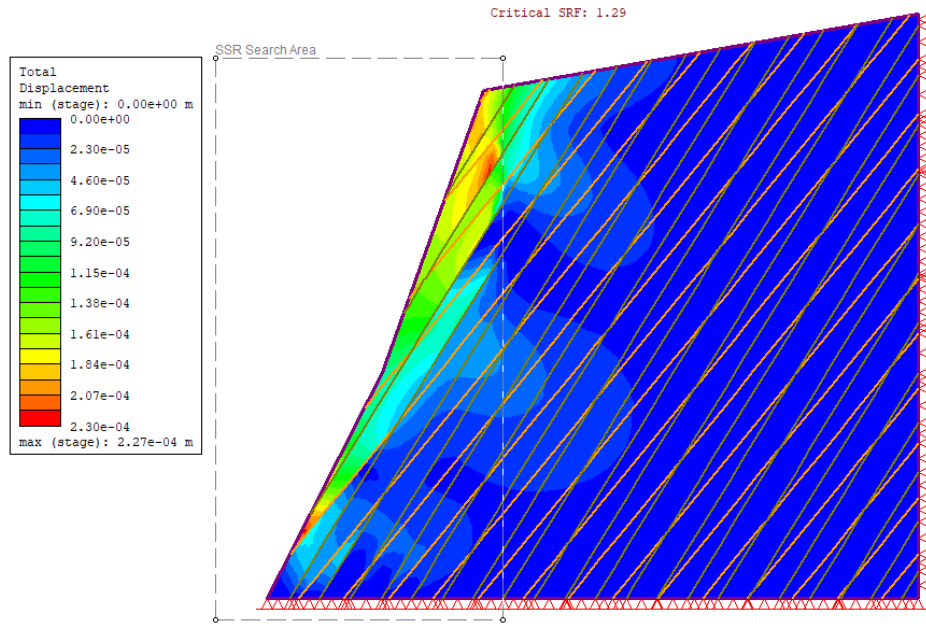


Figure 65: JS 5 and JS 3 (0.25g ground acceleration)

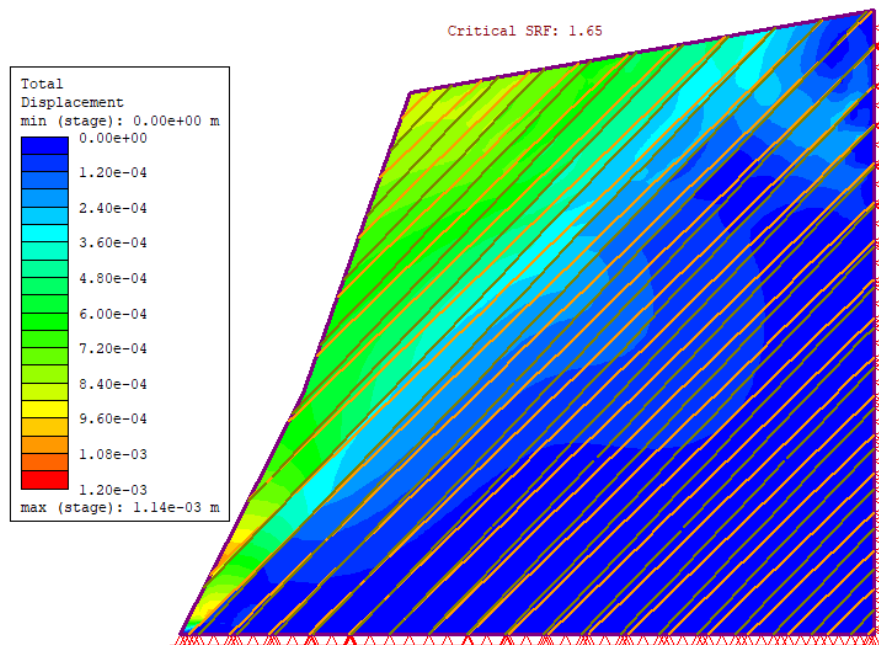


Figure 66: JS 2 and JS 4 (dry conditions)



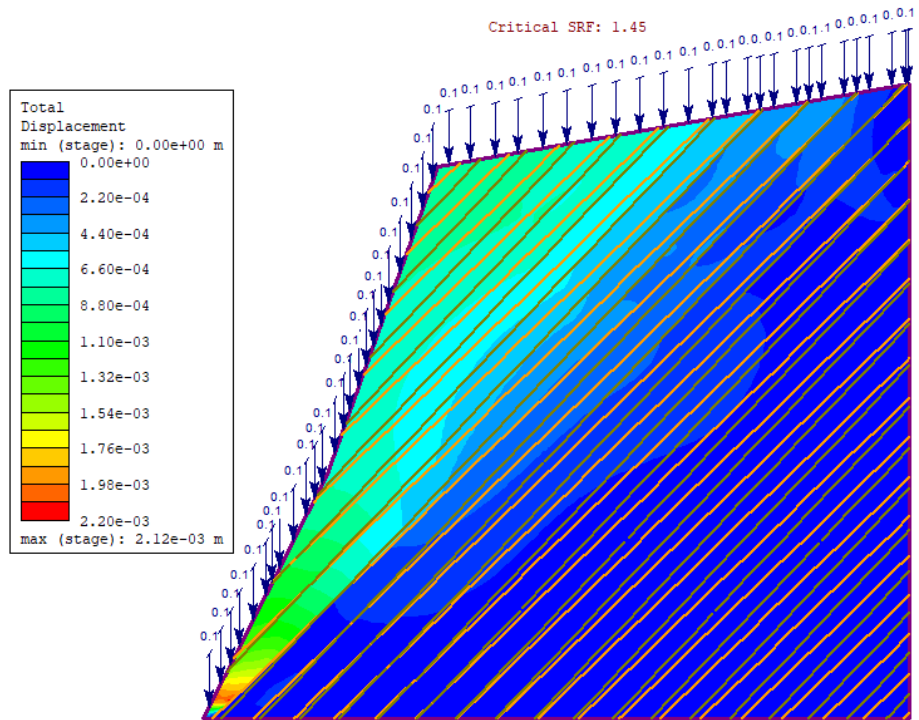


Figure 67: JS 2 and JS 4 (rainfall intensity 0.103 mm/day)

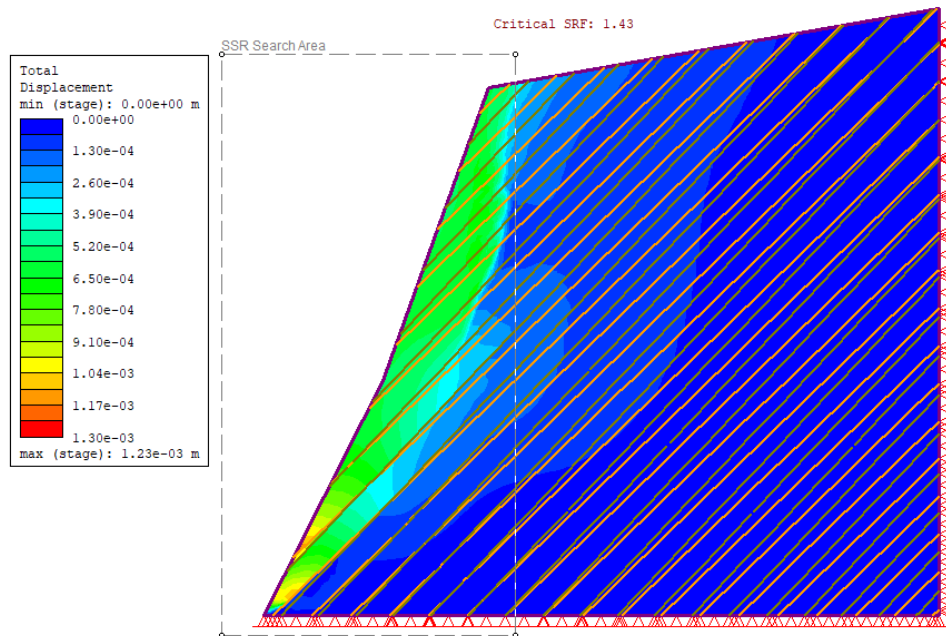


Figure 68: JS 2 and JS 4 (0.25g ground acceleration)



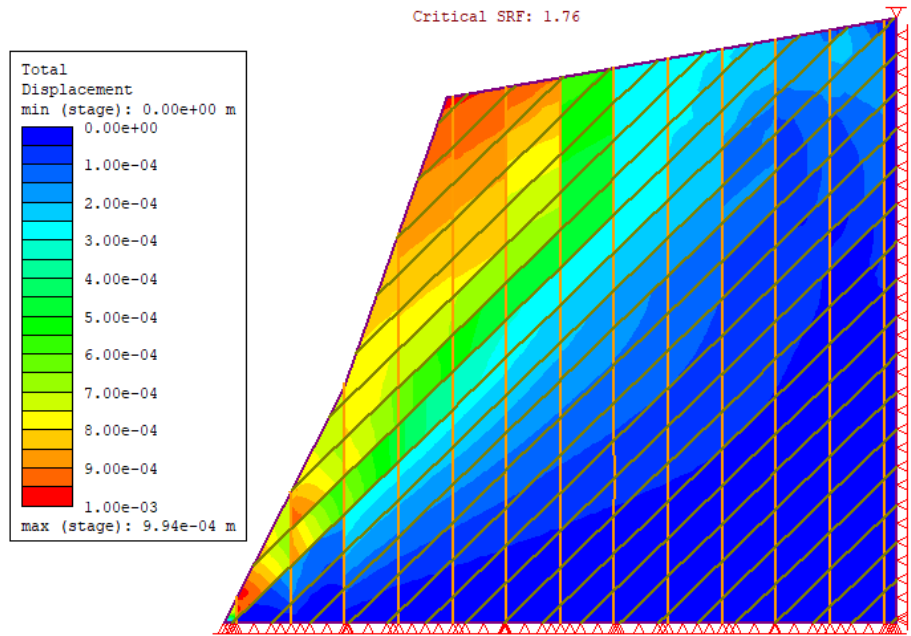


Figure 69: JS 8 and JS 4 (dry conditions)

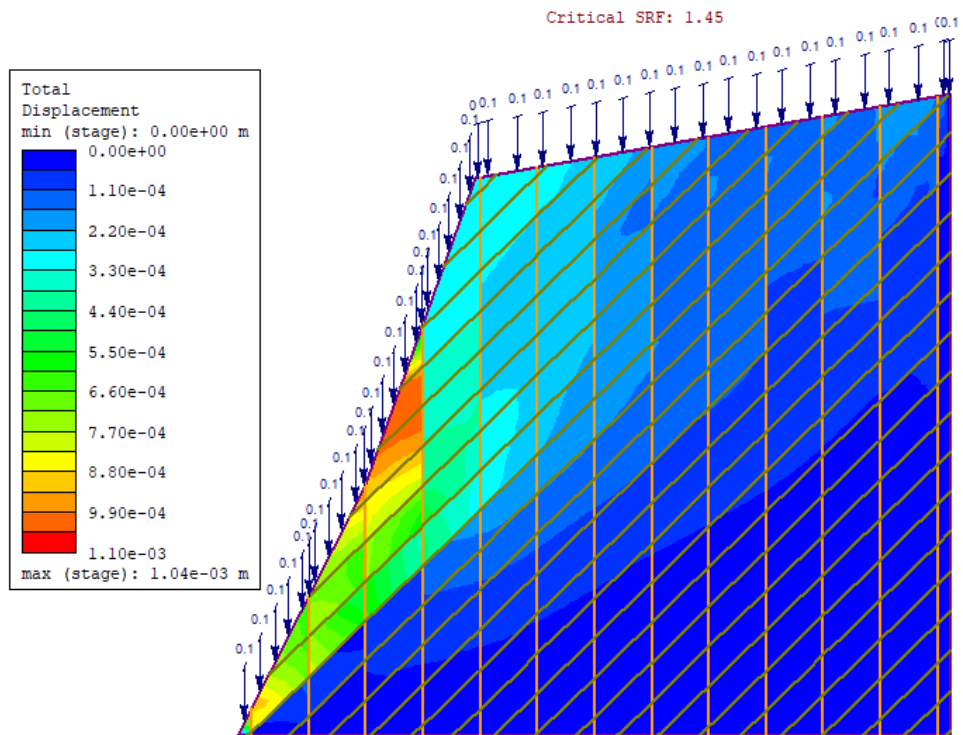


Figure 70: JS 8 and JS 4 (rainfall intensity 0.103 mm/day)

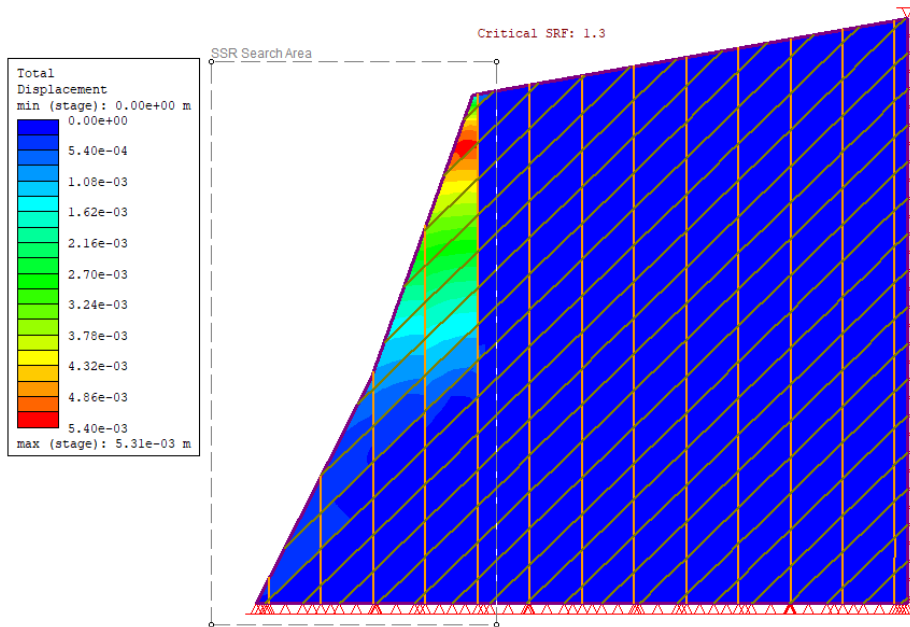


Figure 71: JS 8 and JS 4 (0.25g ground acceleration)

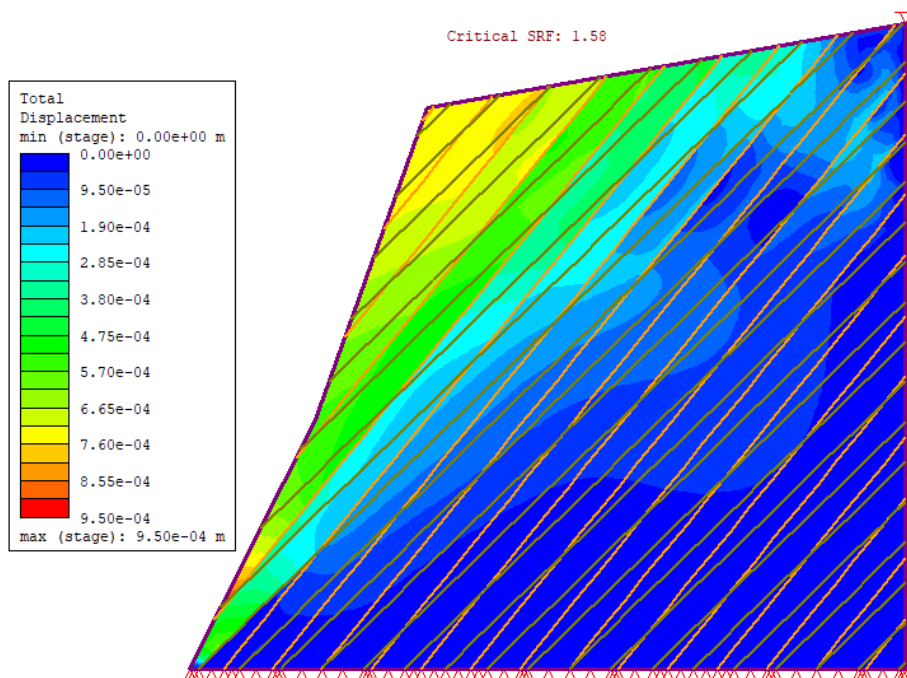


Figure 72: JS 3 and JS 4 (dry conditions)

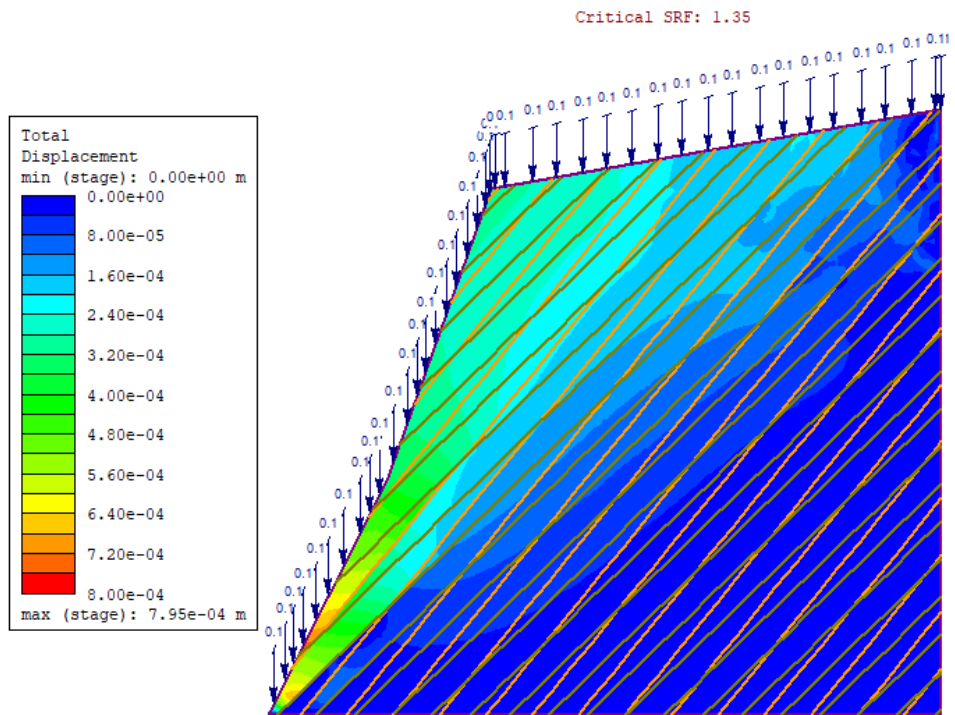


Figure 73: JS 3 and JS 4 (rainfall intensity 0.103 mm/day)

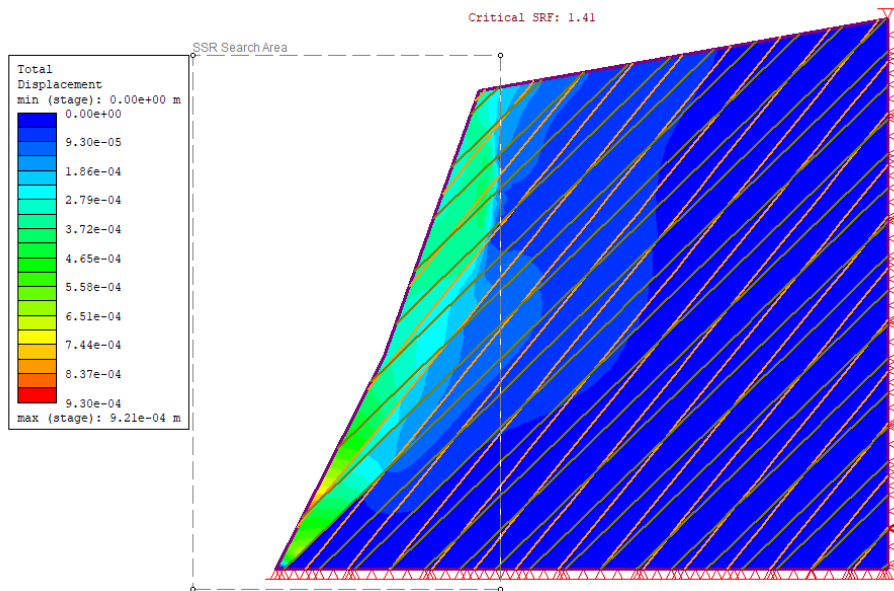


Figure 74: JS 3 and JS 4 (0.25g ground acceleration)

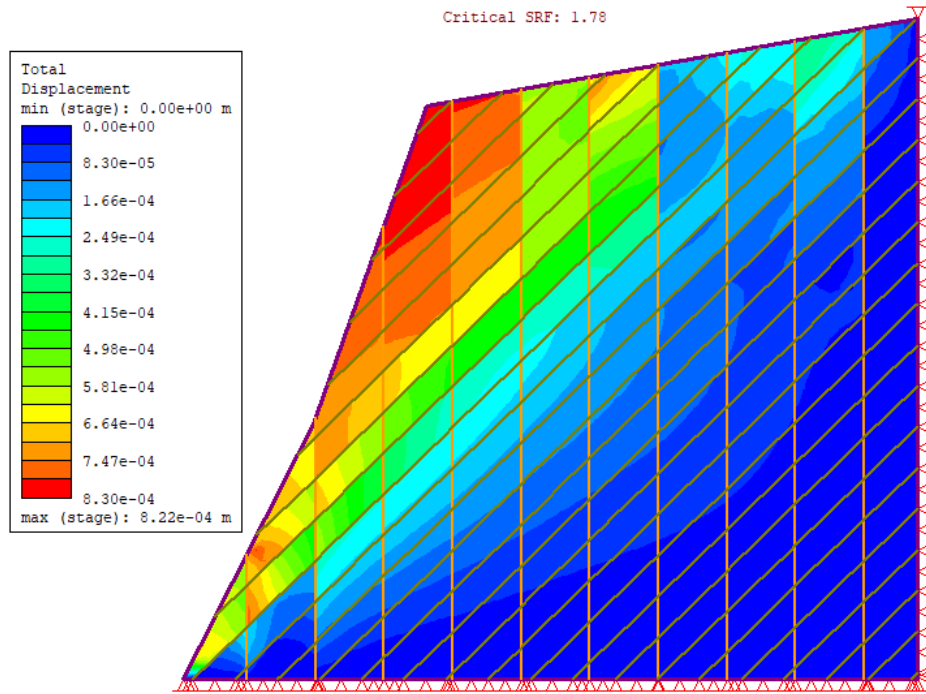


Figure 75: JS 9 and JS 4 (dry conditions)

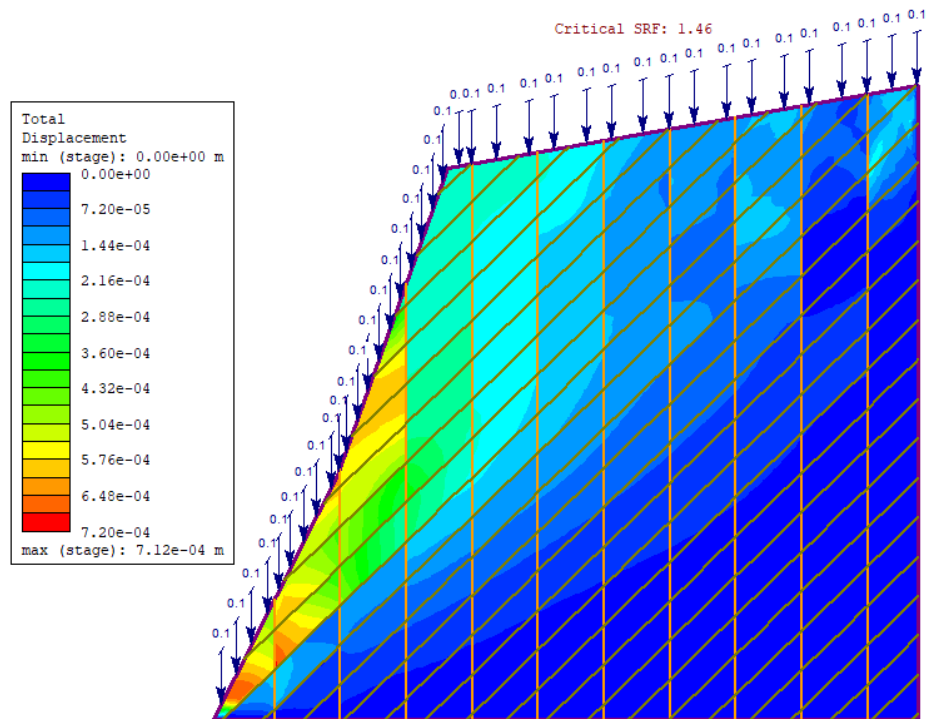


Figure 76: JS 9 and JS 4 (rainfall intensity 0.103 mm/day)

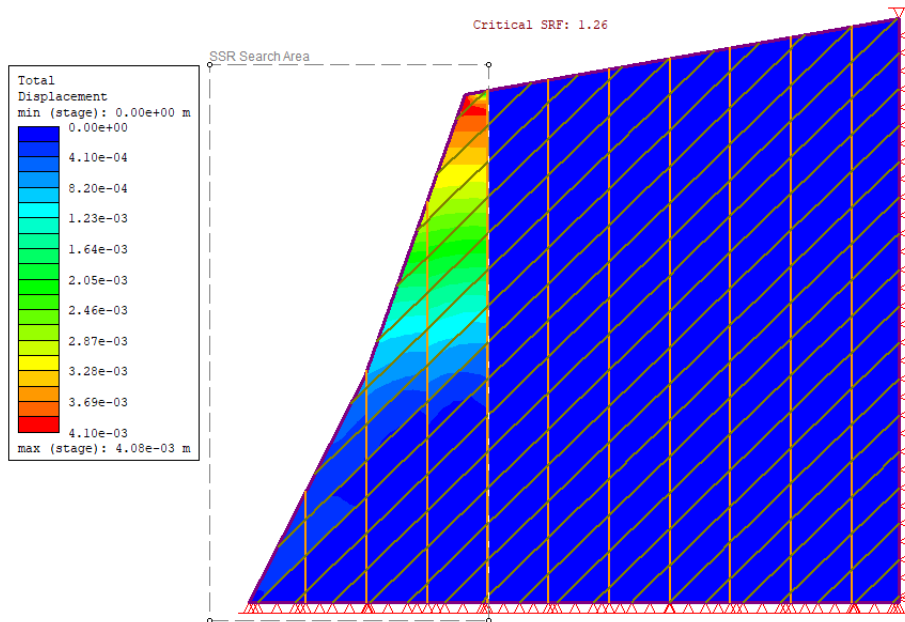


Figure 77: JS 9 and JS 4 (0.25g ground acceleration)

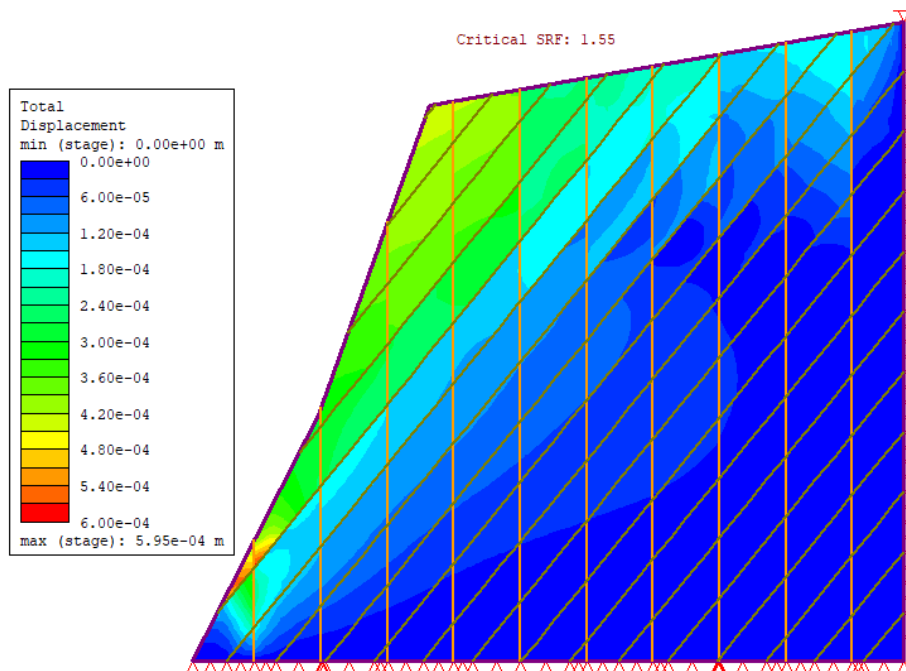


Figure 78: JS 9 and JS 3 (dry conditions)

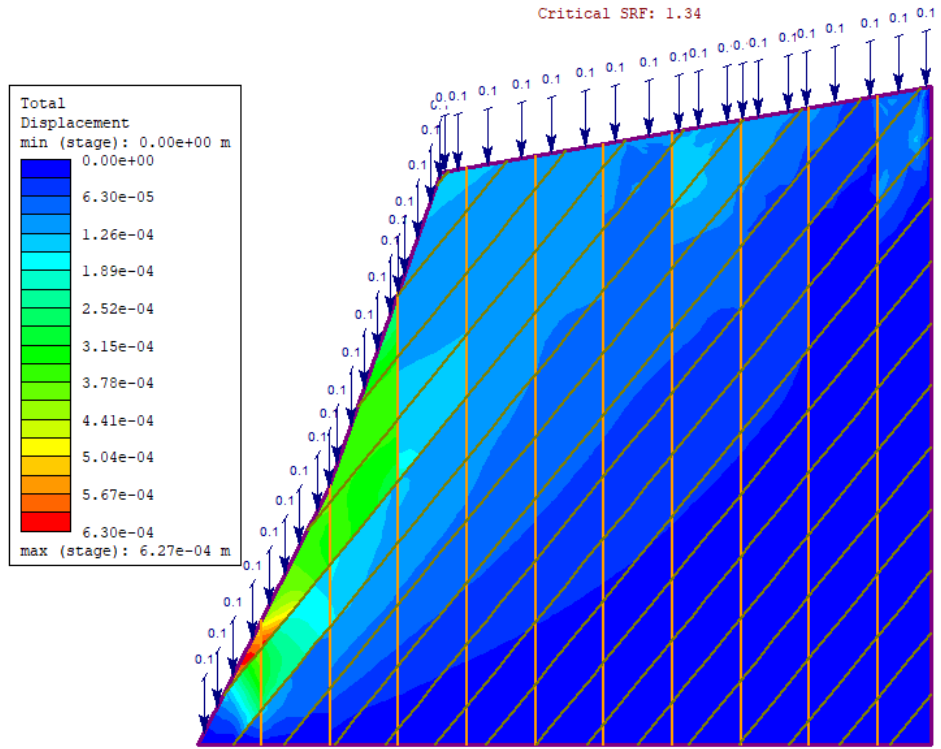


Figure 79: JS 9 and JS 3 (rainfall intensity 0.103 mm/day)

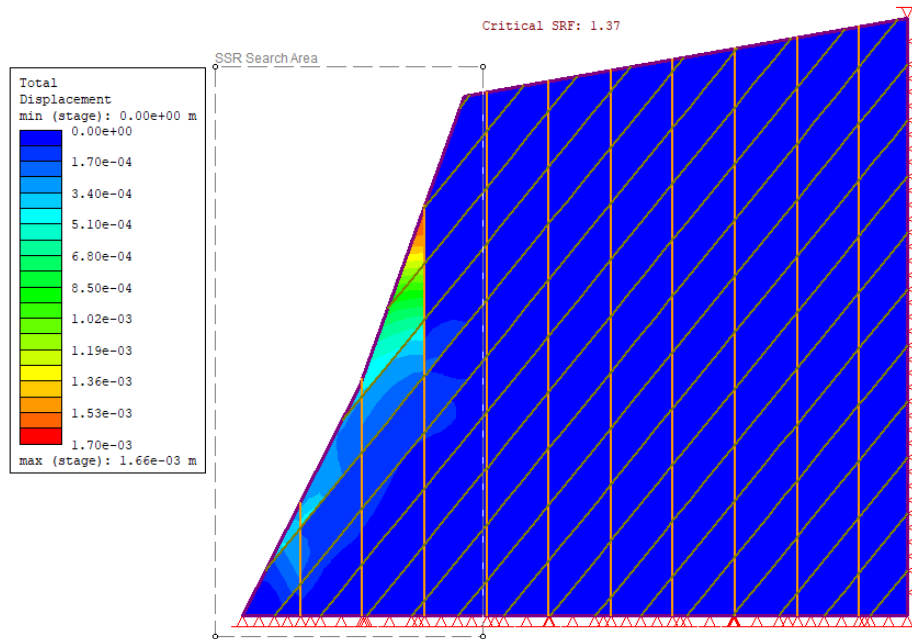


Figure 80: JS 9 and JS 3 (0.25g ground acceleration)

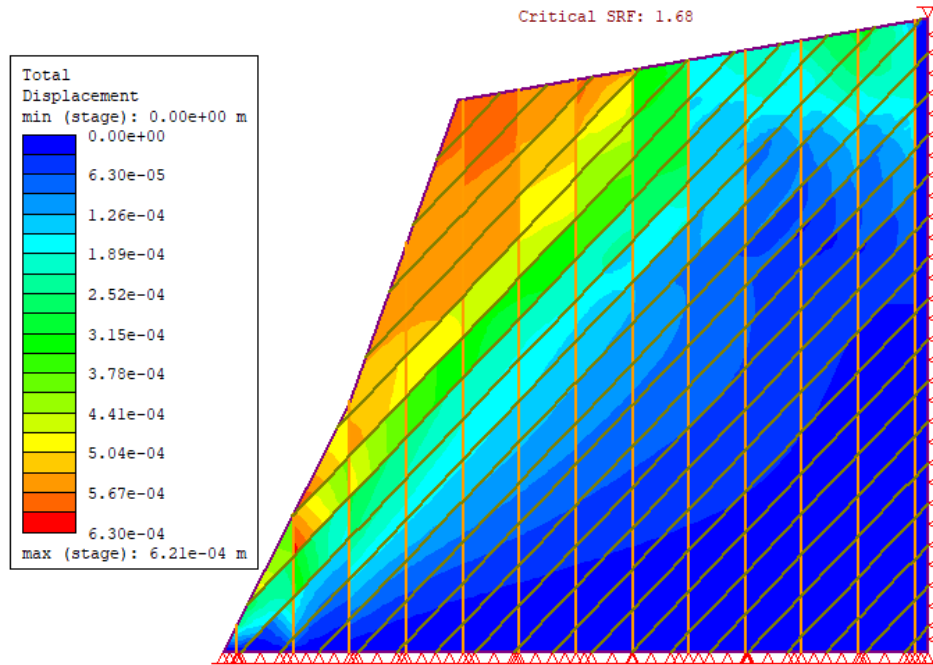


Figure 81: JS 2 and JS 8 (dry conditions)

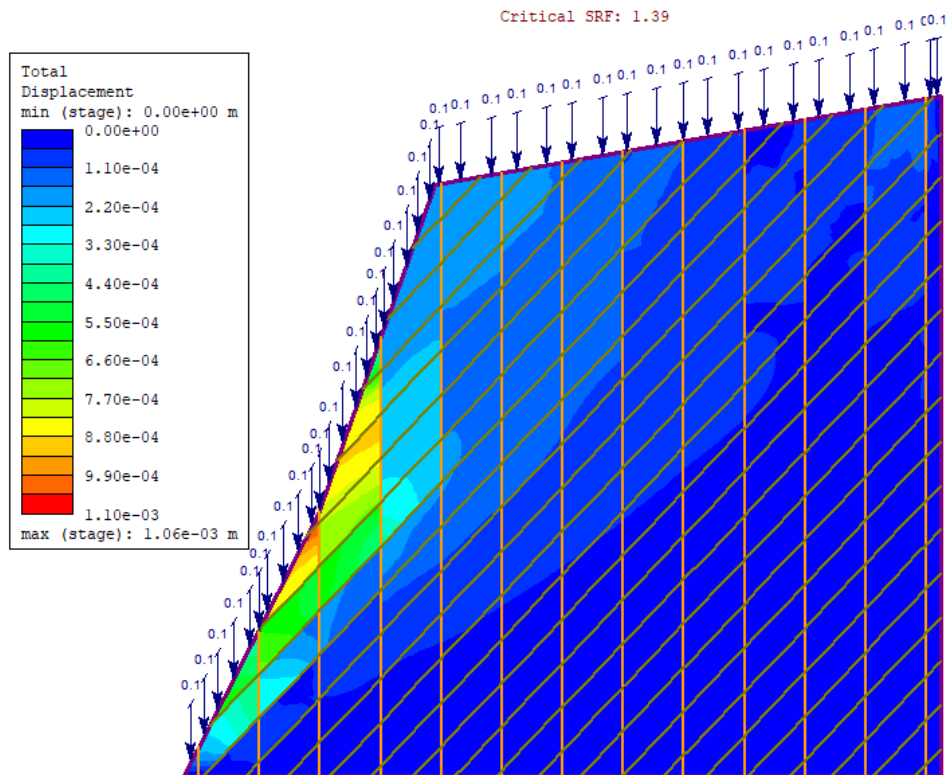


Figure 82: JS 2 and JS 8 (rainfall intensity 0.103 mm/day)



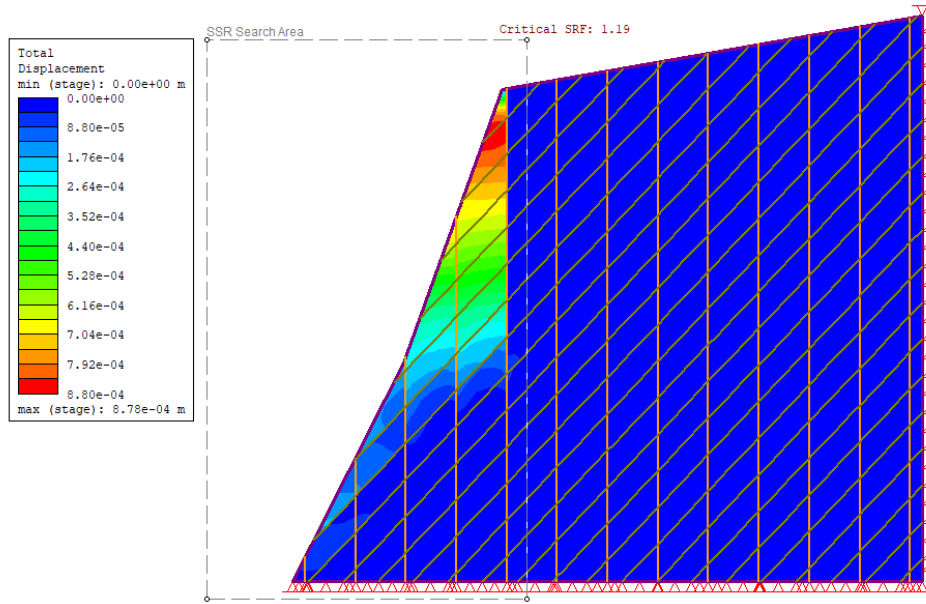


Figure 83: JS 2 and JS 8 (0.25g ground acceleration)

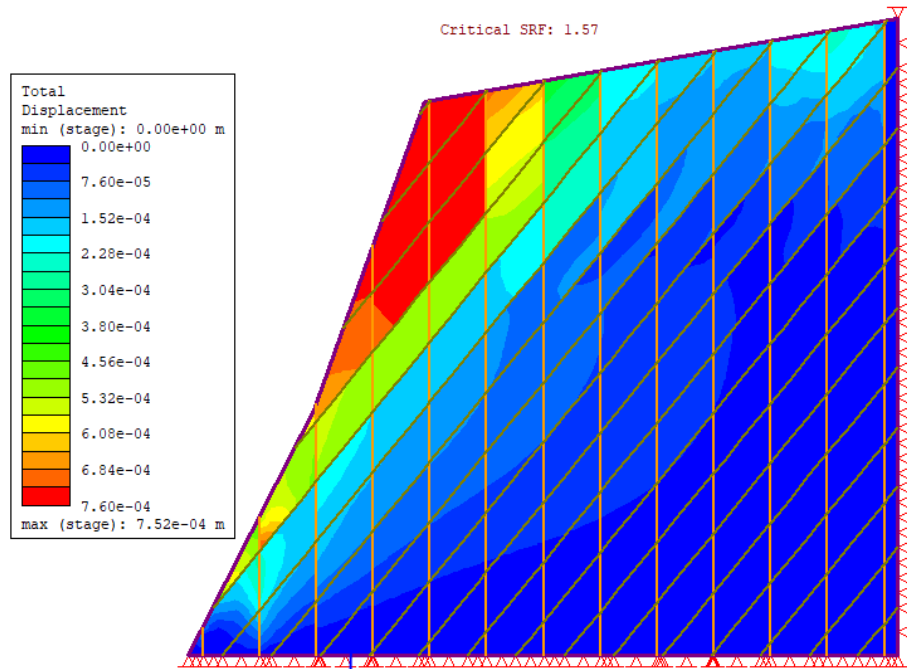


Figure 84: JS 3 and JS 8 (dry conditions)



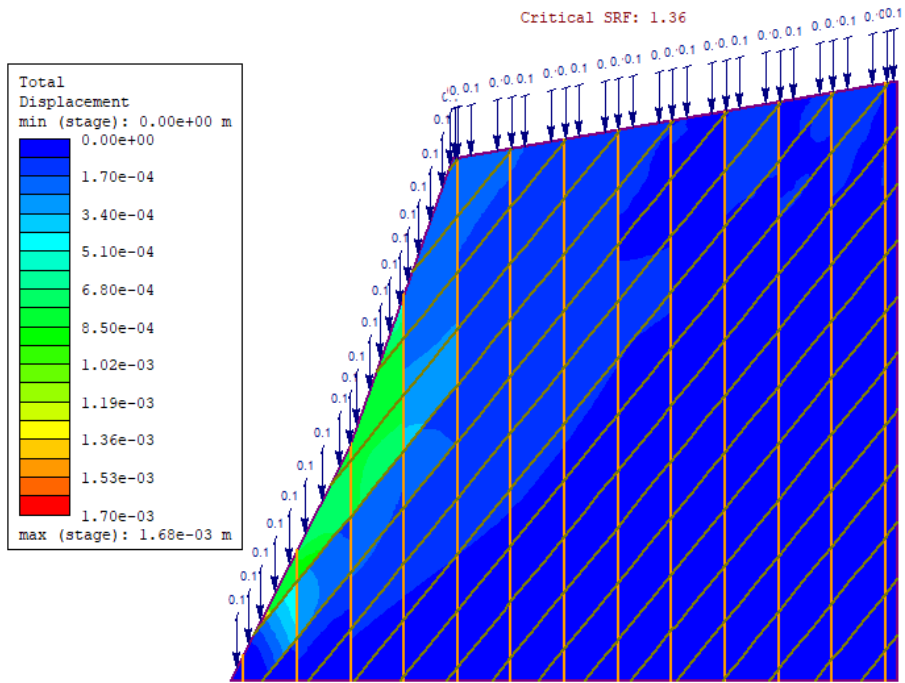


Figure 85: JS 3 and JS 8 (rainfall intensity 0.103 mm/day)

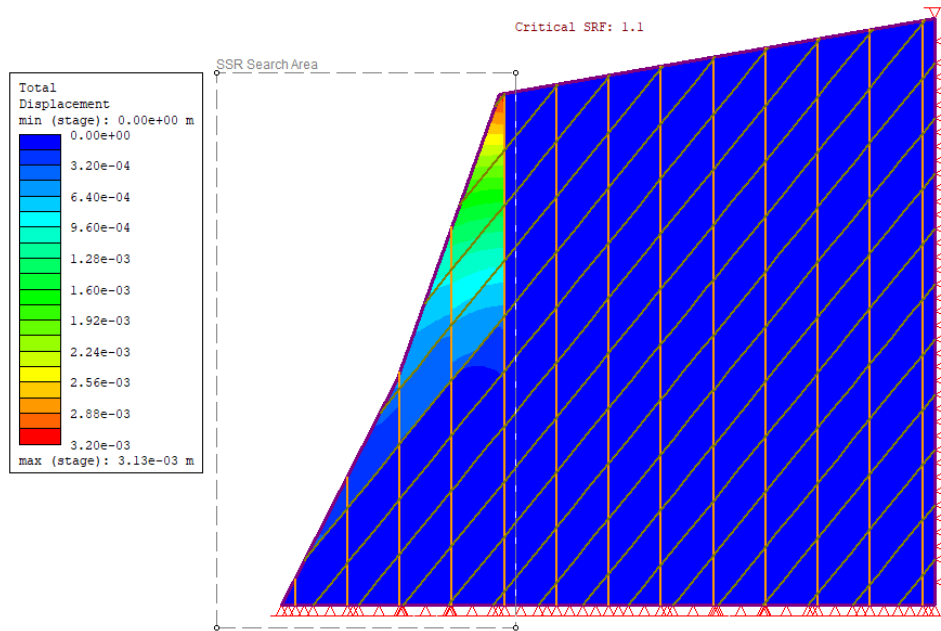


Figure 86: JS 3 and JS 8 (0.25g ground acceleration)

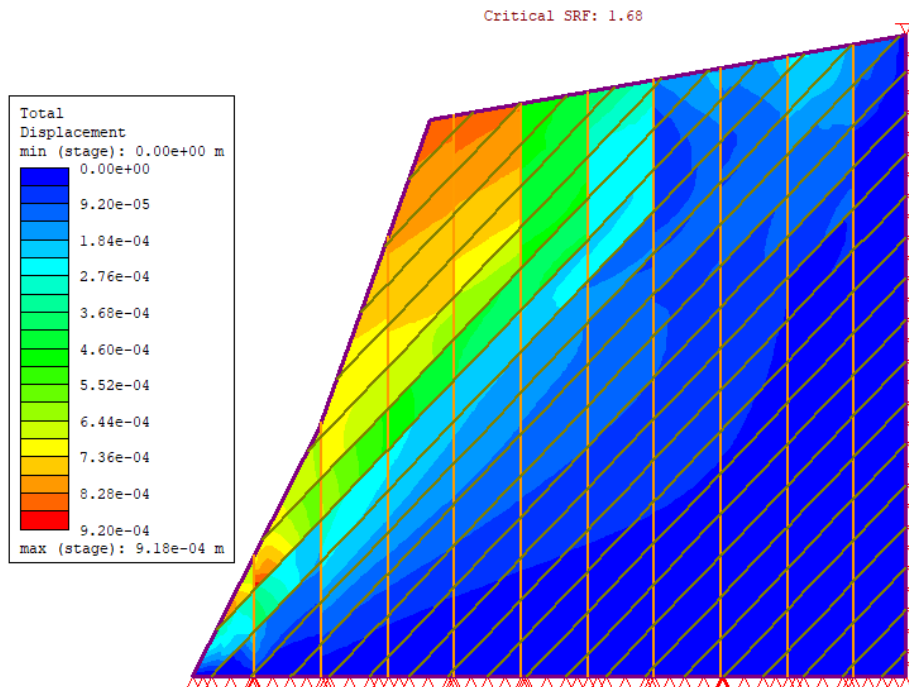


Figure 87: JS 2 and JS 9 (dry conditions)

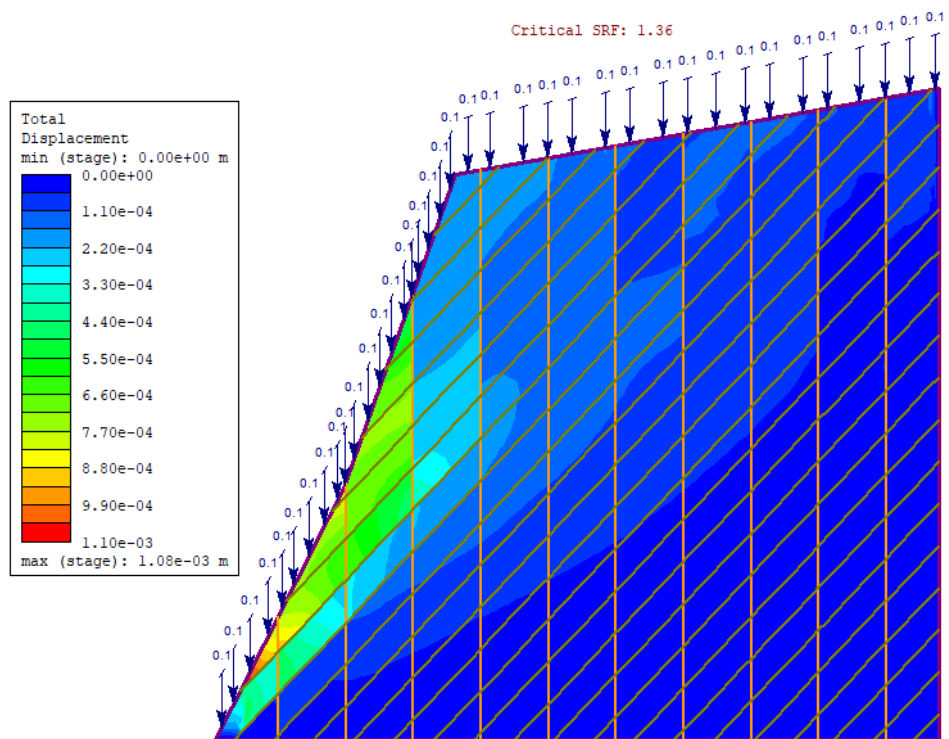


Figure 88: JS 2 and JS 9 (rainfall intensity 0.103 mm/day)

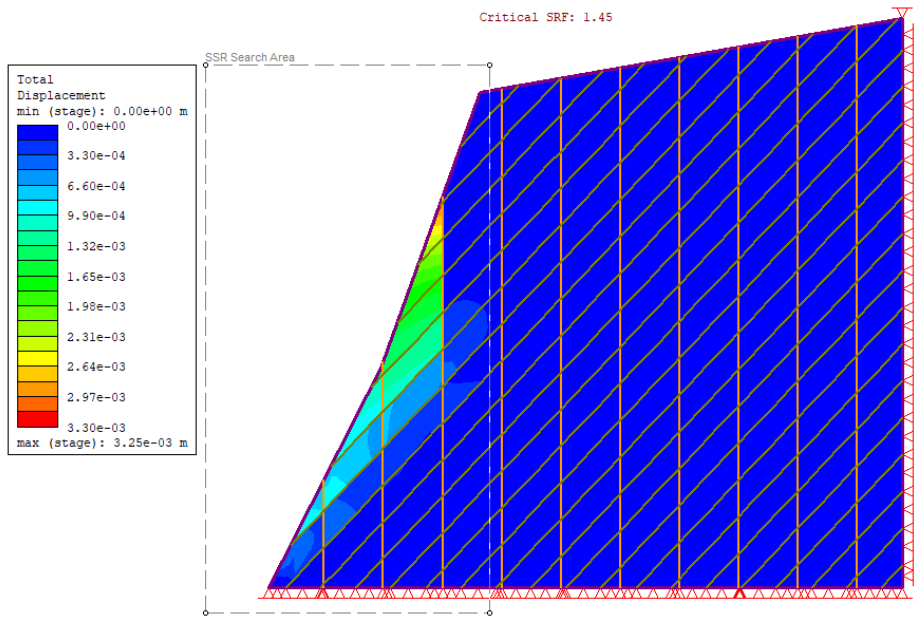


Figure 89: JS 2 and JS 9 (0.25g ground acceleration)

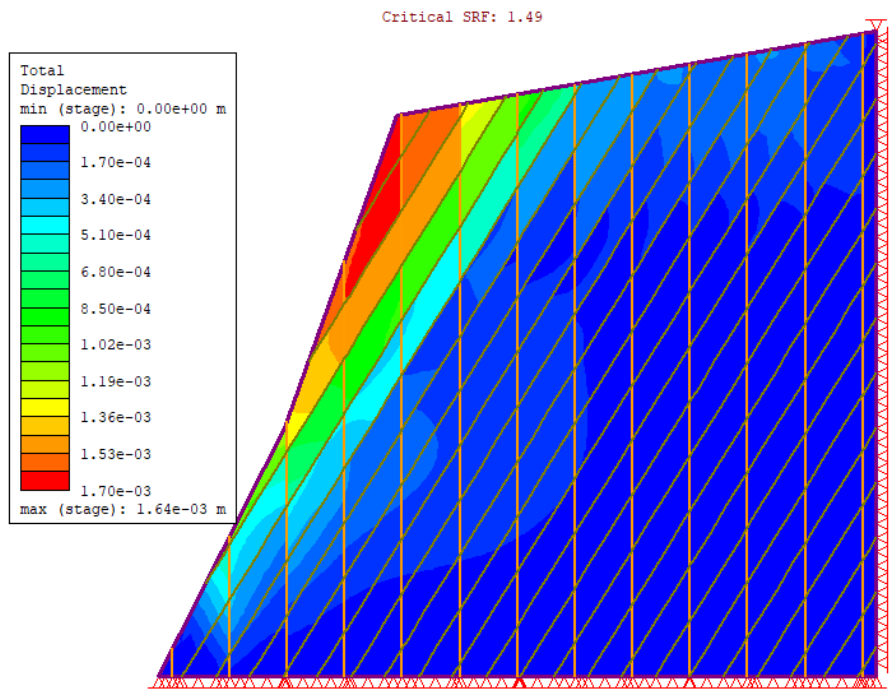


Figure 90: JS 8 and JS 5 (dry conditions)

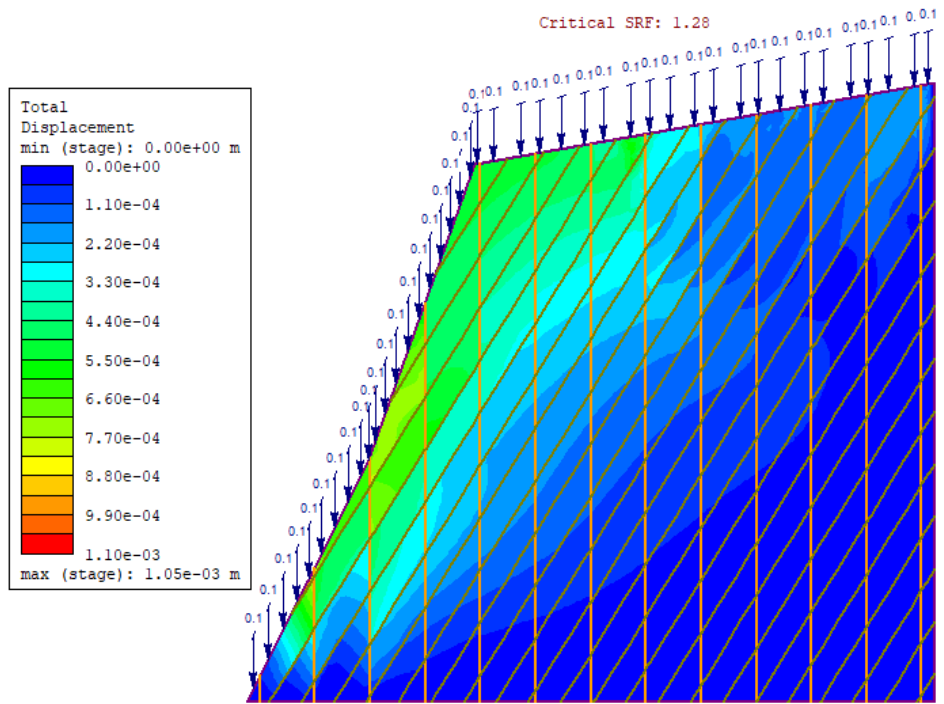


Figure 91: JS 8 and JS 5 (rainfall intensity 0.103 mm/day)

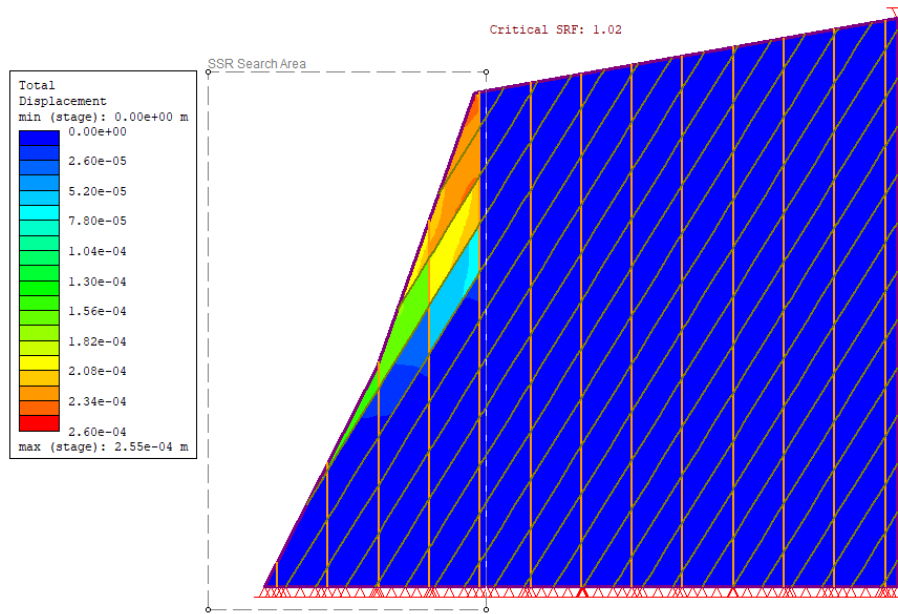


Figure 92: JS 8 and JS 5 (0.25g ground acceleration)

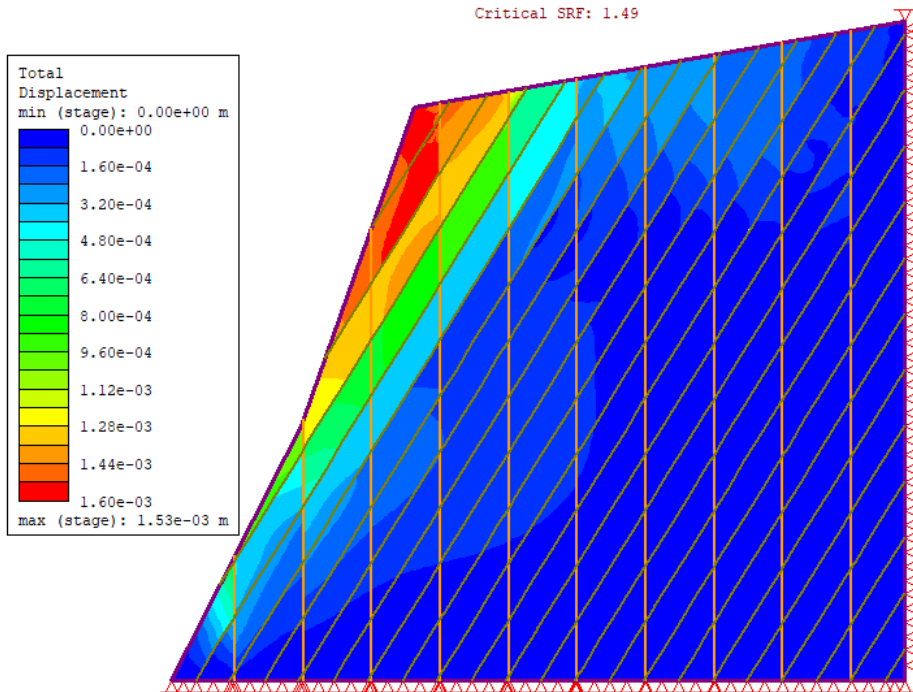


Figure 93: JS 9 and JS 5 (dry conditions)

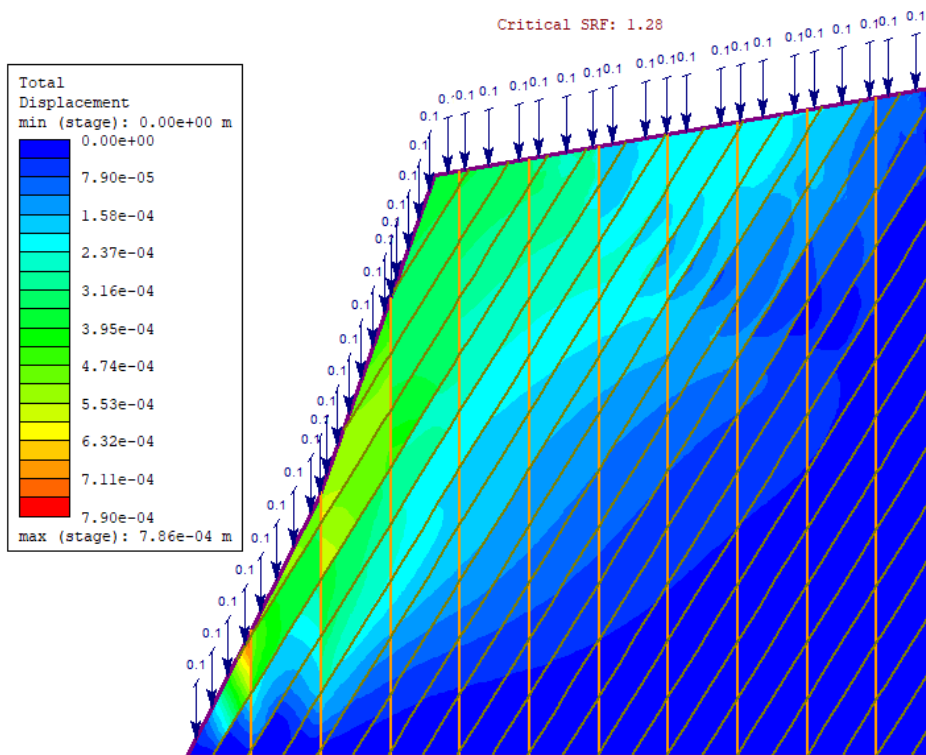


Figure 94: JS 9 and JS 5 (rainfall intensity 0.103 mm/day)

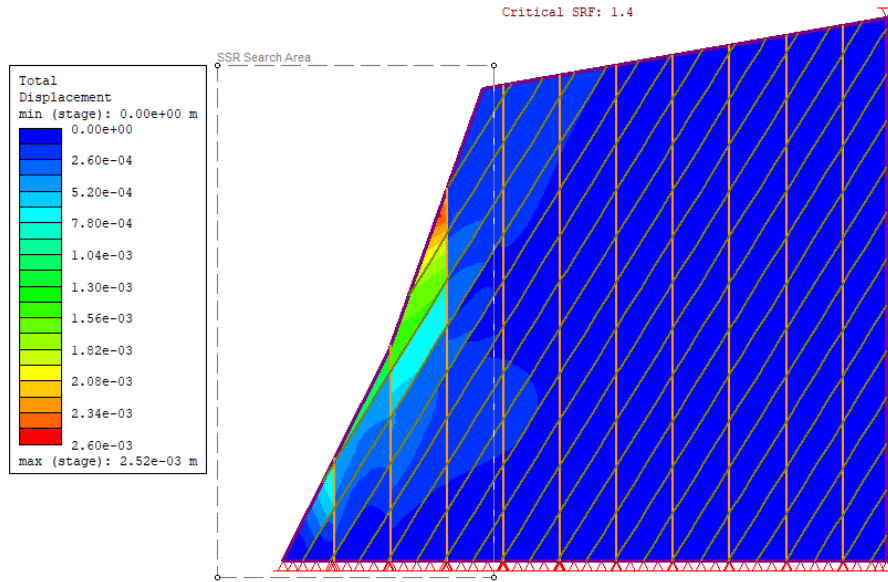


Figure 95: JS 9 and JS 5 (0.25g ground acceleration)

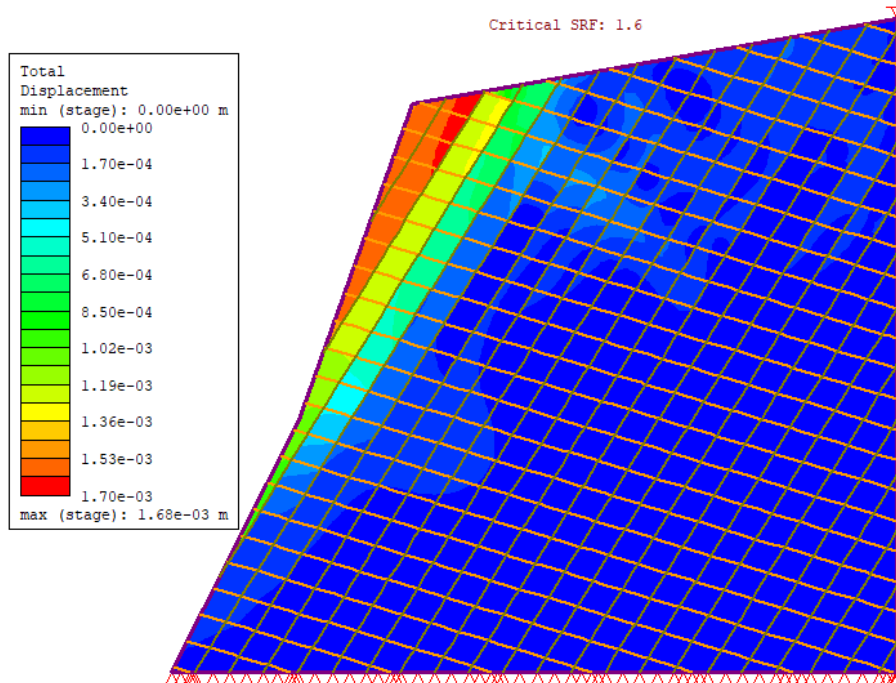


Figure 96: JS 2 and JS 5 (dry conditions)

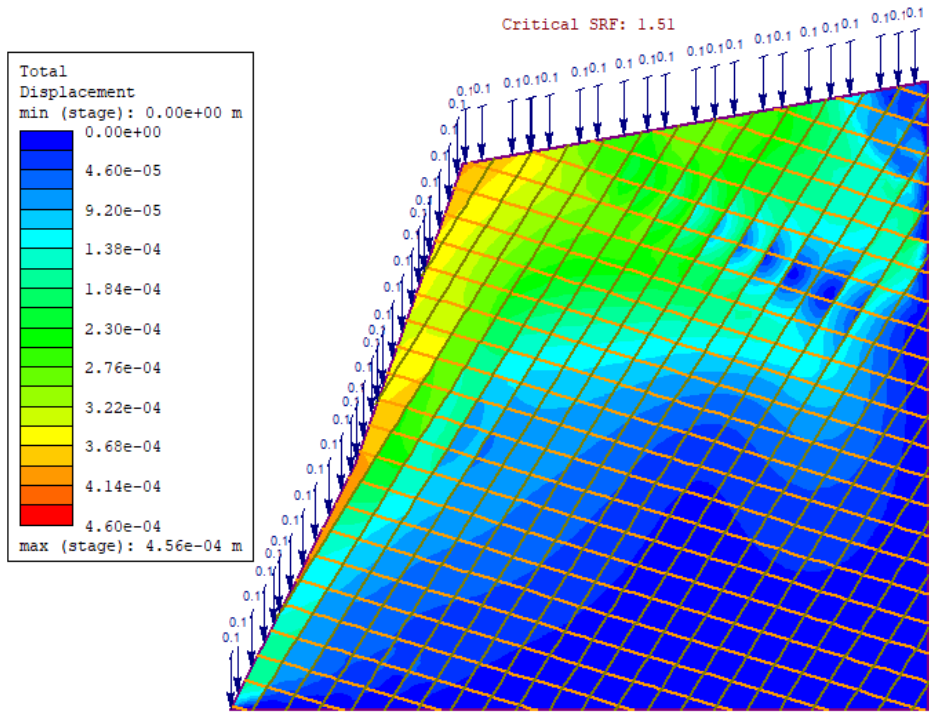


Figure 97: JS 2 and JS 5 (rainfall intensity 0.103 mm/day)

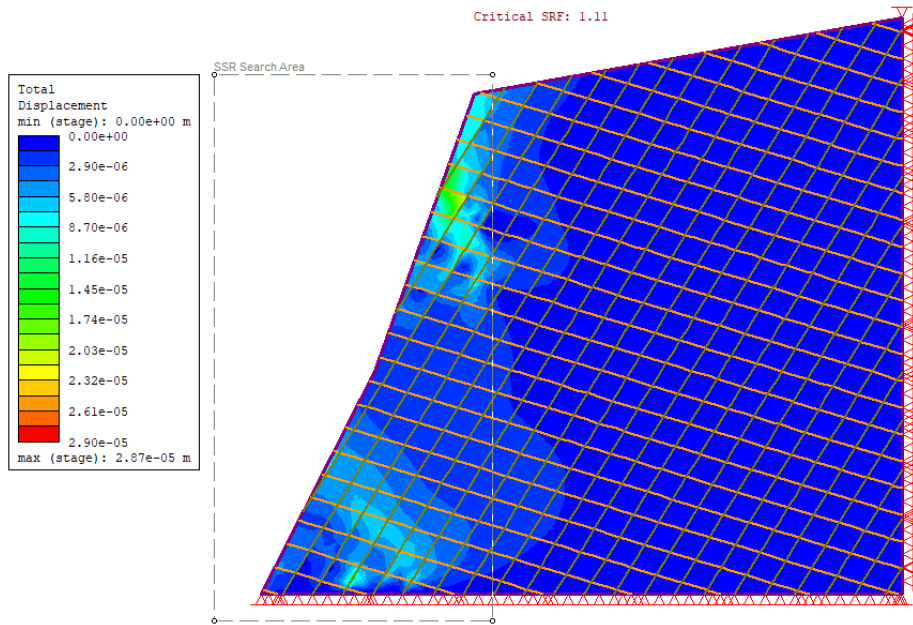


Figure 98: JS 2 and JS 5 (0.25g ground acceleration)



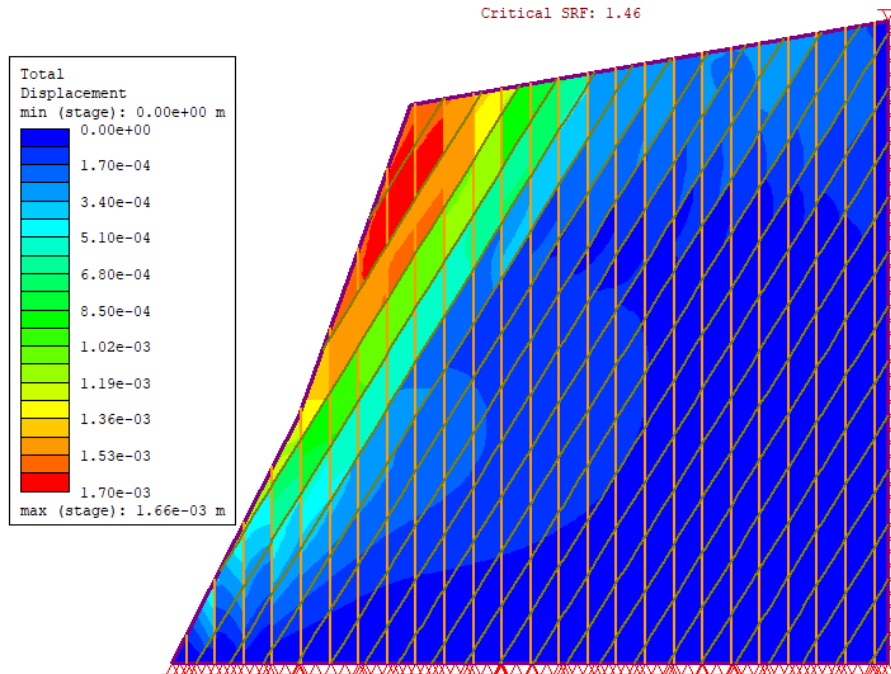


Figure 99: JS 7 and JS 5 (dry conditions)

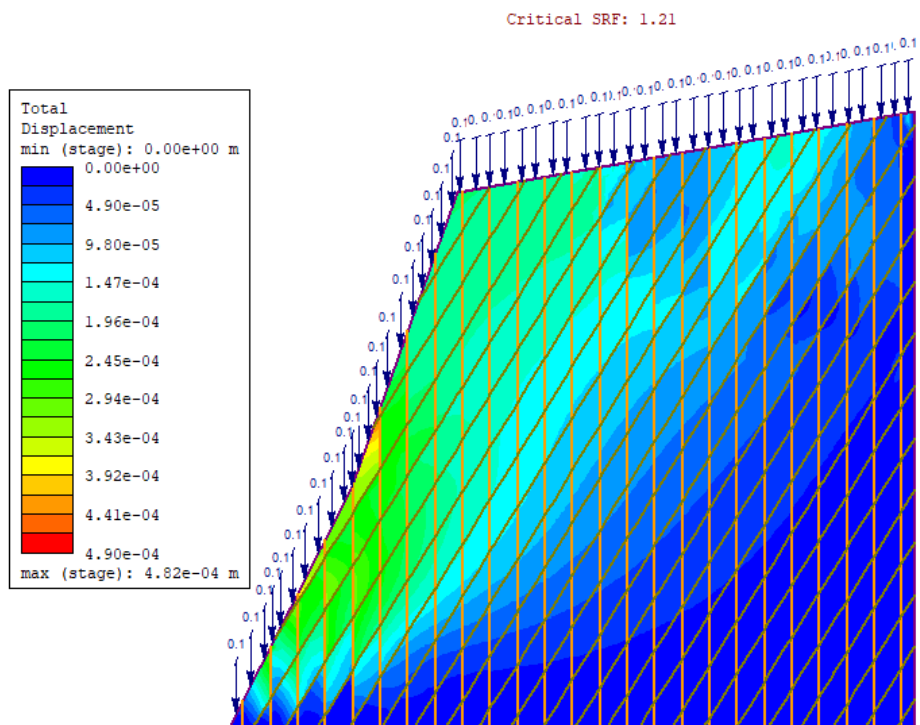


Figure 100: JS 7 and JS 5 (rainfall intensity 0.103 mm/day)



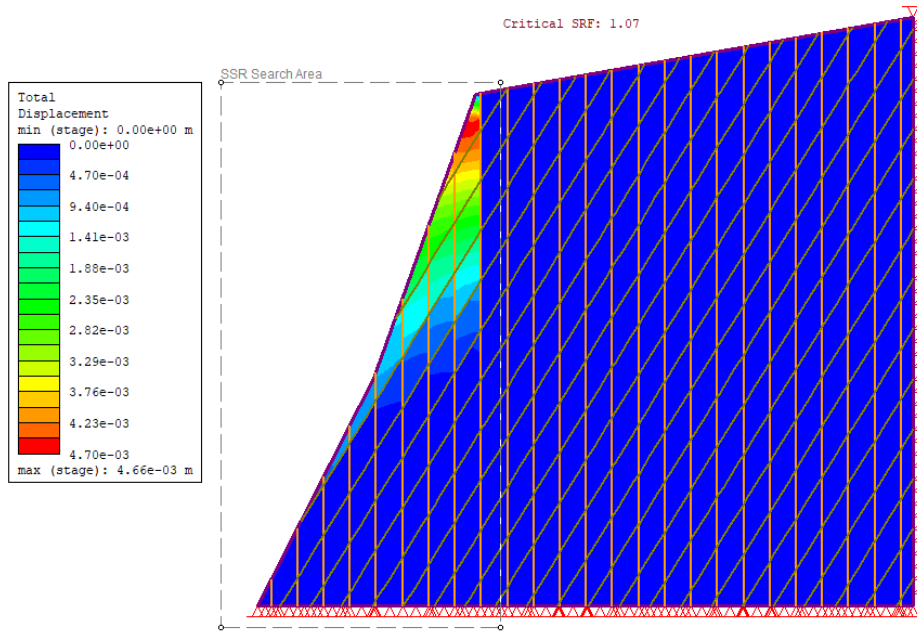


Figure 101: JS 7 and JS 5 (0.25g ground acceleration)

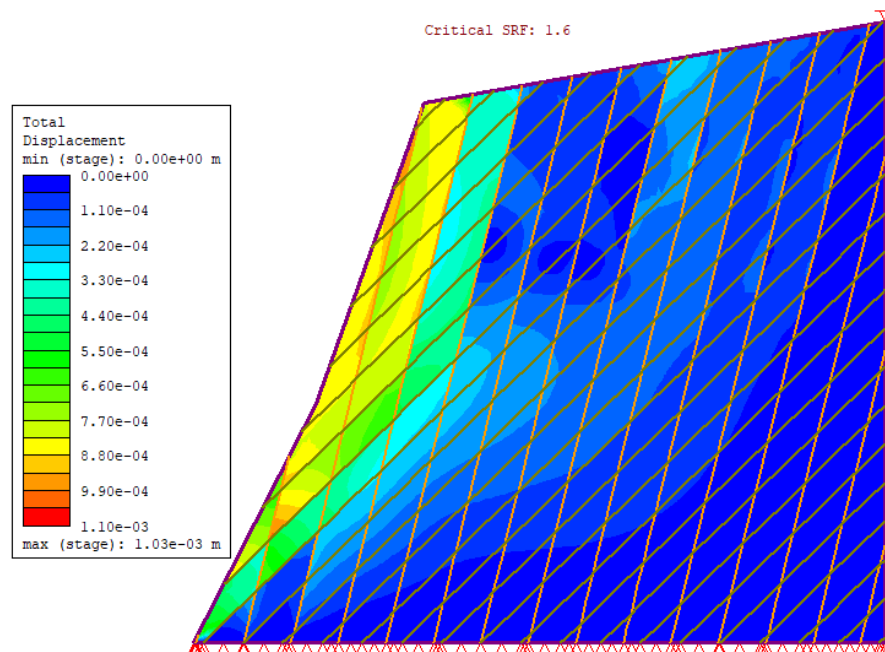


Figure 102: JS 6 and JS 4 (dry conditions)

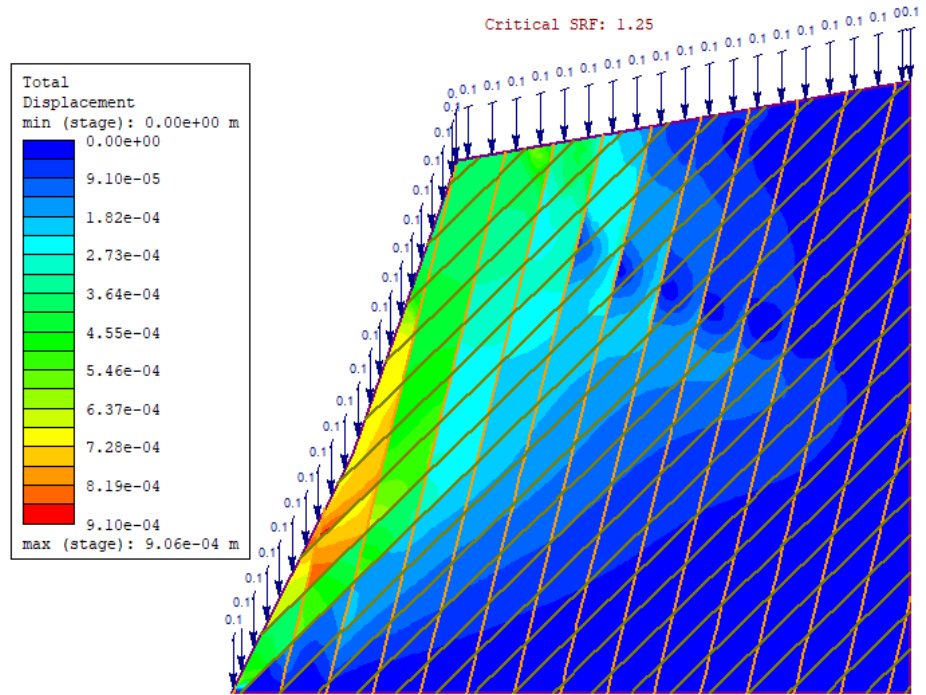


Figure 103: JS 6 and JS 4 (rainfall intensity 0.103 mm/day)

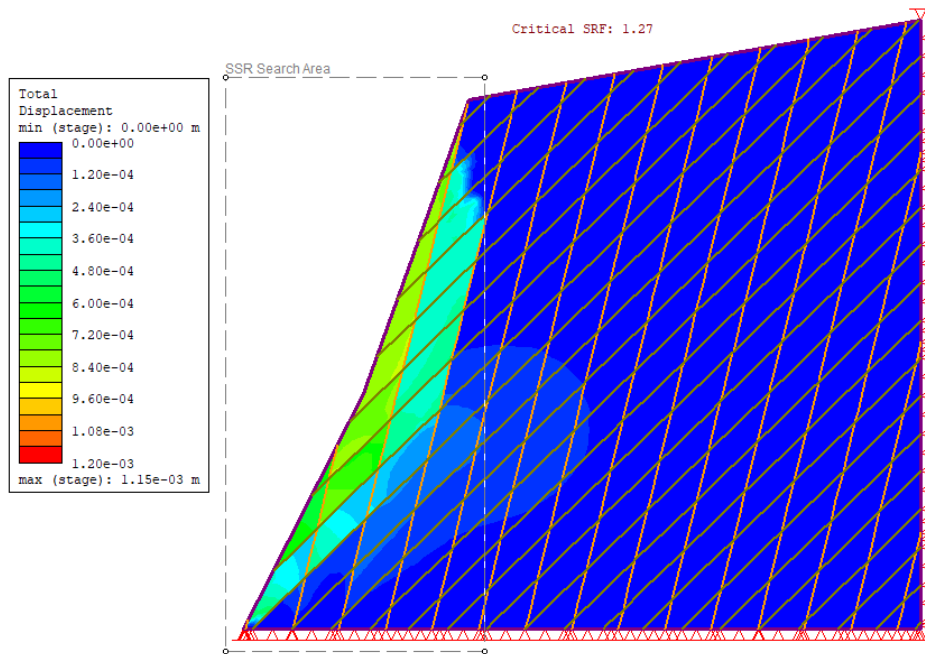


Figure 104: JS 6 and JS 4 (0.25g ground acceleration)

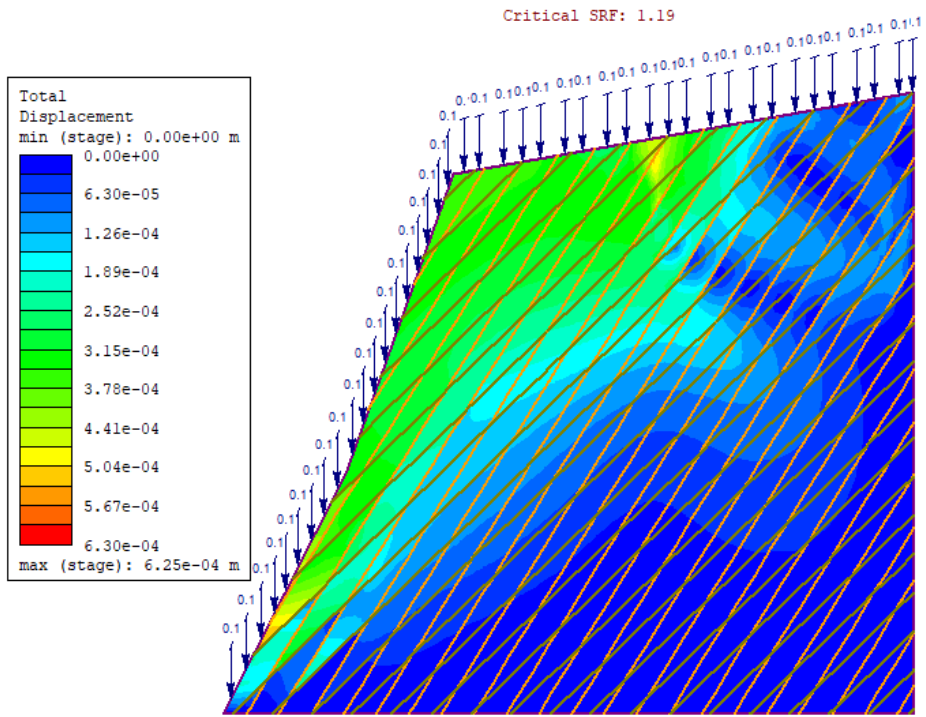


Figure 105: JS 5 and JS 4 (rainfall intensity 0.103 mm/day)

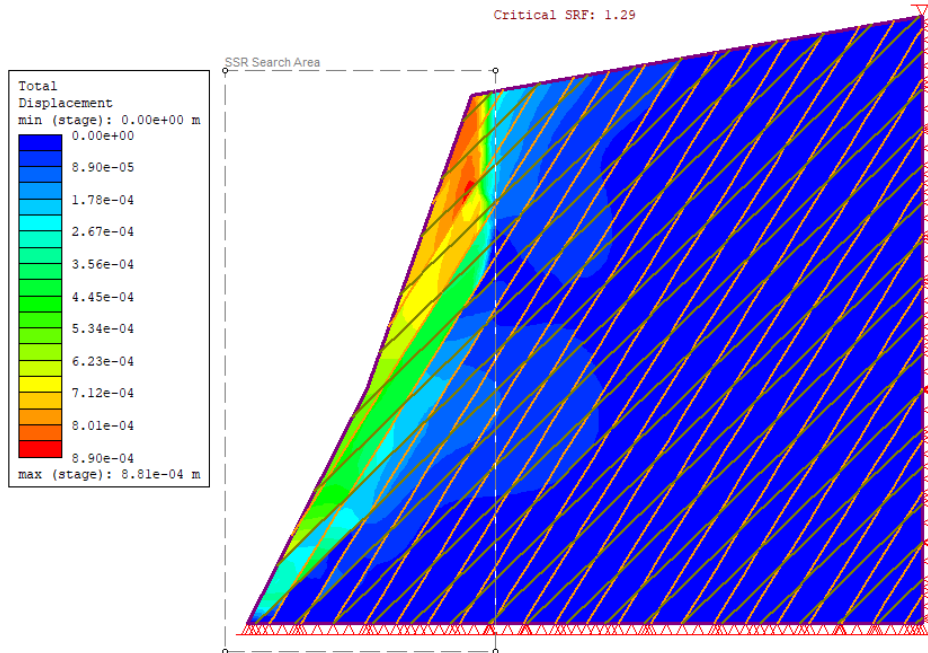


Figure 106: JS 5 and JS 4 (0.25g ground acceleration)

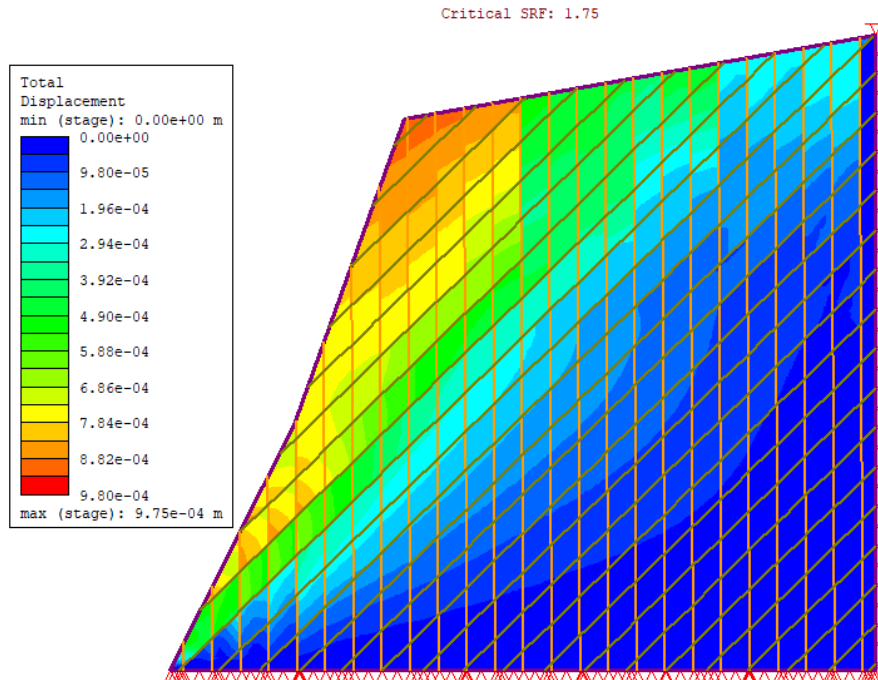


Figure 107: JS 10 and JS 4 (dry conditions)

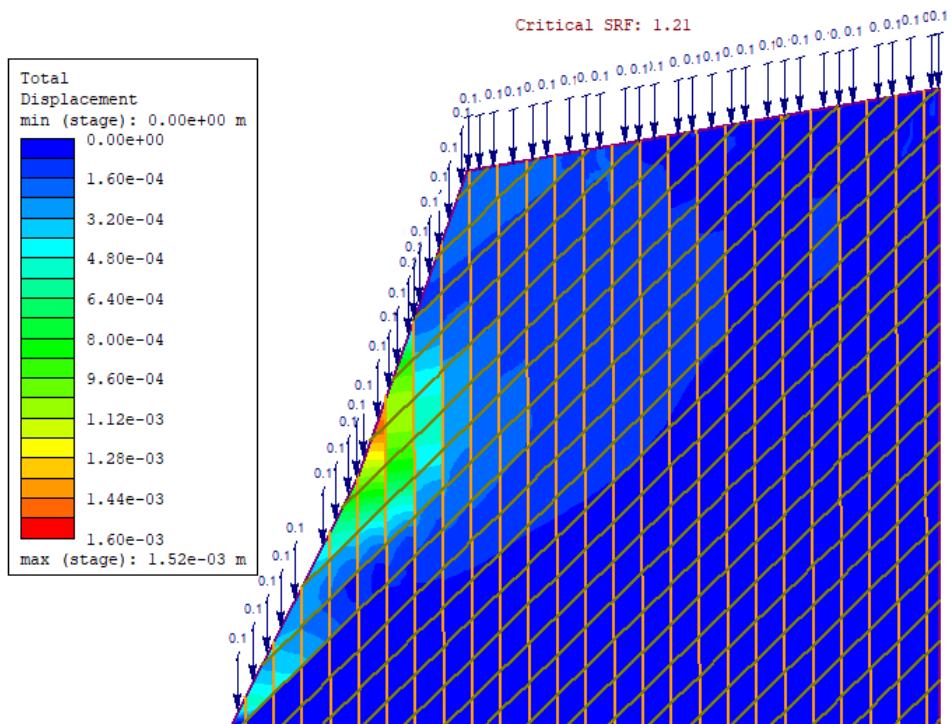


Figure 108: JS 10 and JS 4 (rainfall intensity 0.103 mm/day)

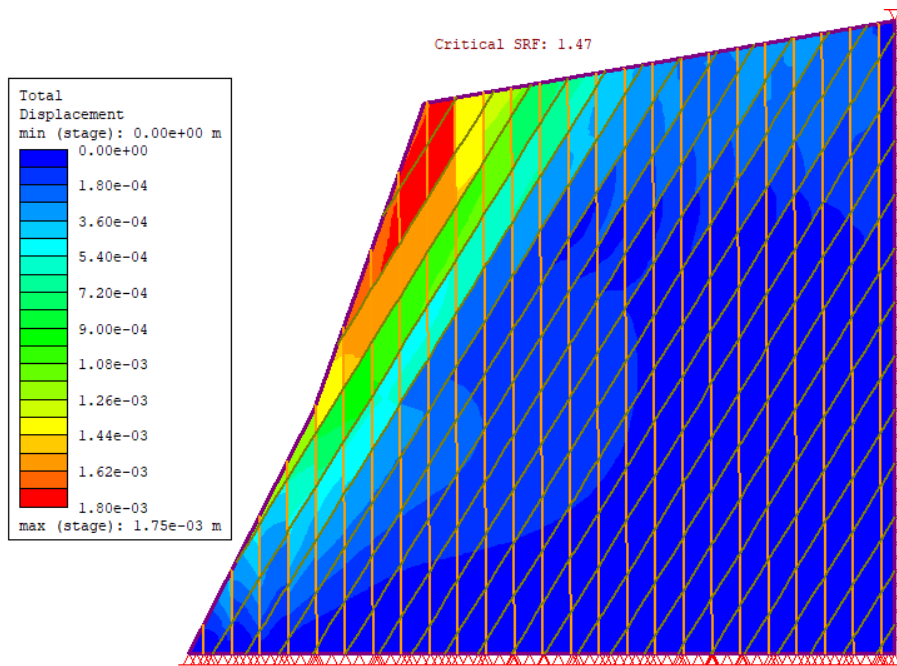


Figure 109: JS 10 and JS 5 (dry conditions)

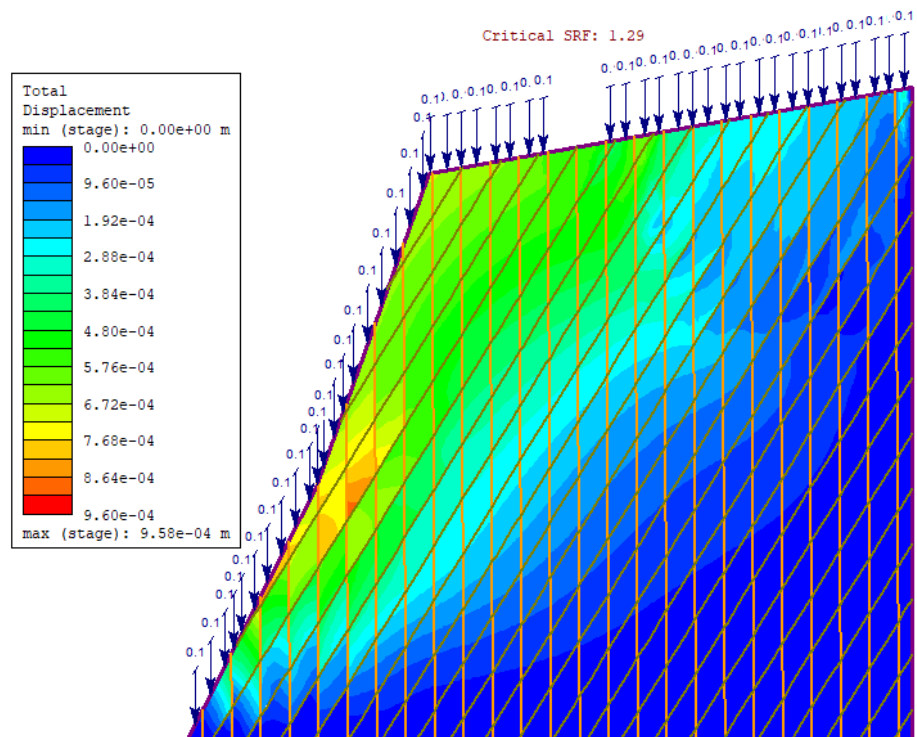


Figure 110: JS 10 and JS 5 (rainfall intensity 0.103 mm/day)

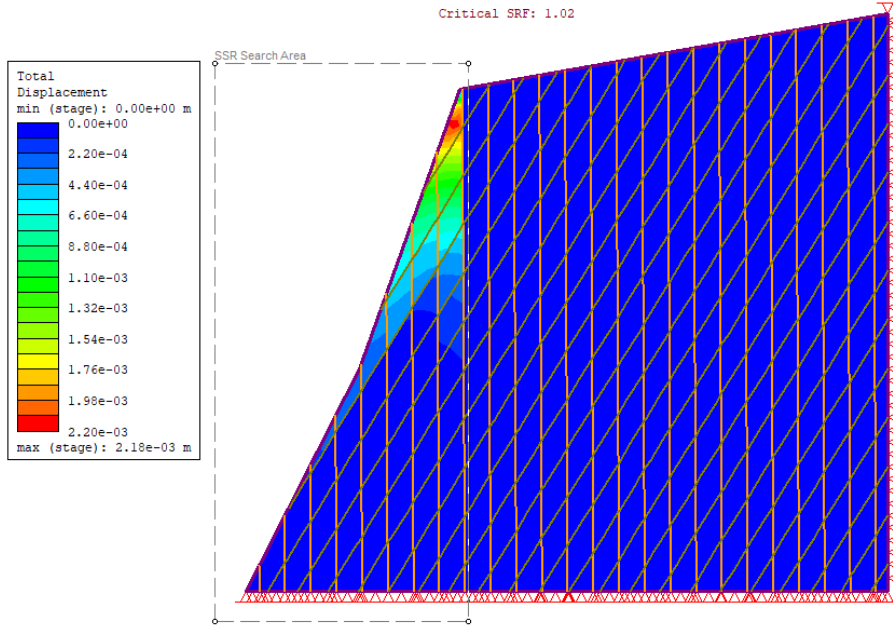


Figure 111: JS 10 and JS 5 (0.25g ground acceleration)